To the Graduate Council:

I am submitting herewith a dissertation written by Sayed Ahmad Ali Shohadaee entitled "Leak Detection Feasibility Investigation Using Radiation Transfer in Absorbing, Emitting, and Scattering Media". I have examined the final copy of this dissertation for form and content and recommend that it be accepted in partial fulfillment of the requirements for the degree of Doctor of Philosophy, with a major in Mechanical Engineering.

Roger A. Crawford, Major Professor

We have read this dissertation
and recommend its acceptance:

Accepted for the Council:

Vice Provost
and Dean of the Graduate School

LEAK DETECTION FEASIBILITY INVESTIGATION USING INFRARED RADIATION TRANSFER IN ABSORBING, EMITTING, AND SCATTERING MEDIA

A Dissertation

Presented for the

Doctor of Philosophy

Degree

The University of Tennessee, Knoxville

Sayed Ahmad Ali Shohadaee

December 1990



بسم الله الرحمن الرحيم

In the name of God, Most Gracious, Most Merciful

1. *Proclaim ! (or Read) in the name of thy Lord and Cherisher, Who created,-*
2. *Created man, out of a (mere) clot of congealed blood:*
3. *Proclaim ! And thy Lord is Most Bountiful,-*
4. *He Who taught (The use of) the Pen,-*
5. *Taught man that which he knew not.*
6. *Nay, but man doth transgress all bounds,*
7. *In that he looketh upon himself as self-sufficient.*
8. *Verily, to thy Lord is the return (of all).*

Holy Qur'an Sura XCVI.

تقدیم به پدر و مادر عزیزم

آقای سید علی اکبر و خانم سیده مولود شهدائی

To my Parents Mr. Sayed Ali Akbar Shohadaee

and Mrs. Moloud Shohadaee

ACKNOWLEDGMENT

I would like to express my sincere gratitude to my advisor, Dr. Roger A. Crawford, for his guidance, instruction and encouragement during the course of this work and for enthusiastic attitude towards learning which motivated me to continue my education. Without his patience, support, and fatherly guidance throughout my years at The University of Tennessee Space Institute, UTSI, would not have been able to finish this research. I would also like to express my deepest appreciation to Dr. Firouz Shahrokhi for spending countless extra hours advising and teaching me and for his instruction, encouragement and support. Special thanks to other members of the committee, Dr. Roy Schulz, and Dr. Kapuluru Reddy, for their wonderful lectures and for careful examination of this work and useful suggestions. Also, the most sincere appreciation to Dr. Ahad Sedghinasab for his continuous support and for many useful discussions relating to radiation heat transfer.

I extend the deepest gratitude to my father, mother and family members for the moral support which enabled me to complete my education. Special thanks is given to my sister Ashrat and her husband Mr. Mohammad Reza Nassirpour for their continual support and encouragement during my education in USA. I express my heartfelt thanks to my three daughters Maryam, Zahra, and Zaynab for their patience and understanding, and to all of my friends for their moral support during this study.

I am deeply indebted to Mrs. Charlene Hane for her wonderful help to prepare the publication for the last two years of my study. I am grateful to Dr. Monty Smith and Mrs. Joan Malone for their help in the Image Processing.

I would also like to acknowledge the faculty members of UTSI for their creative

influence on my academic career, and the graduate research assistantship from UTSI which provided me with financial support during my PhD program.

Finally, I would like to thank God for the health, patience, and determination needed to finish this research.

This study was sponsored by Center of Advance Space Propulsion (CASP), and was supported by NASA Grant NAGW-1195. The work was carried out at the Center for Laser Applications (CLA).

ABSTRACT

A radiation heat transfer model was developed to simulate the transfer of radiative energy in the infrared region $2 \leq \lambda \leq 5\mu m$ through an emitting, absorbing, and scattering plume of water vapor. The model makes use of the spectral features of the water vapor absorption coefficients to yield information on the spectral regions more sensitive to the absorption of a known background radiation source. Scattering was incorporated into the model by varying the albedo parameter from 0 to 0.9, representing all possible situations from no scattering to nearly full scattering. The radiation transport model was used to evaluate and estimate the wavelength sensitivity of infrared sensors for detection of hot and cold leak plumes. Experiments were carried out using an IR image recording and processing system to validate the results of the model. The conclusions of this investigation substantiate the use of IR thermal imaging systems to monitor cryogenic and hot gas leaks in systems such as the Space Shuttle Main Engine (SSME).

TABLE OF CONTENTS

CHAPTER PAGE

I. INTRODUCTION 1

II. LITERATURE REVIEW 5

III. FUNDAMENTALS OF RADIATION IN ABSORBING, EMITTING AND SCATTERING MEDIA 10

3.1 Physical Mechanisms of Absorption, Emission, and Scattering . . 10

3.1.1 Absorption and Emission 10

3.1.2 The Scattering of Energy 14

3.2 Definition of Radiation Intensity 15

3.3 The Attenuation of Energy by Absorption and Scattering 17

3.3.1 Optical Thickness 19

3.3.2 The Absorption Coefficient 19

3.3.3 True Absorption Coefficient 20

3.3.4 The Scattering Coefficient 21

3.4 The Emission of Energy 24

3.5 Incoming Scattering 27

3.5.1 The Phase Function 27

3.5.2 Augmentation of Intensity by Incoming Scattering 29

3.6 The Equation of Transfer 31

3.6.1 Derivation 31

3.7 Integration by Use of Integrating Factor 34

IV. ANALYSIS 37

4.1 Statement of Problem 37

4.2 Basic Assumptions 39

4.3 Equation of Transfer in x-Direction 40
4.4 Equation of Source Function 41
4.5 Boundary Conditions 44
4.6 Blackbody Radiation Source with Absorbing and Emitting Media 44
4.7 Blackbody Radiation Source with Absorbing, Emitting, and Scattering Media 45
V. NUMERICAL MODELING 46
5.1 Numerical Form of The Equation of Transfer 46
5.2 Absorption Coefficient Data to be used 50
5.3 Temperature Distribution 59
5.4 Numerical Procedure 61
5.4.1 Subroutine ABSCOF 61
5.4.2 Subroutine TEMP 63
5.4.3 Subroutine INTPOL 63
5.4.4 Subroutine OPTHIC 65
5.4.5 Subroutine BBINT 65
5.4.6 Subroutine SIMPCOF 65
5.4.7 Subroutine PLATINT 65
5.4.8 Subroutine SIMPSON 66
5.4.9 Subroutine BIGINT 66
5.4.10 Subroutine SOURCE 66
VI. DISCUSSION OF NUMERICAL RESULTS 67
6.1 Blackbody Radiation Source with Absorbing and Emitting Media 67
6.2 Blackbody Radiation Source with Absorbing, Emitting, and Scattering Media 89
VII. EXPERIMENTAL SYSTEM 116

7.1 Thermovision System 116
7.1.1 The Scanner Unit 118
7.1.2 Detector 120
7.1.3 The Interchaneable Lenses 120
7.1.4 Object Field Data 122
7.1.5 Aperture Selection 122
7.1.6 The Display Unit 122
7.1.7 Video Cassette Recording (VCR) 126
7.1.8 Computer Systems 127
7.1.8.1 Thermal Image Computer TIC 127
7.1.8.2 Temperature Readout Computer TRC 127
7.1.9 Atomizer 128
7.2 Experimental Resultes 128
7.2.1 Cold Plume in Front of Warm Background Plate 128
7.2.2 Hot Plume in Front of Warm Background Plate 133
7.3 Comparison of Numerical and Experimental Results 133
7.4 Impingement Cooling 141
VIII. CONCLUSIONS AND RECOMMENDATIONS 145
BIBLIOGRAPHY 147
VITA 152

LIST OF TABLES

TABLE PAGE

7.1 Scanned field (W) and depth of focus (+) set at various distances (d) 123

LIST OF FIGURES

FIGURE PAGE

3.1 Schematic diagram of energy states and transition for atom, ion, or electron. 12

3.2 Spectral emission intensity from black surface. 16

3.3 Intensity incident normally on absorbing layer of thickness dS. . . . 18

3.4 Scattering of intensity into direction (θ, ϕ) from incident radiation within solid angle $d\omega_i$. 23

3.5 Geometry for derivation of emission from volume of gas. 25

3.6 Scattering of energy into S direction. 30

3.7 Geometry for direction of equation of transfer. 32

4.1 Schematic illustration of the problem. 38

4.2 Directional intensity through the plume. 43

5.1 Equally spaced abscissas for numerical computation. 47

5.2 Mean absorption coefficient for water vapor at various temperatures. 51

5.3 Straight line technique for numerical calculation of absorption coefficient. 58

5.4 The Gaussian temperature distribution across the plume. 60

5.5 Flowchart of the Main program. 62

5.6 Temperature distribution across the hot plume at different radii ($T_1 = T_{max}$ *and* $T_{JL} = T_{min}$) 64

6.1 Geometrical arrangement. 68

6.2 Plume cross section for numerical calculation. 69

6.3 Spectral intensity vs. Y for cold background plate with hot gas plume. ($T_p = 300^oK$, $T_{max} = 1000^oK$, $T_{min} = 300^oK$) 70

6.4 Spectral intensity vs. Y for hot background plate with cold gas plume. ($T_p = 800^oK$, $T_{max} = 400^oK$, $T_{min} = 300^oK$) 71

6.5 Spectral intensity vs. wavelength for hot background plate with cold gas plume at different Y locations. ($T_p = 1000^oK$, $T_{max} = 600^oK$, $T_{min} = 300^oK$) 73

6.6 Spectral intensity vs. wavelength for cold background plate with hot gas plume at different Y locations. ($T_p = 300^oK$, $T_{max} = 1000^oK$, $T_{min} = 300^oK$) 74

6.7 Spectral intensity vs. wavelength at different plume diameters. ($T_p = 755^oK$, $T_{max} = 373^oK$, $T_{min} = 300^oK$) 75

6.8 Spectral intensity vs. wavelength at different plume diameters. ($T_p = 755^oK$, $T_{max} = 373^oK$, $T_{min} = 300^oK$) 76

6.9 Integrated intensity vs. Y at different plume diameters. ($T_p = 755^oK$, $T_{max} = 373^oK$, $T_{min} = 300^oK$ and $2.0 \leq \lambda \leq 5.0\mu m$) 77

6.10 Integrated intensity vs. Y at different plume diameters. ($T_p = 755^oK$, $T_{max} = 373^oK$, $T_{min} = 300^oK$ and $2.0 \leq \lambda \leq 5.0\mu m$) 78

6.11 Integrated intensity vs. Y at different plume diameters. ($T_p = 755^oK$, $T_{max} = 373^oK$, $T_{min} = 300^oK$ and $2.5 \leq \lambda \leq 2.86\mu m$) 80

6.12 Integrated intensity vs. Y at different plume diameters. ($T_p = 755^oK$, $T_{max} = 373^oK$, $T_{min} = 300^oK$ and $2.5 \leq \lambda \leq 2.86\mu m$) 81

6.13 Percentage of Integrated intensity reduced vs. R ($T_p = 755^oK$, $T_{max} = 373^oK$, $T_{min} = 300^oK$) 82

6.14 Integrated intensity vs. Y at different plate temperatures. ($T_{max} = 1200^oK$, $T_{min} = 300^oK$ *and* $DP = 5.0$ *cm*) 84

6.15 Scattering coefficient vs. wavelengthat a fixed temperature of 300^oK. 90

6.16 Source function vs. wavelength at different albedos ($T_p = 755^oK$, $T_{max} = 373^oK$, $T_{min} = 300^oK$, $DP = 10cm$, and Y=0.0) 92

6.17 Source function vs. position across the plume for different albedos. ($T_p = 755^oK$, $T_{max} = 373^oK$, $T_{min} = 300^oK$, $DP = 10$ *cm*, *and* $\lambda = 2.86\mu m$) 94

6.18 Source function vs. position across the plume. ($T_p = 755^oK$, $T_{max} = 373^oK$, $T_{min} = 300^oK$, $DP = 10$ *cm*) 95

6.19 Spectral intensity vs. wavelength for hot background plate with cold gas plume. ($T_p = 755°K$, $T_{max} = 373°K$, $T_{min} = 300°K$, *and* $DP = 10cm$) . . 97

6.20 Spectral intensity vs. wavelength for hot background plate with cold gas plume. ($T_p = 1755°K$, $T_{max} = 373°K$, $T_{min} = 300°K$, *and* $DP = 10cm$) . . 98

6.21 Spectral intensity vs. wavelength at different plate temperatures with hot gas plume. ($T_{max} = 1200°K$, $T_{min} = 300°K$, *and* $DP = 5cm$) 100

6.22 Integrated intensity vs. Y at different albedos. ($T_p = 700°K$, $T_{max} = 1200°K$, $T_{min} = 300°K$, *and* $DP = 5\ cm$) . . 106

6.23 Integrated intensity vs. Y at different albedos. ($T_p = 900°K$, $T_{max} = 1200°K$, $T_{min} = 300°K$, *and* $DP = 5\ cm$) . . 111

7.1 Experimental Arrangement 117

7.2 Connection of the Thermovision 870 system 119

7.3 Cutaway view of Thermovision scanner 121

7.4 Dimension of scanned surfaces with various lenses 124

7.5 Display unit. 125

7.6 Thermal image of the cold plume in front of warm background radiation source. 130

7.7 Thermal image of the warm background radiation source without the plume at $T_p = 460°K$. 131

7.8 Thermal image of the warm background radiation source with the plume. 132

7.9 Thermal image of the warm background radiation source without the plume at $T_p = 485°K$. 134

7.10 Thermal image of the warm background radiation source with the plume. 135

7.11 Thermal image of the hot plume in front of the warm background radiation source. 136

7.12 Sketch of a typical experimental result. 130

7.13 Comparison of the experimental and numerical integrated intensity across the plate ($T_p = 485^oK$, $T_{max} = 300^oK$, $T_{min} = 300^oK$, $DP = 5(cm)$, *and* $\Omega = 0.0$) 139

7.14 Comparison of the experimental and numerical integrated intensity across the plate ($T_p = 485^oK$, $T_{max} = 300^oK$, $T_{min} = 300^oK$, $DP = 5(cm)$, *and* $\Omega = 0.4$) 140

7.15 Thermal image of the warm background radiation source at $T_p = 485^oK$. 143

7.16 Thermal image of the impingement cooled plate at $T_p = 445^oK$. . . . 144

NOMENCLATURE

A	area
a	absorption coefficient
$C_1,\ C_2$	constant in Planck's spectral energy distribution
D	diameter of plume
E	energy
E_I	ionization potential
e	emissive power
h	Planck's constant
I	source function
i	radiation intensity
K	extinction coefficient, $a + \sigma_s$
k	Boltzmann constant
N	number density, particles per unit volume
n	simple refractive index
P	pressure
Q	energy per unit time
q	energy flux, energy per unit area and time
R	radius of plume cross section
S	coordinate along path of radiation
s	scattering cross section
T	absolute temperature
V	volume
x, y, z	coordinates in Cartesian system
Y	coordinate across the plume

α	absorptivity
β	integration constant [Eq. 5-1]
δ	integration constant [Eq. 5-5]
ϵ	emissivity
θ	cone angle, angle from normal of area; scattering angle measured relative to forward direction
λ	wavelength in medium
μ	the quantity cos θ
φ	circumferential angle
ρ	reflectivity
σ_s	scattering coefficient
τ	optical thickness
Ω_0	albedo for scattering
Φ	phase function for scattering
ω	solid angle

Subscripts

a	absorbed
b	blackbody
e	emitted
g	gas
i	incident; incoming; the λ increment
j	the S increment
o	outgoing
p	projected; plate

s	source or scatter
η	wave number-dependent
λ	wavelength-dependent

Superscripts

$'$	directional quantity
$+$	true value, not modified by addition of induced emission
$*$	dummy variable of integration

CHAPTER I

INTRODUCTION

Among the advances in current aerospace technology, there has been a significant growth of research activities in various aspects of radiation heat transfer. The complicated and interesting phenomena associated with the study of energy transfer through participating media that can absorb, emit and scatter radiation has received increased attention in the past three decades and significant advances have been made in the treatment of radiative transfer in the presence of participating media.

The problem of computing the radiation transfer through participating media came into the focus of attention because of various new practical engineering applications, such as rocket propulsion, nuclear explosions, plasma generations for nuclear fusion, and combustion at high pressures and temperatures. The safe operation and testing of a high pressure liquid rocket engine, in particular, the Space Shuttle Main Engine (SSME) is among these applications that has introduced a new opportunity in which the prediction of the radiation transfer through participating media plays an important role in preventative diagnostics.

The development, qualification and reliability improvement testing of a liquid rocket engine can (and has) result(ed) in the loss of a significant number of engines and associated resources including project time. Each qualification or component improvement engine represents a critical program resource which includes the accumulated cost of all test time on the hardware. Protection of high time fleet leader engines during ground testing has become more important as the inventory matures.

The complicated high-pressure cycle of rocket engine propellant path, which

includes cryogenic hydrogen and oxygen, provides many opportunities for external propellant path leaks while the engine is running. This mode of engine failure may be detected and analyzed with sufficient speed to save critical engine test hardware from destruction. The leaks indicate hardware failures which will damage or destroy an engine if undetected.

High pressure staged combustion rocket engines operation on cryogenic hydrogen and oxygen have potential propellant path leaks of both cryogenics and hot gases. In most cycles the hot hydrogen will contain water vapor from the preburner thus providing a strong emission signal. If the hot hydrogen burns in the surrounding air the emission intensity will be very high requiring a large dynamic range on the sensors. Cold leaks of oxygen and hydrogen can only be detected indirectly since H_2 and O_2 do not absorb radiation. All atmospheric cryogenic leaks are surrounded by condensed water droplets which have strong absorption in the 2.5 to 2.9 μm band. The condensed water droplets on the outer edge of the plume also scatter the background radiation. One additional detection method, impingement cooling, may provide excellent detection of cryogenic leaks which impinge on the engine hardware causing sudden surface emission changes.

An advanced propellant path leak detection technique by using state-of-the-art technology of infrared (IR) thermal imaging systems combined with computer, digital image processing and expert systems is proposed for a rocket engine protection system. The high-tech IR detection techniques may be used to replace the existing conventional thermocouple based system for leak detection to provide a non-intrusive, high response gas-leak detection system for safe shut down of the engine. The IR equipment enables us to measure and record the image of temperature distribution over the exterior surface of the engine hardware and to determine whether the engine components are functioning properly.

The objectives of this investigation can be categorized in four parts: (1) develop a theoretical radiation transport model including emission, absorption and scattering; (2) develop a computational model to calculate radiation heat transfer in a participating media; (3) apply this numerical code to a simple leak model to evaluate infrared sensor sensitivity to engine and plume radiation patterns; (4) validate the model results with laboratory scale experiments.

Theoretical study of the radiation heat transfer in an absorbing, emitting and scattering medium is complicated due to the following characteristics of the medium. In a participating medium , absorption, emission and scattering of energy occurs not only at the system boundaries, but also at all locations within the medium. A complete solution of the energy exchange problem requires the knowledge of temperature, radiation intensity, and physical properties at every point within the medium. The mathematics describing the radiation model is inherently complex caused by the non-homogeneity of the temperature field. In addition, the highly non-gray spectral effects of gases are often much more pronounced than for solid surfaces, and a detailed spectrally dependent analysis is required. Most of the simplifications introduced in gas radiation problems are aimed at dealing with one or both of these complexities.

Numerical results are very important since they are the basis for confirming or predicting results from an experimental model. The useful information from numerical results provides excellent guidance to select the best wavelength range for infrared detector, filter wavelength, and equipment set up for generation of better experimental data. From observation of the numerical data and analysis of the available information one can select a more realistic experimental model. Numerical solution of the models is cost effective and timely in assisting in building the experimental set up and avoiding the purchase of high cost experimental

equipment.

Absorption and scattering coefficients are required for calculation of radiation heat transfer in participating media. The absorption of radiation by the gas depends on the radiative properties of the gas. Analytical determination of the absorption coefficient requires quantum-mechanical calculations. Penner [1][1] presented a detailed analytical study of quantum-mechanics for the calculation of absorption coefficients. In the present investigation the absorption coefficients have been taken from Ref. [2] which is based on a combination of experimental data and analytical results.

The feasibility of the infrared detection scheme was evaluated on subscale simulated laboratory plumes to determine sensitivity, signal to noise ratio, and general suitability of IR imaging system for a liquid rocket engine propellant path leak detection. The experimental analysis was undertaken with the objective of testing simple models to predict the amount of radiation coming from a radiation source passing through an absorbing, emitting and scattering medium.

A review of the pertinent experimental and analytical literature is presented in chapter II. In chapter III, the fundamental radiation transport relations in participating media are presented. In chapter IV the physical and geometrical problem is defined, and in chapter V the numerical solution to the transport equation is described. Discussion of the numerical results are presented in chapter VI. The laboratory experimental set-up and the experimental results can be found in chapter VII, and finally chapter VIII presentes the conclusions and recommendations.

---

[1] Numbers in brackets refer to similarly numbered references in the bibliography.

CHAPTER II

LITERATURE REVIEW

Review of literature in the area of gas radiation reveals that most previous researches have studied a one-dimensional problem of parallel plate enclosures [3-8]. One difficulty encountered in studying radiation within absorbing and emitting media is that spectral effects are often much more pronounced in gases than for solid surfaces and accordingly, a more detailed spectrally dependent analysis is required. However because of the complicated analytical nature of the problem, most of the solutions have been obtained by adopting what is called the gray-gas model [1,9].

In the gray-gas assumption, the radiation properties such as absorption and emission coefficients are considered to be independent of wavelength and local thermodynamic conditions such as temperature and pressure. For a medium containing undissociated molecules, this assumption is invalid and may lead to significant errors in calculation of radiative transfer due to the highly wavelength dependent contribution of molecular bands to emission and absorption coefficients. In addition, the final solution is often given in terms of a mean absorption coefficient over the whole spectrum. The impacts of averaging radiative properties have been examined in the studies of atmospheric and astrophysical radiation [10,11] and in the treatments of engineering radiative heat-transfer problems [1,9,12]. This assumption will restrict the applicability of these analyses only to gray gases or to gases that are optically thin at all wavelengths of interest.

Earlier attempts to take into account the non-gray behavior of real gases in the radiative heat-transfer analyses have been reported in [13-16]. These methods required elaborate and time-consuming calculations, and the results are restricted

to the specific gas and geometric considerations. When the gas is neither gray nor optically thin at all wavelengths of interest, it is customary to apply the monochromatic transport equation at a sufficiently large number of wavelength ranges to enable calculation of integrated intensity by a numerical technique.

The radiation properties of water vapor are strongly depend on wavelength and temperature. In order to include the dependence of radiation properties on temperature, which often varies greatly in media of practical interest, it is necessary to acquire a knowledge of the absorption coefficient of water vapor as a function of temperature. In general, the absorption coefficient of a gas is a function of temperature and pressure. In most systems of engineering interest, the temperature variation is relatively more significant than the pressure by comparison. Consequently, it is assumed that the non-homogeneity along the gas path will be due to the temperature variation alone. The absorption coefficient will be denoted simply as $a_\lambda[T(S), \lambda]$ where T is the temperature, S the path length and λ the wavelength.

The determination of the radiation transfer through such a medium requires knowledge of the monochromatic absorption coefficients a_λ. In theory, the expressions for a_λ can be derived from the applications of quantum and statistical mechanics. The complexity and the many necessary approximations involved in the theoretical determination of a_λ support the experimental determination of radiation transport properties. Many experiments have been developed for infrared measurements of gases at moderate and high temperatures. Extensive data for the monochromatic absorption coefficient of different gases obtained theoretically and experimentally have been reported in the literature [2,11, 17-19]. In the present study, the spectral infrared properties of water vapor have been taken from Ref. [2]. These properties were obtained by curve fitting of the equations from quantum

and statistical mechanics and experimental investigations.

Review of literature related to radiation in a parallel plate enclosure reveals that researchers have given inadequate consideration to the role of radiation when high temperature gases are present. For example, Jakob [20] computes the absorption in a gas layer as radiation energy passes from a hotter to a colder wall. But, the gas is not permitted to re-radiate, as it must under steady state conditions. By ignoring the emission of the gas, Jakob circumvents the problem of computing the temperature distribution of gas; and as a consequence, his analysis does not permit a complete computation of the net heat transfer. A practical procedure has been proposed by Wohlenberg [20] for computing the net heat transfer in a gas-filled parallel plate enclosure. He ignored the local absorption-emission processes, supposing the gas to be isothermal and to radiate as a whole according to Stephan-Boltzman's law. Quantitative thermal measurements of a gas plume require understanding of radiation in the absorbing and emitting media.

An important engineering approach in the study of non-isothermal radiating gas bodies has been made by Hottel and Cohen [21]. They provide interchange factors between finite-sized rectangular gas volumes situated at various orientation with respect to one another. Similar information is also given for surface-to-volume radiation. Such factors are useful when a radiation problem is formulated by subdividing the gas body into a group of finite volumes elements, each of which possesses a uniform temperature different from its neighbors. The approach of the present analysis differs from Hottel and Cohen in that the temperature is permitted to vary continuously throughout the gas.

Geometries of more practical interest have received relatively little attention. Sparrow, Usiskin and Hubbard [22] have considered radiation heat transfer in an absorbing and emitting non-isothermal gray-gas confined within spherical enclo-

sure. Tien and Abu-Romia [23] have examined radiation energy transfer to the outer base region of a semi-infinite cylindrical isothermal gas body. Desoto [24] has developed a method to determine the radiation heat flux to the base region of a gas system with an axisymmetric geometry and axisymmetric property distribution. Einstein [25] has considered radiation heat transfer in an absorbing emitting non-isothermal gray-gas confined within a black-walled cylindrical pipe. Heaslet and Warming [26] and Kesten [27] have developed an analytical and numerical method for predicting radiation transfer in a homogeneous cylindrical medium.

Many of the heat-transfer studies have been concerned with the solutions which were limited to radiation in one-dimensional systems to better understand the results. The astrophysical studies have also emphasized one-dimensional analyses because multidimensional phenomena are of secondary interest when interpreting astronomical observations through the plane, parallel, terrestrial atmosphere. The solution of the transfer equation in two- and three-dimensional slab, cylindrical and spherical media has been presented by Uesugi and Tsujita [28].

In the computation of radiation heat transfer through media containing local inhomogeneities, such as small particles, consideration should be given to the effect of energy scattering. Such media include smoke, dust clouds, fluidized beds of particles, fogs, and low density insulation.

Heat transfer by simultaneous conduction and radiation in thermal radiation absorbing, emitting, and scattering material has been investigated theoretically by Viskanta [3]. The one-dimensional system consisted of two diffuse, non-black, isothermal parallel plates which were filled with an isotropically scattering material. Love and Grosh [4] presented an approximate method for analyzing the problem of radiation heat transfer in an isothermal plane-parallel system of particles which absorb, emit, and scatter energy. Numerical results have been published

for various particle size to wavelength ratios and refractive indices. The scattering effect has been studied extensively and in most cases, the investigators have been interested in particle identification.

It should be pointed out that scattering includes the combined effects of reflection, refraction, diffraction, and transmission of the radiation by the particle. The results of the analysis from Love and Grosh gave an interesting insight into the effect of scattering on radiation heat transfer. Their computation have been made over a range of spherical particle sizes having complex indices of refraction of 1.25-1.25i and 2.0-0.6i and compared with the results for isotropic scattering for wall emmisivities of 0.9. These refractive indices correspond roughly to iron and carbon, respectively, in the visible wavelengths. Their results indicated that, for small optical spacings and for small values of particle size parameter, the effect of anisotropic scattering is closely approximated by the isotropic case. This would suggest that the assumption of isotropic scattering may be made with little error for many systems.

Another interesting result was that infinite clouds of particles which scatter radiation, such as carbon particles may not be considered black. Since most clouds of particles may be composed of various sizes and shape of the particles with random orientation and unknown refractive indices, analytical determination of the scattering function may be impossible. However, because of the random nature of the clouds, the scattering was considered axially symmetric and the above analysis would be used with experimentally determined scattering function.

In the present investigation, geometry of the plume has been assumed to be a cylindrical shape and the computation of infrared radiation heat transfer through participating media has been accomplished with absorbing, emitting and scattering medium which is a non-gray and non-isothermal gas.

CHAPTER III

FUNDAMENTALS OF RADIATION IN ABSORBING, EMITTING, AND SCATTERING MEDIA

Theoretical study of the radiation heat transfer in an absorbing, emitting, and scattering medium is complicated due to the following characteristics of the medium. In a participating medium, absorption, emission and scattering of energy occur not only at the system boundaries, but also at all locations within the medium. A complete solution of the energy exchange problem requires the knowledge of temperature, radiation intensity, and physical properties at every point within the medium. The mathematics describing the radiation model is inherently complex caused in part by the non-homogeneity of temperature field. In addition, the highly non-gray spectral effects of gases are often much more pronounced than for solid surfaces, and a detailed spectrally dependent analysis is required. Most of the simplifications introduced in gas radiation problems are aimed at dealing with one or both of these complexities.

In this chapter, the fundamental concepts are introduced for radiant intensity within a medium, and for the effects of absorption, emission, and scattering on radiant propagation. The following drivations are based on derivation in Ref. [29].

3.1 Physical Mechanisms of Absorption, Emission, and Scattering

3.1.1 Absorption and Emission

The mechanisms of radiation in absorbing, emitting and scattering media must be treated accordingly. The gas properties generally exhibit very irregular wavelength dependencies. As a result, the absorption or emission by gases is

significant only in certain wavelength regions, especially at temperature levels below a few thousand degrees kelvin.

The radiation emitted from a solid actually originates within the solid (i.e., not at the solid surface) so the solid can be considered an absorbing and emitting medium similar to a gas. The differences in emission spectra are caused by the various types of energy transitions that occur within the medium. A gas has different types of transitions, a fact which leads to a less continuous spectrum than that for a solid. The energy transitions that account for radiation emission and absorption will now be discussed.

A radiating gas can be composed of molecules, atoms, ions, and free electrons. These particles can have various energy levels associated with them. In a molecule, for example, the atoms form a dynamic system that has certain vibrational and rotational modes. These modes have specific energy levels associated with them. A schematic diagram of the energy levels for an atom, ion, or electron is shown in Figure 3.1. The zero energy level is assigned to the ground state (lowest energy bound state), with the higher bound states being at positive energy levels. The energy E_I in Figure 3.1 is the ionization potential, that is, the energy required to produce ionization from the ground state. Energies above E_I denote that ionization has taken place and free electrons have been produced.

It is convenient to discuss the radiation process by utilizing a photon or quantum point of view. The photon is the basic unit of radiation energy. Radiative emission consists of the release of photons of energy, and absorption is the capture of photons by a particle. When a photon is emitted or absorbed, the energy of the emitting or absorbing particle is correspondingly decreased or increased. Figure 3.1 is a diagram of the three types of transitions that can occur. These are bound-bound, bound-free, and free-free.

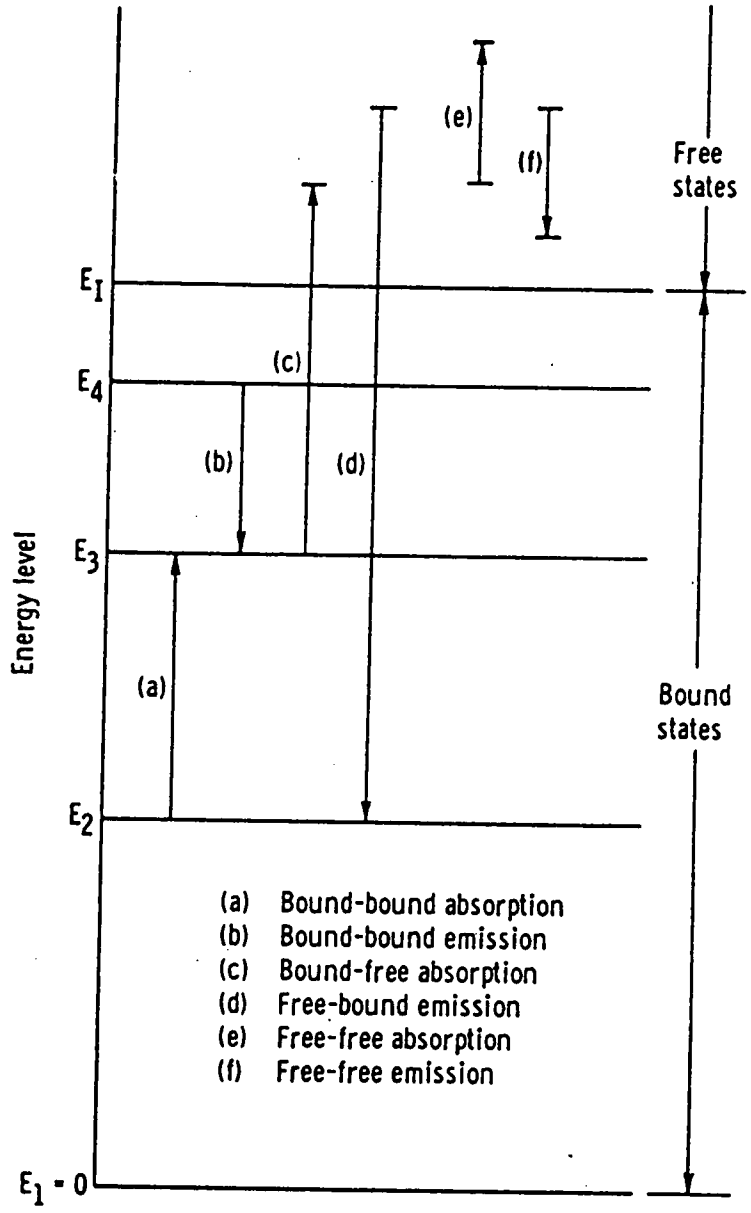


Figure 3.1 Schematic diagram of energy states and transition for atom, ion, or electron.

The magnitude of the energy transition is related to the frequency of the emitted or absorbed radiation. The energy of a photon is $h\nu$, where h is Planck's constant and ν is the frequency of the photon energy. For an energy transition, say from bound state E_3 down to bound state E_2 in Figure 3.1, a photon is emitted with energy $E_3 - E_2 = h\nu$. The frequency of the emitted energy is then $\nu = (E_3 - E_2)/h$ so that a fixed frequency is associated with the transition from a specific energy level to another. Thus, in the absence of other effects, the emitted radiation will be in the form of a spectral line. Conversely, in a transition between two bound states when a particle absorbs energy, the quantum nature of the process dictates that the absorption is such that the particle can only go to one of the discrete higher energy levels. Consequently, the frequency of the photon energy must have one of certain discrete values for the photon to be absorbed. For example, a particle in the ground state in Figure 3.1 may absorb photons with frequencies $(E_2 - E_1)/h$, or $(E_3 - E_1)/h$, or $(E_4 - E_1)/h$ and undergo a transition to a higher bound energy level. Photons with other frequencies in the range $0 < \nu < E_I/h$ cannot be absorbed.

When a photon is absorbed or emitted by an atom or molecule and there is no ionization or recombination of ions and electrons, the process is termed a bound-bound absorption or emission (see processes *a* and *b* in Figure 3.1). The atom or molecule moves from one quantized bound energy state to another. These states can be rotational, vibrational, or electronic in molecules, and electronic in atoms. Since bound-bound energy changes are associated with specific energy levels, the absorption and emission coefficients will be sharply peaked functions of frequency in the form of a series of spectral lines.

The vibrational energy modes are always coupled with rotational modes. The rotational spectral lines superimposed on the vibrational line give a band of closely

spaced spectral lines. If these are averaged together into one continuous region, it becomes a vibration-rotational band. Rotation transitions within a given vibrational state are associated with energies at long wavelength, $\sim 8 - 1000\mu m$. Vibration-rotation are at infrared energies of about 1.5-20 μm, and at portions of ultraviolet and infrared near the visible region.

Process c in Figure 3.1 is a bound-free absorption (photoionization). An atom absorbs a photon with sufficient energy to cause ionization. The resulting ion and electron are free to take on any kinetic energy; hence, the bound- free absorption coefficient is a continuous function of photon energy frequency ν as long as the photon energy $h\nu$ is sufficiently large to cause ionization. The reverse (process d in Figure 3.1) is a free-bound transition (photorecombination). Hence an ion and free electron combine, a photon of energy is released, and energy of the resulting atom drops to that of a discrete bound state. The free-bound emission produces a continuous spectrum, as the combining particle can have any initial kinetic energy.

In an ionized gas, a free electron can pass near an ion and interact with its electric filed. This can produce a free-free transition. The electron can absorb a photon (process e in Figure 3.1) thereby going to a higher kinetic energy, or it can emit a photon (process f) and drop to a lower free energy. Since the initial and final free energies can have any values, a continuous absorption or emission spectrum is produced.

3.1.2 The Scattering of Energy

Scattering is taken here to be any encounter between a photon and one or more other particles during which the photon does not lose its entire energy. It may undergo a change in direction, and a partial loss or a gain of energy. In any of these cases, the photon is said to have been scattered. The scattering coefficient, $\sigma_{s\lambda}$, is

the inverse of the mean free path that a photon of wavelength λ will travel before undergoing scattering. The scattering can be characterized by four types of events: elastic scattering in which the energy (and, therefore, frequency and wavelength) of the photon is unchanged by the scattering, inelastic scattering in which the energy is changed, isotropic scattering in which scattering into any direction is equally likely, and anisotropic scattering in which there is a distribution of scattering direction. Elastic-isotropic scattering is the most amenable to analysis without resorting to sophisticated analytical or numerical techniques. Most scattering events of importance in engineering are elastic, or very nearly so, and the analysis given here will consider only the elastic case.

3.2 Definition of Radiation Intensity

The radiation emitted in any direction will be defined in terms of intensity. Radiation intensity is a convenient quantity for use in problems dealing with radiative transfer through absorbing, emitting and scattering media. This convenience arises chiefly because of certain invariance properties. The spectral intensity refers to radiation in an interval $d\lambda$ around a single wavelength and will be given by i'_λ. The subscripts denote that one wavelength is being considered and the prime denotes that radiation per unit solid angle in a single direction is being considered. The emitted spectral intensity is defined as the energy emitted per unit time per unit small wavelength interval around the wavelength λ, per unit elemental projected surface area normal to the (θ, ϕ) direction and into a unit elemental solid angle centered around the direction (θ, ϕ)(see Figure 3.2).

$$i'_\lambda \equiv \frac{d^3 Q'_\lambda}{dA d\omega d\lambda} \qquad (3-1)$$

Where the third-derivative notation d^3 emphasizes that emitted energy Q is a function of three differential quantities.

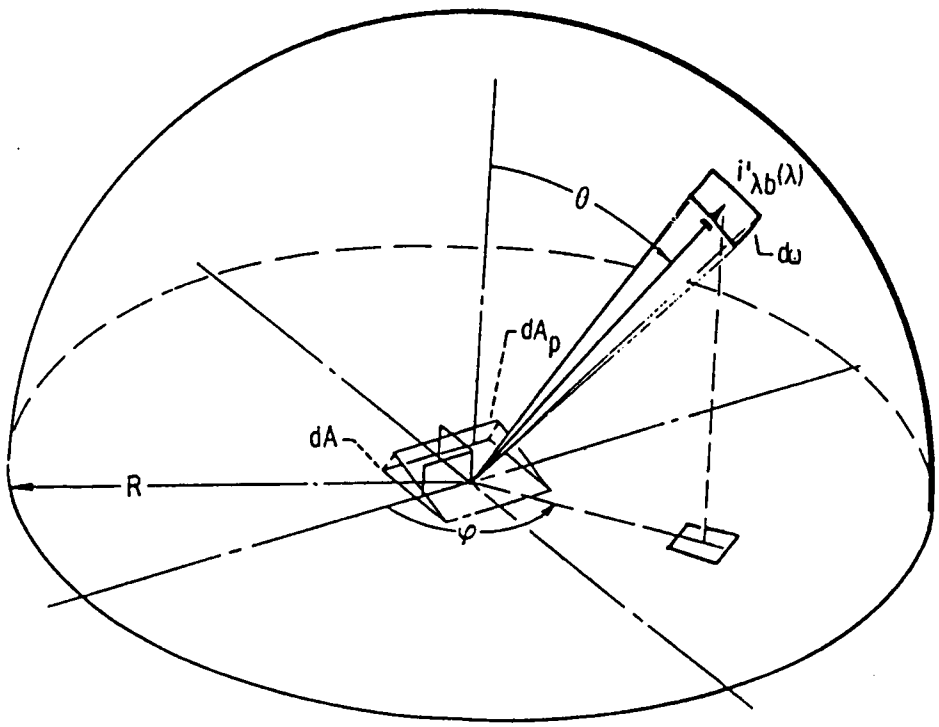


Figure 3.2 Spectral emission intensity from black surface.

3.3 The Attenuation of Energy by Absorption and Scattering

Consider spectral radiation of intensity i'_λ impinging normally on a layer of gas of thickness dS as in Figure 3.3. As the radiation passes through this absorbing medium, its intensity is reduced by absorption. The change in intensity has been found experimentally to depend on the magnitude of the local intensity. If a coefficient of proportionality K_λ which depends on the local properties of the medium is introduced, the decrease is given by

$$di'_\lambda = -K_\lambda(S) i'_\lambda dS. \qquad (3-2)$$

The K_λ is the extinction coefficient of the gas in the layer; it is a physical property of the gas and has units of reciprocal length. It is a function of the temperature T and wavelength λ of the incident radiation. The extinction coefficient is composed of two parts, an absorption coefficient $a_\lambda(\lambda, T)$ and a scattering coefficient $\sigma_{s\lambda}(\lambda, T)$

$$K_\lambda = K_\lambda(\lambda, T) = a_\lambda(\lambda, T) + \sigma_{s\lambda}(\lambda, T). \qquad (3-3)$$

Integrating (3-2) over path length S gives

$$\int_{i'_\lambda(0)}^{i'_\lambda(S)} \frac{di'_\lambda}{i'_\lambda} = -\int_0^S K_\lambda(S^*) dS^* \qquad (3-4)$$

where $i'_\lambda(0)$ is the intensity entering the layer, and S^* is a dummy variable of integration. Carrying out the integration on the left side of (3-4) yields

$$i'_\lambda(S) = i'_\lambda(0) exp\left[-\int_0^S K_\lambda(S^*) dS^*\right] \qquad (3-5)$$

Equation (3-5) is known as Bouguer's law; it shows that, as a consequence of the proportionality in (3-5), the intensity of monochromatic radiation along a path

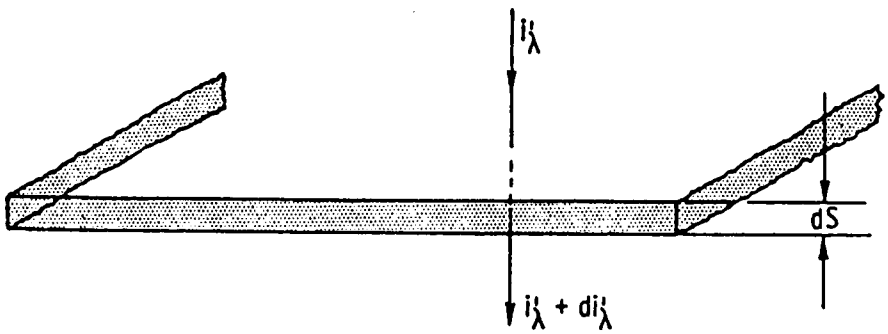


Figure 3.3 Intensity incident normally on absorbing layer of thickness dS.

is attenuated exponentially while it passes through an absorbing medium. The exponent is equal to the integral of the local extinction coefficient over the path length traversed by the radiation.

3.3.1 Optical Thickness

The exponential factor in (3-5) is often written in an alternative form by defining the dimensionless quantity

$$\tau_\lambda(S) \equiv \int_0^S K_\lambda(S^*)dS^*, \qquad (3-6)$$

so that (3-5) becomes

$$i'_\lambda(S) = i'_\lambda(0)exp[-\tau_\lambda(S)]. \qquad (3-7)$$

The quantity $\tau_\lambda(S)$ is the optical thickness or opacity of the layer of thickness S and is a function of all the values of K_λ between 0 and S. Because K_λ is a function of the local temperature T and wavelength λ, the optical thickness becomes a function of all these conditions along the path between 0 and S.

The optical thickness is a measure of the ability of a given path length of gas to attenuate radiation of a given wavelength. A large optical thickness means large attenuation. The quantity τ_λ is a convenient dimensionless parameter that will occur in the solution of radiation problems.

3.3.2 The Absorption Coefficient

The absorption coefficient $a_\lambda(\lambda, T)$ usually varies strongly with wavelength and often varies substantially with temperature. Considerable analytical and experimental effort has been expended in the determination of a_λ, which requires detailed quantum-mechanical calculations. Except for the simplest gases, such as

atomic hydrogen, the calculations are very tedious and require many simplifying assumptions.

Dealing with spectral line emission and absorption is one of the computational difficulties encountered in analyses of radiant energy transfer through gases. Incident radiation at wavelengths near a line center will be strongly absorbed, while radiation of only a slightly different wavelength may experience almost no attenuation. Integrating line absorption coefficients with respect to wavelength to obtain band or total absorption coefficients is generally tedious. These averaged coefficients are used in certain calculation methods of radiation transfer.

3.3.3 True Absorption Coefficient

Bouguer's law in the form of Eq. (3.5) gives the attenuation of a beam of radiation upon passing through a volume of non-emitting non-scattering gas along a path of length S as would be observed by detectors of incident and emerging radiation. Such observed information could be used in determining a_λ. Actually, as radiation energy passes through a gas, not only is absorbed, but there is also an additional phenomenon in that its presence stimulates some of the gas atoms or molecules to emit energy. This is not the ordinary or spontaneous emission. Spontaneous emission is the result of the excited state of the gas being unstable and decaying spontaneously to a state of lower energy. The emission resulting from the presence of the radiation field is termed stimulated or induced emission and is a negative absorption.

The induced emission constitutes a portion of the intensity that is observed in the beam emerging from the gas volume. Consequently, the amount of energy that is actually absorbed by the gas is greater than that found by taking the difference between the entering and leaving intensities. This is because the observed emerging

intensity is the result of the actual absorption modified by the addition of induced emission along the path of the beam. The actual absorbed energy should be calculated using a true absorption coefficient $a_\lambda^+(\lambda,T)$, which is larger than the absorption coefficient $a_\lambda(\lambda,T)$ calculated by using observed attenuation data and Bouguer's law. The "true" law for absorption along path S is then

$$i'_\lambda(S) = i'_\lambda(0)exp\left[-\int_0^S a_\lambda^+(S^*)dS^*\right]. \qquad (3-8)$$

Statistical-machanics considerations give the relation between $a_\lambda(\lambda,T)$ and $a_\lambda^+(\lambda,T)$ for a gas with refraction index n=1 as

$$a_\lambda(\lambda,T) = \left[1 - exp(-\frac{C_2}{\lambda T})\right] a_\lambda^+(\lambda,T). \qquad (3-9)$$

Examination of Eq. (3.9) shows that, because of the negative exponential term, a_λ^+ will always be larger than a_λ.

Because the induced emission depends on the incident radiation field, it is usually grouped together with the true absorption, thereby yielding the absorption coefficient a_λ. The emission term in the equation of radiation transfer then includes only the spontaneous emission and consequently depends only on the local conditions of the gas.

The exponential term in (3-9) is small except at large values of λT. Thus a_λ and a_λ^+ are nearly equal except at large values of λT (long wavelengths and/or high temperatures). The values are within 1% for λT less than 3120 $\mu m.^oK$ and within 5% for λT less than 4800 $\mu m.^oK$.

3.3.4 The Scattering Coefficient

The extent of scattering can be viewed in terms of the scattering cross section S. This is the apparent area that an object presents to an incident beam insofar as

the ability of the object to deflect radiation from the beam is concerned. In addition, depending on the particle size, the scattering cross section may depend upon the shape and material of the scattering body and the wavelength, polarization, and coherence of the incident radiation.

The scattering cross section can be determined experimentally by measuring the amount of radiation in a beam that is able to penetrate through a cloud of scattering particles. The ratio of the scattered portion $di'_{\lambda,s}$ of the incident intensity to the intensity i'_λ of the incident beam is equal to the ratio of the apparent projected scattering area $d^2A_{s\lambda}$ occupied by all scattered particles to the cross-sectional area of the incident beam dA. This gives the following for a beam traveling a differential distance within a medium in which it encounters the scattering area $d^2A_{s\lambda}$

$$\frac{di'_{\lambda,s}}{i'_\lambda} = \frac{d^2A_{s\lambda}}{dA}. \qquad (3-10)$$

The apparent scattering area presented by a group of the scattering particles is related to the average scattering areas of the individual particles by

$$d^2A_{s\lambda} = s_\lambda N_s dV = s_\lambda N_s dA dS \qquad (3-11)$$

where N_s is the number density of the particles, s_λ is the average scattering cross section of the particles, and dV is a differential volume of the particle containing cloud as shown in Figure 3.4. Inserting (3-11) into (3-10) gives the change di'_λ of the intensity as a result of scattering from the incident beam:

$$-\frac{di'_\lambda}{i'_\lambda} = \frac{di'_{\lambda,s}}{i'_\lambda} = \frac{s_\lambda N_\lambda dA dS}{dA} = s_\lambda N_\lambda dS. \qquad (3-12)$$

By integrating (3-12) over a path from 0 to S, the intensity is found at S as a result of attenuation by scattering from the beam with original intensity $i'_\lambda(0)$:

$$i'_\lambda(S) = i'_\lambda(0) exp\left(-\int_0^S s_\lambda N_\lambda dS^*\right). \qquad (3-13)$$

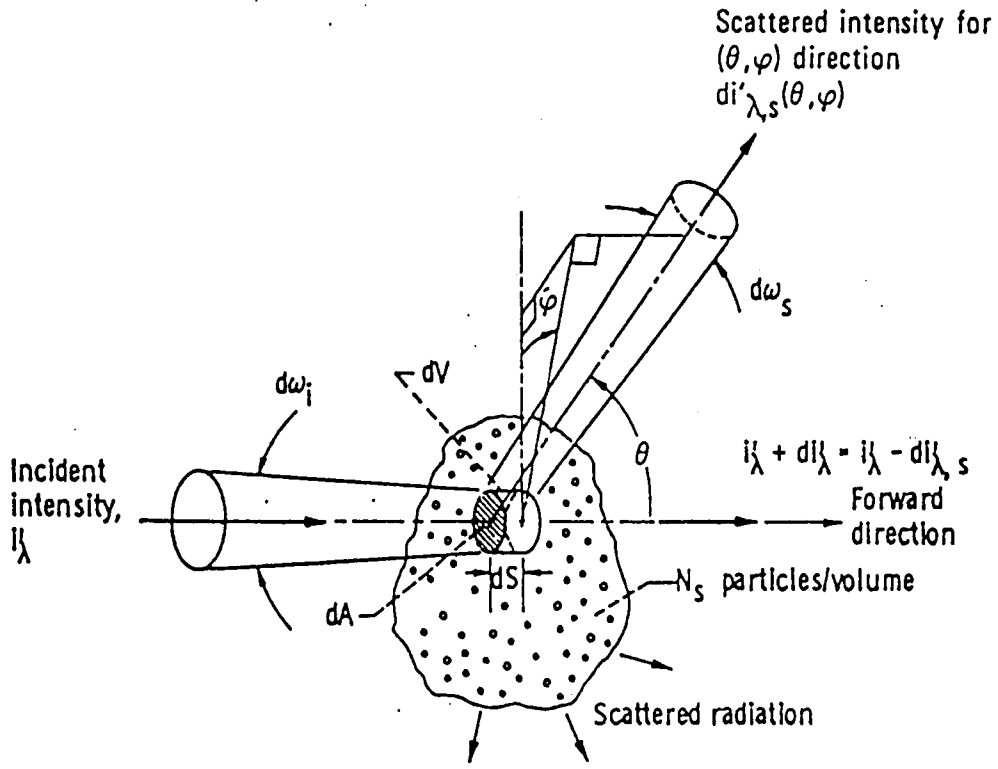


Figure 3.4 Scattering of intensity into direction (θ, ϕ) from incident radiation within solid angle $d\omega_i$.

The portion of the incident intensity that was scattered away along the path is thus

$$i'_\lambda(0) - i'_\lambda(S) = i'_\lambda(0)\left[1 - exp\left(-\int_0^S s_\lambda N_\lambda dS^*\right)\right]. \qquad (3-14)$$

The scattering coefficient $\sigma_{s\lambda}$ is defined to be

$$\sigma_{s\lambda} \equiv s_\lambda N_\lambda, \qquad (3-15)$$

so that (3-13) becomes

$$i'_\lambda(S) = i'_\lambda(0) exp\left[-\int_0^S \sigma_s \lambda(S^*) dS^*\right]. \qquad (3-16)$$

This is the pure-scattering from of Bouguer's law.

3.4 The Emission of Energy

Consider an elemental volume dV of gas as shown in Figure 3.5 The true absorption coefficient within volume is $a^+_\lambda(\lambda, T)$ and is considered constant over dV. Let dV be placed at the center of a large black hollow of radius R at uniform temperature T. The space between dV and the sphere wall is filled with a non-participating medium. The spectral intensity incident at dA_S location on dV from an element dA on the surface of the enclosure is,

$$i'_\lambda(0) = i'_{\lambda b}(\lambda, T). \qquad (3-17)$$

The change of the intensity as a result of true absorption in dV is

$$di'_\lambda = -i'_\lambda(0)[1 - exp(-a^+_\lambda dS)] = -i'_{\lambda b}(\lambda, T)[1 - exp(-a^+_\lambda dS)] \qquad (3-18)$$

Since the true absorption coefficient has been used, this does not include induced emission. Let dV be small enough so that $a^+_\lambda dS$ is sufficiently small to allow the approximation

$$di'_\lambda = -i'_{\lambda b}(\lambda, T)[1 - exp(-a^+_\lambda dS)] \simeq -i'_{\lambda b}(\lambda, T) a^+_\lambda dS \qquad (3-19)$$

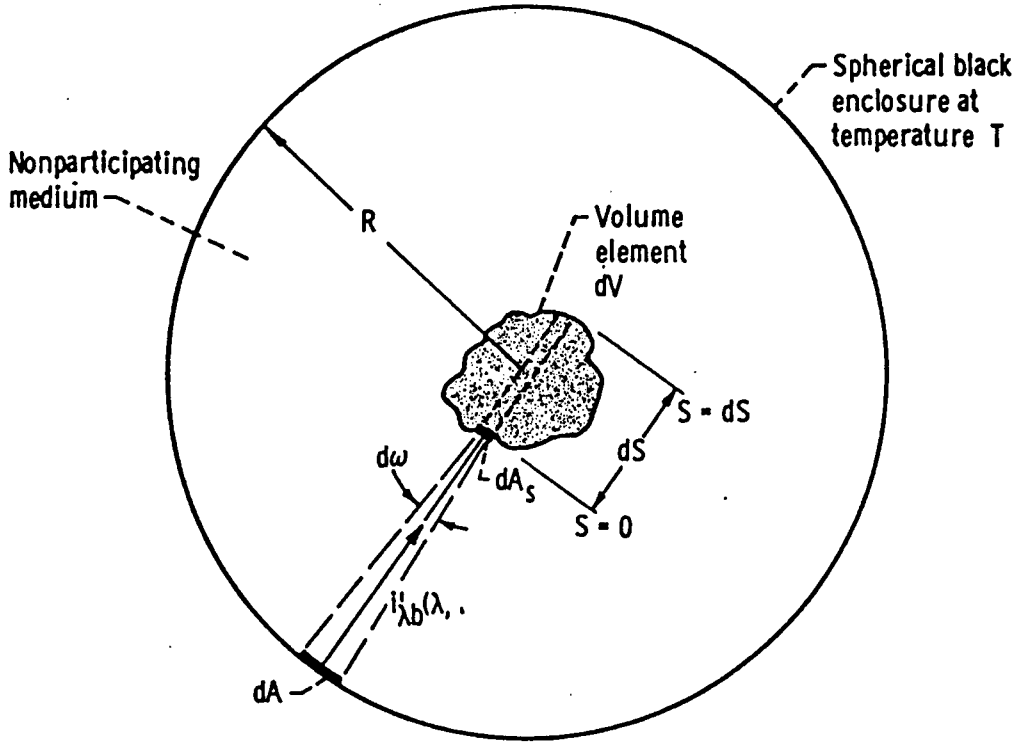


Figure 3.5 Geometry for derivation of emission from volume of gas.

Equation (3-19) is also evident from the differential form (3-2). The energy absorbed by the differential subvolume dS dA_S from this incident radiation is

$$d^5Q'_{\lambda,a} = -di'_\lambda dA_S d\lambda d\omega \qquad (3-20)$$

Where $d\omega = \frac{dA}{R^2}$ and dA_S is a projected area normal to $i'_\lambda(0)$. Substituting (3-19) in (3-20) results in

$$d^5Q'_{\lambda,a} = i'_{\lambda b}(\lambda,T)a^+_\lambda dS dA_S d\lambda d\omega. \qquad (3-21)$$

The energy emitted by dA and absorbed by all of dV is found by integrating over dV; that is,

$$d^4Q'_{\lambda,a} = \int_{dV} d^5Q'_{\lambda,a} = a^+_\lambda i'_{\lambda b}(\lambda,T)dV d\lambda d\omega \qquad (3-22)$$

where $d\omega$ is the solid angle subtended by dA when viewed from dV. To account for all energy incident upon dV from the entire spherical enclosure , integration is carried out over all such solid angles to give

$$d^3Q_{\lambda,a} = \int_\omega d^4Q'_{\lambda,a} = a^+_\lambda i'_{\lambda b}(\lambda,T)dV d\lambda \int_{4\pi} d\omega$$

$$= 4\pi a^+_\lambda i'_{\lambda b}(\lambda,T)dV d\lambda = 4a^+_\lambda e_{\lambda b}(\lambda,T)dV d\lambda \qquad (3-23)$$

where $e_{\lambda b}$ is the blackbody spectral emissive power.

To maintain equilibrium in the enclosure, dV must emit an amount of energy equal to that absorbed. Hence, the energy emitted by an isothermal volume element in equilibrium with its surroundings is

$$d^3Q_{\lambda,e} = d^3Q_{\lambda,a} = 4a^+_\lambda(\lambda,T)e_{\lambda b}(\lambda,T)dV d\lambda. \qquad (3-24)$$

This result includes both spontaneous emission and emission induced by the incident equilibrium radiation field. For only spontaneous emission, the coefficient a_λ would be used. The shape of the element dV is arbitrary; however, its size

must be small enough to justify the approximation (3-19) and small enough so that energy emitted within dV escapes before reabsorption within dV. Further, the gas must be in thermodynamic equilibrium with respect to its internal energy.

When the spontaneously emitted intensity is the same for all directions the radiation intensity emitted spontaneously by a volume element into any direction is

$$di'_{\lambda,e}(\lambda,T) = \frac{d^3Q_{\lambda,e}}{4\pi dA_P d\lambda} = \frac{a_\lambda(\lambda,T)e_{\lambda b}(\lambda,T)dS}{\pi} = a_\lambda(\lambda,T)i'_{\lambda,b}(\lambda,T)dS \quad (3-25)$$

Where dA_P is the projected area of dV normal to the direction of emission, and dS is the mean thickness of dV parallel to the direction of emission (that is, $dS = \frac{dV}{dA_P}$).

3.5 Incoming Scattering

The scattering relations in sec. 3.3.4 were concerned with the portion of the intensity in an incident beam that is lost as a result of being scattered away along a path. One also needs to know how much the intensity can be increased by the scattering into a path from other directions. To calculate this , the directional distribution of the scattered radiation is needed; this is in terms of an angularly dependent phase function.

3.5.1 The Phase Function

Consider the radiation within solid angle $d\omega_i$ that is incident on area dA in figure 3.4. The portion of the incident intensity that is scattered away in dS is given by (3-12) and (3-15) as

$$di'_{\lambda,s} = \sigma_{s,\lambda} i'_\lambda dS \quad (3-26)$$

The $di'_{\lambda,s}$ is the spectral energy scattered within path length dS per unit incident solid angle and area normal to the incident beam:

$$di'_{\lambda,s} = \frac{d^4 Q'_{\lambda,s}}{d\omega_i dA d\lambda} \qquad (3-27)$$

As shown by Figure 3.4, the scattering energy produces an intensity distribution as a function of angle θ measured relative to the forward direction and the circumferential angle ϕ. A phase function $\Phi(\theta,\phi)$ will be defined to describe the angular distribution of the scattered energy.

The scattered intensity in any direction (θ,ϕ) is defined as the energy scattered in that direction per unit solid angle of the scattered direction and per unit area and solid angle of the incident radiation:

$$di'_{\lambda,s}(\theta,\phi) \equiv \frac{spectral\ energy\ scattered\ in\ direction(\theta,\phi)}{d\omega_s dA d\omega_i d\lambda} = \frac{d^5 Q'_{\lambda,s}(\theta,\phi)}{d\omega_s dA d\omega_i d\lambda} \qquad (3-28)$$

The directional magnitude of $di'_{\lambda,s}(\theta,\phi)$ is related to the entire intensity $di'_{\lambda,s}$ scattered away from the incident radiation by the phase function, such that

$$di'_{\lambda,s}(\theta,\phi) = di'_{\lambda,s}\frac{\Phi(\theta,\phi)}{4\pi} = \sigma_{\lambda s} i'_\lambda dS \frac{\Phi(\theta,\phi)}{4\pi} \qquad (3-29)$$

To better understand the phase function, note that the spectral energy per unit $d\lambda, d\omega_i$, and dA scattered into $d\omega_s$ is $di'_{\lambda,s}(\theta,\phi)d\omega_s$, and hence that scattered into all $d\omega_s$ is $\int_{\omega_s=4\pi} di'_{\lambda,s}(\theta,\phi)d\omega_s$. However, the scattered energy per unit $d\lambda, d\omega_i$, and dA, is $di'_{\lambda,s}$ from (3-27) so that

$$di'_{\lambda,s} = \int_{\omega_s=4\pi} di'_{\lambda,s}(\theta,\phi)d\omega_s \qquad (3-30)$$

Using (3-29) to eliminate $di'_{\lambda,s}$ gives the phase function as

$$\Phi(\theta,\phi) = \frac{di'_{\lambda,s}(\theta,\phi)}{(1/4\pi)\int_{\omega_s=4\pi} di'_{\lambda,s}(\theta,\phi)d\omega_s} \qquad (3-31)$$

Thus, $\Phi(\theta,\phi)$ has the physical interpretation of being the scattered intensity in a direction, divided by the intensity that would be scattered in that direction if the scattering were isotropic. For isotropic scattering, then, $\Phi = 1$. By integrating (3-31) over all $d\omega_s$, it becomes evident that $\Phi(\theta,\phi)$ is a function normalized such that

$$\frac{1}{4\pi}\int_{\omega_s=4\pi}\Phi(\theta,\phi)d\omega_s = 1 \qquad (3-32)$$

3.5.2 Augmentation of Intensity by Incoming Scattering

The local intensity along a path will be enhanced by radiation scattered into the direction being considered. To compute the scattering from all directions into the direction of $i'_\lambda(S)$, consider the radiation incident at angle (θ,ϕ) as shown in Figure 3.6. This radiation has intensity $i'_\lambda(\theta,\phi)$, and in the process of going through the volume element dV it will pass through a path length $dS/cos\theta$. From Eq. (3-29) oriented with respect to the present coordinate system, the intensity scattered from $i'_\lambda(\theta,\phi)$ into the direction of i'_λ is

$$di'_{\lambda,s} = \sigma_{s\lambda}i'_{\lambda,s}(\theta,\phi)\frac{dS}{cos\theta}\frac{\Phi(\theta,\phi)}{4\pi} \qquad (3-33)$$

However, from (3-28), $i'_{\lambda,s}$ is an intensity defined as energy in the scattered direction per unit $d\lambda$, per unit scattered solid angle, per unit incident solid angle $d\omega_i$, and per unit area normal to the incident intensity. This is area normal to $i'_\lambda(\theta,\phi)$, which is dA cos θ. Then the spectral energy scattered into the S direction as a result of $i'_\lambda(\theta,\phi)$ is, by use of (3-33),

$$d^5Q'_{\lambda,s} = di'_{\lambda,s}d\omega d\omega_i d\lambda dAcos\theta$$

$$= \sigma_{s\lambda}i'_\lambda(\theta,\phi)\frac{dS}{cos\theta}\frac{\Phi(\theta,\phi)}{4\pi}d\omega d\omega_i d\lambda dAcos\theta$$

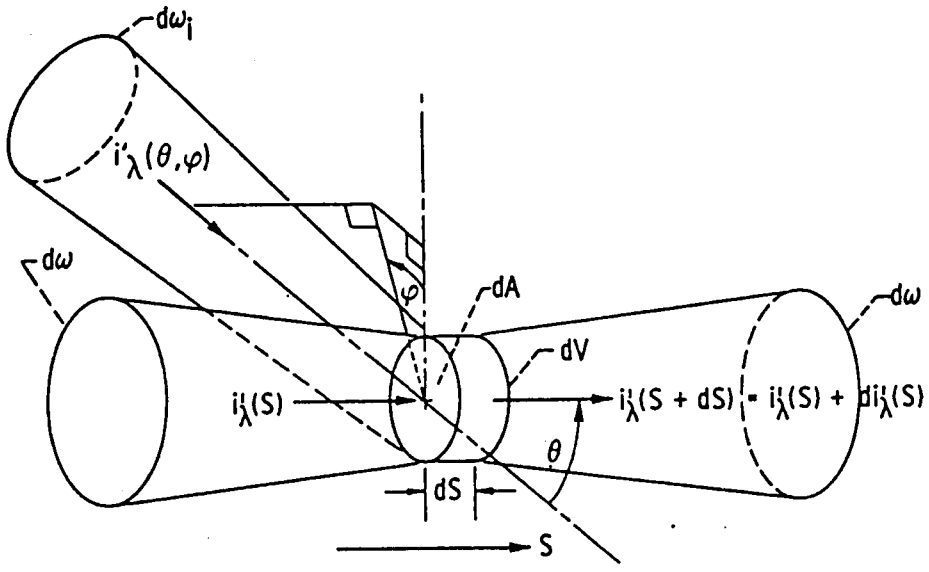


Figure 3.6 Scattering of energy into S direction.

$$d^5Q'_{\lambda,s} = \sigma_{s\lambda} i'_\lambda(\theta,\phi) dS \frac{\Phi(\theta,\phi)}{4\pi} d\omega d\omega_i d\lambda dA$$

The contribution of this scattered energy to the spectral intensity in the S direction is then

$$\frac{d^5Q'_{\lambda,s}}{dAd\omega d\lambda} = \sigma_{s\lambda} i'_\lambda(\theta,\phi) \frac{\Phi(\theta,\phi)}{4\pi} d\omega_i dS. \qquad (3-34)$$

To account for the scattering contributions by the incident intensities from all direction, one integrates over all $d\omega_i$ to obtain

$$\int_{\omega_i=4\pi} \frac{d^5Q'_{\lambda,s}}{dAd\omega d\lambda} = \frac{dS}{4\pi} \sigma_{s\lambda} \int_{\omega_i=4\pi} i'_\lambda(\theta,\phi)\Phi(\theta,\phi) d\omega_i \qquad (3-35)$$

The scattering particles have been assumed randomly oriented so that the scattering cross section $\sigma_{s,\lambda}$ is independent of the incident direction. The augmentation of intensity in direction S by incoming scattering is then

$$\frac{di'_\lambda}{dS} = \frac{\sigma_{s\lambda}}{4\pi} \int_{\omega_i=4\pi} i'_\lambda(\theta,\phi)\Phi(\theta,\phi) d\omega_i. \qquad (3-36)$$

3.6 The Equation of Transfer

The equation of transfer in a medium will now be derived. This will describe the intensity of radiation at any position along its path through an absorbing, emitting, and scattering medium.

3.6.1 Derivation

Bouguer's law, Eq. (3-5), accounts for attenuation by absorption and scattering. The equation of transfer is an extension to include the contributions to the radiation intensity by emission and incoming scattering along the path.

Consider radiation of intensity $i'_\lambda(S)$ within a region of absorbing, emitting, and scattering medium (Figure 3.7). Attention is directed to the change of intensity as the radiation passes through a distance dS. Using Eq. (3-2) gives the

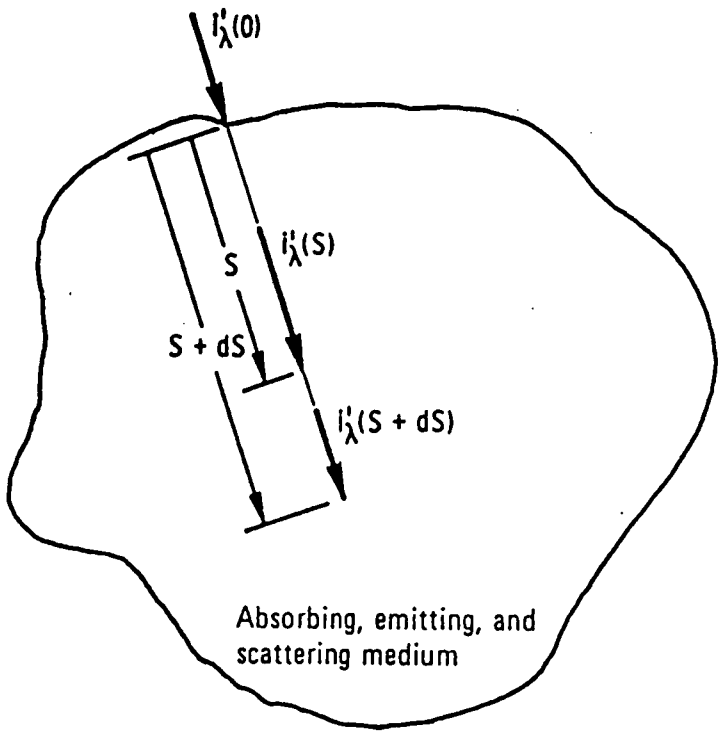


Figure 3.7 Geometry for direction of equation of transfer.

decrease due to absorption as

$$di'_{\lambda,a} = -a_\lambda(S)i'_\lambda(S)dS. \qquad (3-37)$$

Assuming the radiation along the path is in local thermodynamic equilibrium, the spontaneous emission contribution by the medium along the path length dS to the intensity in the S direction is given by Eq. (3-25) as

$$di'_{\lambda,e} = a_\lambda(S)i'_{\lambda,b}(S)dS \qquad (3-38)$$

From Eqs. (3-12), (3-15), (3-36), and Figure 3.5, the sum of the attenuation by scattering and the gain by incoming scattering in direction S can be written as

$$di'_{\lambda,s} = -\sigma_{s\lambda}(S)i'_\lambda(S)dS + \frac{dS\sigma_{s\lambda}}{4\pi}\int_{\omega_i=4\pi} i'_\lambda(S,\omega_i)\Phi(\lambda,\omega,\omega_i)d\omega_i \qquad (3-39)$$

Adding (3-37)-(3-39) gives, for the change in intensity with S in the solid angle $d\omega$ about the direction of S,

$$\frac{di'_\lambda}{dS} = -a_\lambda i'_\lambda(S) + a_\lambda i'_{\lambda,b}(S) - \sigma_{s\lambda}i'_\lambda(S) + \frac{\sigma_{s\lambda}}{4\pi}\int_{\omega_i=4\pi} i'_\lambda(S,\omega_i)\Phi(\lambda,\omega,\omega_i)d\omega_i \qquad (3-40)$$

The first term on right hand side of Eq. (3-40) is the loss by absorption(including the contribution by induced emission). The second term is gain by emission (not including induced emission). The third and forth terms are loss by scattering and gain by scattering into S direction respectively.

The two terms represent decrease by absorption and scattering are combined to give the equation of transfer for absorbing, emitting, and scattering media:

$$\frac{di'_\lambda}{dS} = -K_\lambda i'_\lambda(S) + a_\lambda i'_{\lambda,b}(S) + \frac{\sigma_{s\lambda}}{4\pi}\int_{\omega_i=4\pi} i'_\lambda(S,\omega_i)\Phi(\lambda,\omega,\omega_i)d\omega_i \qquad (3-41)$$

where $K_\lambda = a_\lambda + \sigma_{s\lambda}$ is the extinction coefficient and is a function of position S.

The albedo for scattering, from Ref.[29], Ω_0, defined as the ratio of the scattering coefficient to the extinction coefficient:

$$\Omega_{0\lambda} \equiv \frac{\sigma_{s\lambda}}{a_\lambda + \sigma_{s\lambda}} \qquad (3-42)$$

For scattering alone $\Omega_{0\lambda} \to 1$, while for absorption alone $\Omega_{0\lambda} \to 0$.

Dividing both sides of Eq. (3.41) by K_λ and using Eq. (3.42) yields

$$\frac{di'_\lambda}{K_\lambda dS} = -i'_\lambda(S) + (1-\Omega_{0\lambda})i'_{\lambda b}(S) + \frac{\Omega_{0\lambda}}{4\pi}\int_{\omega_i=4\pi} i'_\lambda(S,\omega_i)\Phi(\lambda,\omega,\omega_i)d\omega_i \quad (3-43)$$

The final two terms in (3-43) are combined into the source function $I'_\lambda(S,\omega)$ defined as

$$I'_\lambda(S,\omega) \equiv (1-\Omega_{0\lambda})i'_{\lambda b}(S) + \frac{\Omega_{0\lambda}}{4\pi}\int_{\omega_i=4\pi} i'_\lambda(S,\omega_i)\Phi(\lambda,\omega,\omega_i)d\omega_i \qquad (3-44)$$

This is the source of intensity along the optical path from both emission and incoming scattering. For anisotropic scattering the I'_λ is a function of ω (that is, the direction of S). The equation of transfer then becomes

$$\frac{di'_\lambda}{dS} + K_\lambda i'_\lambda(S) \equiv K_\lambda I'_\lambda(S,\omega) \qquad (3-45)$$

This is an integrodifferential equation since i'_λ is within the integral of the source function.

3.7 Integration by Use of Integrating Factor

Equation (3-45) is a first-order linear integrodifferential equation, and an integrated form can be obtained by use of an integrating factor. Multiplying through by $exp\left[\int_0^S K_\lambda dS\right]$ gives

$$exp\left[\int_0^S K_\lambda dS\right]\frac{di'_\lambda(S)}{dS} + exp\left[\int_0^S K_\lambda dS\right]K_\lambda i'_\lambda(S) = exp\left[\int_0^S K_\lambda dS\right]K_\lambda I'_\lambda(S,\omega) \qquad (3-46)$$

The first two terms can be combined together as

$$\frac{d}{dS}\left[i'_\lambda(S)exp\left[\int_0^S K_\lambda dS\right]\right] = exp\left[\int_0^S K_\lambda dS\right] K_\lambda I'_\lambda(S,\omega) \qquad (3-47)$$

Integrating over a distance from S=0 to S=S gives

$$i'_\lambda(S)exp\left[\int_0^S K_\lambda dS\right] i'_\lambda(0) = \int_0^S exp\left[\int_0^{S^*} K_\lambda dS^{**}\right] K_\lambda I'_\lambda(S^*,\omega)dS^* \quad (3-48)$$

Dividing through by $exp\left[\int_0^S K_\lambda dS\right]$ gives

$$i'_\lambda(S) = i'_\lambda(0)exp\left[\int_0^S K_\lambda dS\right] + exp\left[-\int_0^S K_\lambda dS\right]$$

$$\times \int_0^S exp\left[\int_0^S K_\lambda dS\right] K_\lambda I'_\lambda(S^*,\omega)dS^* \qquad (3-49)$$

where S^* and S^{**} are dummy variables of integration.

It has been found convenient by other authors (Siegel and Howell [29] and Love [30]) to use the non-dimensionalized equation of transfer (3-49) in terms of optical thickness, τ, and the albedo parameter. The optical depth or opacity when both scattering and absorption are present was defined in Eq. (3-6)

$$\tau_\lambda(S) = \int_0^S K_\lambda(S^*)dS^* = \int_0^S (a_\lambda + \sigma_{S\lambda})dS^* \qquad (3-50)$$

where S^* is a dummy variable of integration. Introducing (3-50) into (3-44), (3-45), and (3-49) gives the non-dimensionalized form of source function, equation of transfer, and the integrated form of equation of transfer respectively.

$$I'_\lambda(\tau_\lambda,\omega) \equiv (1-\Omega_{0\lambda})i'_{\lambda b}(\tau_\lambda) + \frac{\Omega_{0\lambda}}{4\pi}\int_{\omega_i} i'_\lambda(\tau_\lambda,\omega_i)\Phi(\lambda,\omega,\omega_i)d\omega_i \qquad (3-51)$$

$$\frac{di'_\lambda}{d\tau_\lambda} + i'_\lambda(\tau_\lambda) = I'_\lambda(\tau_\lambda,\omega) \qquad (3-52)$$

$$i'_\lambda(\tau) = i'_\lambda(0)exp(-\tau) + \int_0^{\tau_\lambda} I'_\lambda(\tau^*_\lambda)exp[-(\tau_\lambda - \tau^*_\lambda)]d\tau^*_\lambda \qquad (3-53)$$

where $d\tau_\lambda = K_\lambda(S)dS$ is the optical differential thickness.

Equation (3-53) is interpreted physically as the intensity being composed of two terms at optical depth τ_λ. The first term is the attenuated incident radiation arriving at τ_λ (including, however, the contribution of induced emission along the path). The second term is the intensity at τ_λ resulting from spontaneous emission and incoming scattering in the S direction by all elements along the path, reduced by exponential attenuation between each point of emission and incoming scattering τ^*_λ and the location τ_λ.

The equation (3-52) or (3-53) cannot be used itself to obtain the local intensity because it contains the unknown temperature and scattering distributions that are in the source function [the temperature is in the $i'_{\lambda b}(\lambda, T)$ within I'_λ]. Temperature distribution is also needed to determine the absorption and scattering coefficients so that the local optical depth $\tau_\lambda(S)$ can be computed from (3-50), and the physical coordinate S thereby related to the optical coordinate τ_λ. The temperature distribution depends on conservation of energy within the medium, which in turn depends on the total absorbed radiation in each volume element along the path. This total energy will be obtained by utilizing the intensity passing through a location and integrating over all incident solid angles and all wavelengths. The energy equation should be solved in conjunction with a source function equation to yield compatible temperature and scattering distributions. The source function equation is found by inserting (3-53) into (3-51) to eliminate i'_λ and obtain an equation for I'_λ. The resulting equations are sufficiently complex so that numerical solutions are almost always required.

CHAPTER IV

ANALYSIS

4.1 Statement of Problem

Due to the compact and complex propellant path configuration of the rocket engine,the leak plume shape and resulting temperature distribution will be difficult to predict. Significant plume impingement on other components will result in solid surface radiation as well as gas plume radiation. Since the leak flow field is extremely complex, a simple physical model of a leak plume was developed for evaluation analytically, numerically and experimentally.

The physical problem is illustrated schematically in Figure 4-1, which consists of a background plate, gas plume, and an infrared detector. The background plate, a continuous and uniform radiation source, is an opaque (non-transparent) surface. The radiant energy is taken to be diffusely incident upon a differential area of the gas medium which is chosen to be water vapor, a tri-atomic gas, which absorbs and emits significantly in the infrared wavelength range. This participating gas medium is non-gray and non-isothermal which can absorb, emit, and scatter the incident radiant energy.

The surrounding medium is considered to be air which is a non-participating medium with refractive index equal to unity. The infrared detector, a thermal imaging system, has a wavelength range of 2 to 5 μm. The lenses for the scanner of the IR detector are antireflective coated, therefore, all the incoming radiation energy is transmitted through the lenses without being reflected, in the specified range of wavelength.

The physical coordinate system is also described in Figure 4-1.

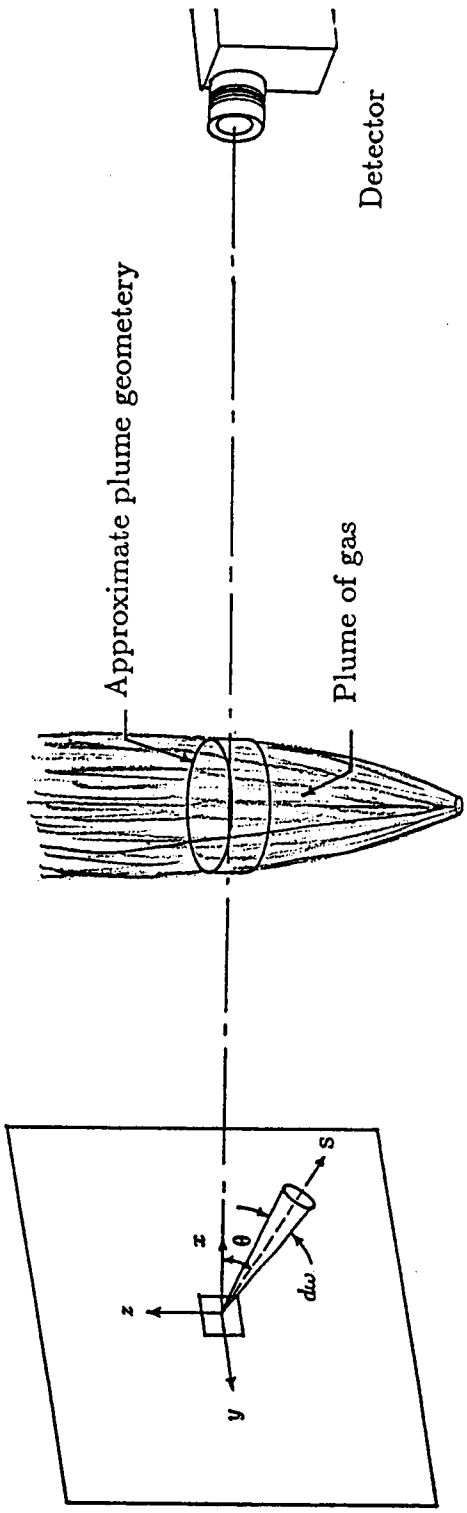


Figure 4.1 Schematic illustration of the problem

Regions 1, 2, and 3 represent the air, gas medium, and air respectively.

4.2 Basic Assumptions

The opaque background plate is a continuous and uniform source of radiation energy which is the base radiation for the present work. The plate is used as a known radiation source and considered to be isothermal. The temperature range used for numerical calculation is 300 ^{o} to 2700 ^{o} K, but for experimental investigation the upper limit was up to 800^oK because of limitation in available commercial source of radiation. The participating gas medium is assumed to be homogeneous, continuous and in local thermodynamic equilibrium.

The surrounding air is a non-attenuating and non-emitting medium with refractive index equal to unity and has constant properties. Since air occupies the distance between the radiation source and the plume, the directional intensity at the boundary of the medium is the same as the intensity of the background source.

The interior of the gas volume is taken to be an absorbing, emitting, and scattering medium. According to Ref. [30], scattering is defined as any change in the direction of propagation of the photons. The process is physically due to local inhomogeneities within the medium, and such inhomogeneities may result from suspended solid particles or liquid droplets within the gas. Examples of such situations include radiative heat transfer through dust, smoke, glass fiber insulation, plastics or ceramics that contain bubbles or pigment particles. In such media energy will be scattered as well as absorbed from a pencil of rays, resulting in a change of intensity along a given direction. In general we may, however, expect that only a part of the energy lost from an incident pencil of rays will reappear as scattered radiation in other directions and that the remaining part will be truly absorbed.

The scattering is assumed to be isotropic; thus, radiation is scattered uniformly in all directions. Based on Ref. [4], the justification for isotropic scattering can be categorized as: 1) For small optical spacing and small values of particle size parameter, the effect of anisotropic scattering is closely approximated by the isotropic case. 2) For infinite clouds of particles which may be composed of various size and shape of the particles with random orientation and unknown refractive indices, analytical determination of the scattering function may be impossible.

The assumption of single scattering is also imposed. Because the radiation transport equation is based on conservation or balance about a differential element, dS, single scattering implies that a beam of intensity incident on an infinitesimal element can undergo at most one scatter. This does not mean that a beam of intensity can not be scattered many times as it travels through the medium; it only means that scattering can occur only once in each differential element. In passing through many dS elements, the beam may be scattered many times.

The intensity field is assumed to be one-dimensional, therefore, dependent only on one spatial coordinate, namely the S or τ coordinate, and the radiative transport equation is based on conservation or balance on a differential element, dS. Steady State and local thermodynamic equilibrium is also assumed.

4.3 Equation of Transfer in x - Direction

The arbitrary path S in figure 4.1 is at an angle θ from the x direction. The optical depth $\tau_\lambda(x)$ is now defined along the x coordinate as

$$\tau_\lambda(x) = \int_0^x K_\lambda(x^*)dx^* \qquad (4-1)$$

The radiation between optical positions along S and x direction is given by

$$\tau_\lambda(S) = \int_0^S K_\lambda(S^*)dS^* = \int_0^{\frac{x}{cos\theta}} K_\lambda(\frac{x^*}{cos\theta})d(\frac{x^*}{cos\theta})$$

$$= \frac{1}{cos\theta}\int_0^x K_\lambda(x^*)dx^* = \frac{\tau_\lambda(x)}{cos\theta} \qquad (4-2)$$

Then, with $d\tau_\lambda(S) = \frac{d\tau_\lambda(x)}{cos\theta}$, the equation of transfer (3-53) becomes

$$cos\theta\frac{di'_\lambda}{d\tau_\lambda(x)} + i'_\lambda(\tau_\lambda(x),\theta) = I'_\lambda(\tau_\lambda(x),\theta) \qquad (4-3)$$

where I'_λ depends on θ because of the angular dependency of the phase function Φ on anisotropic scattering.

A convenient substitution is to let $\mu = cos\theta$; then (4-3) becomes

$$\mu\frac{di'_\lambda}{d\tau_\lambda(x)} + i'_\lambda(\tau_\lambda(x),\mu) = I'_\lambda(\tau_\lambda(x),\mu) \qquad (4-4)$$

Integrated form of eq.(4-4) is

$$i'_\lambda(\tau_\lambda,\mu) = i'_\lambda(0,\mu)exp(\frac{-\tau_\lambda}{\mu}) + \int_0^{\tau_\lambda} I'_\lambda(\tau^*_\lambda,\mu)exp\left[\frac{-(\tau_\lambda-\tau^*_\lambda)}{\mu}\right]\frac{d\tau^*_\lambda}{\mu} \qquad (4-5)$$

The range of θ is between 0 and $\frac{\pi}{2}$ so that μ changes from 0 to 1.

The transport equation (4-5) describes the spectral intensity field. This equation together with boundary conditions constitutes the basic mathematical problem to be solved for the description of the intensity field under the assumptions that have been previously stated.

4.4 Equation for Source Function

The source function $I'_\lambda(\tau_\lambda(x),\mu)$ which was defined in (3-51) can be written as

$$I'_\lambda(\tau_\lambda,\omega) \equiv (1-\Omega_{0\lambda})i'_{\lambda b}(\tau_\lambda) + \frac{\Omega_{0\lambda}}{4\pi}\int_{\omega_i} i'_\lambda(\tau_\lambda,\omega_i)\Phi(\lambda,\omega,\omega_i)d\omega_i \qquad (4-6)$$

For isotropic scattering the phase function Φ becomes equal to unity. The source function (4-6) reduces to

$$I'_\lambda(\tau_\lambda) \equiv (1-\Omega_{0\lambda})i'_{\lambda b}(\tau_\lambda) + \frac{\Omega_{0\lambda}}{4\pi}\int_{\omega} i'_\lambda(\tau_\lambda,\omega)d\omega \qquad (4-7)$$

where it is no longer necessary to use the subscript i on ω. The I'_λ is independent of ω in this instance.

The following derivation is done for directional intensity of a single element subtending a small solid angle $d\omega$. The solid angle $d\omega$ is equal to (see Figure 4.2)

$$d\omega = \frac{dA cos\theta}{S^2} \qquad (4-8)$$

where $dA = dydz$; for unit length in z direction, $dA = dy$. Substituting (4-8) into (4-7) yields

$$I'_\lambda(\tau_\lambda) \equiv (1-\Omega_{0\lambda})i'_{\lambda b}(\tau_\lambda) + \frac{\Omega_{0\lambda}}{4\pi}\int_{\Delta y} i'_\lambda(\tau_\lambda,\theta)\frac{cos\theta}{S^2}dy \qquad (4-9)$$

Directional spectral intensity $i'_\lambda(\tau_\lambda,\theta)$, cos$\theta$, and S are constant for small Δy, thus

$$I'_\lambda(\tau_\lambda) \equiv (1-\Omega_{0\lambda})i'_{\lambda b}(\tau_\lambda) + \frac{\Omega_{0\lambda}}{4\pi}\left[i'_\lambda(\tau_\lambda,\theta)\frac{cos\theta}{S^2}\Delta y\right] \qquad (4-10)$$

Inserting Eq.(4-5) into Eq.(4-10) to eliminate i'_λ and obtain an equation for I'_λ, for an element of area, $dA = dy$

$$I'_\lambda(\tau_\lambda) \equiv (1-\Omega_{0\lambda})i'_{\lambda b}(\tau_\lambda)$$

$$+\frac{\Omega_{0\lambda}\mu\Delta y}{4\pi S^2}\left[i'_\lambda(0,\mu)exp(\frac{-\tau_\lambda}{\mu}) + \int_0^{\tau_\lambda} I'_\lambda(\tau^*_\lambda,\mu)exp[\frac{-(\tau_\lambda-\tau^*_\lambda)}{\mu}]\frac{d\tau^*_\lambda}{\mu}\right] \qquad (4-11)$$

This equation is sufficiently complex so that numerical solution is required.

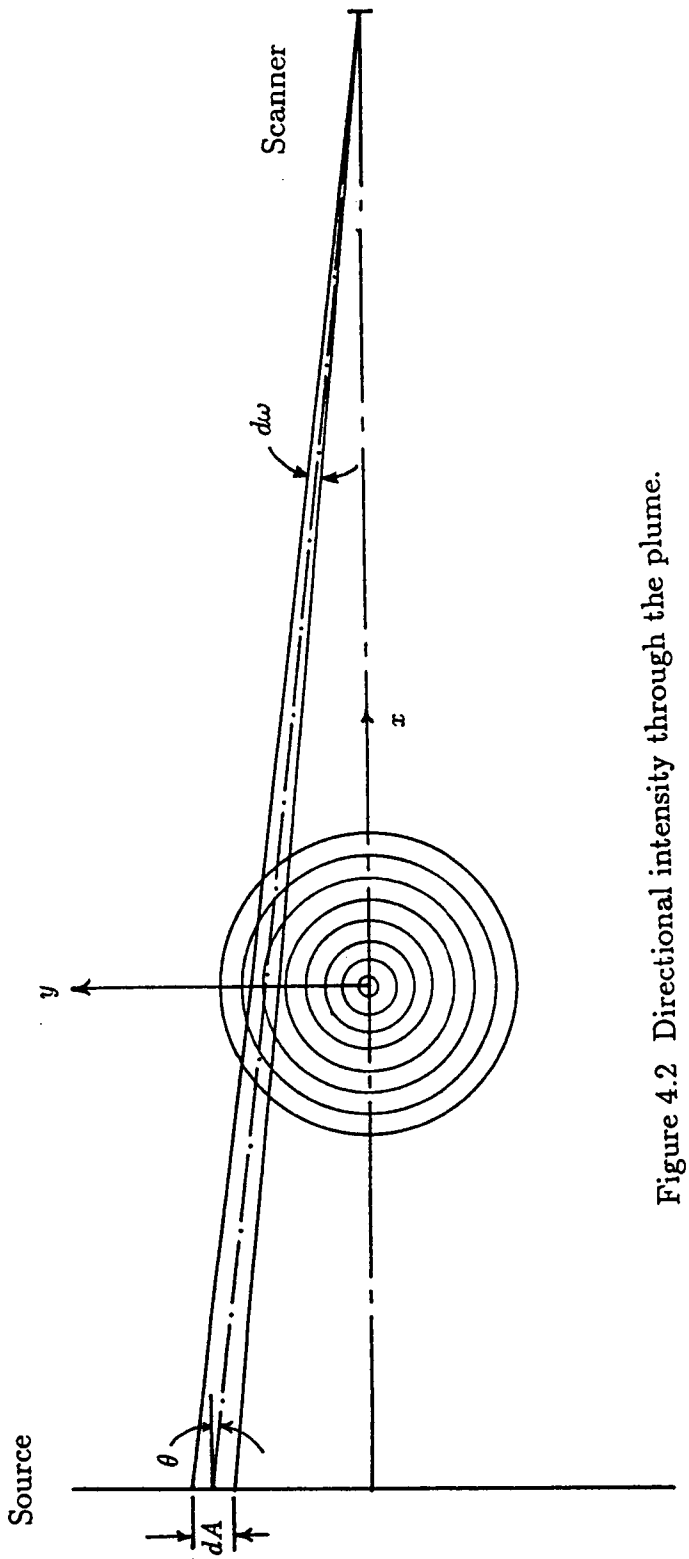


Figure 4.2 Directional intensity through the plume.

4.5 Boundary Conditions

The boundary value of the intensity i'_λ has to be specified in order to select a unique solution from the family of solutions to the integrodifferential equation (3-52). Generally the boundary could be walls, adjacent layers of the medium or vacuum. The boundary value of the intensity i'_λ may consist of radiation emitted by the boundary and radiation coming from an outer source and entering the region through the boundary.

For the one-dimensional case treated here, it is easy to choose the reference direction for θ. For plume geometries, the integrated directional intensity across the plume is

$$i'(S) = \int_2^5 i'_\lambda(S) d\lambda \qquad (4-12)$$

In the search for a realistic numerical model several combinations of boundary conditions were considered for the background radiation source and the participating media of gas plume. The two sets of boundary conditions employed were:

1. Blackbody radiation source with absorbing and emitting media.
2. Blackbody radiation source with absorbing, emitting and scattering media.

4.6 Blackbody Radiation Source with Absorbing and Emitting Media

The black surfaces emit in a perfectly diffuse fashion, such that the radiation intensity leaving a surface is independent of the direction of emission. For zero scattering $\Omega_{0\lambda} \to 0$, reducing the source function, Eq.(4-11) to

$$I'_\lambda = i'_{\lambda b}(T_g) \qquad (4-13)$$

The spectral intensity of the blackbody can simply be calculated by the Planck's law,

$$i'_{\lambda b}(\lambda) = \frac{2C_1}{\lambda^5}\left[exp(\frac{C_2}{\lambda T}) - 1\right]^{-1} \qquad (4-14)$$

The constants are defined as $C_1 = hc_0^2$ and $C_2 = hc_0/k$, where h is Planck's constant and k is the Boltzmann constant.

When distance between the plate and detector is large, compared with the plate actual size, the angle θ is very small, thus, μ approaches one. The intensity entering the participating media will be the same as blackbody intensity evaluated at T_p

$$i'_{\lambda}(0) = i'_{\lambda b}(T_g) \qquad (4-15)$$

.

4.7 Blackbody Radiation Source With Absorbing, Emitting and Scattering Media

The source function for this case has been derived in section 4.4 which has the final form of

$$I'_{\lambda}(\tau_\lambda) \equiv (1-\Omega_{0\lambda})i'_{\lambda b}(\tau_\lambda)$$
$$+\frac{\Omega_{0\lambda}\mu\Delta y}{4\pi S^2}\left[i'_{\lambda}(0,\mu)exp(\frac{-\tau_\lambda}{\mu}) + \int_0^{\tau_\lambda} I'_{\lambda}(\tau^*_\lambda,\mu)exp[\frac{-(\tau_\lambda-\tau^*_\lambda)}{\mu}]\frac{d\tau^*_\lambda}{\mu}\right] \qquad (4-11)$$

The entering intensity into the plume has the same form of Eq.(4-15).

CHAPTER V

NUMERICAL MODELING

Numerical results are very important since they are basis for confirming or disqualifying any attempt at an experimental program. The useful information from numerical results provides excellent guidance to select the best wavelength range for infrared detector, filters and equipment set up for generation of better experimental data. From observation of the numerical data and evaluation of the available information one can make a more realistic experimental model.

The numerical radiation transport model is developed for a simple geometry containing a background radiation source, a simulated leak plume model in the form of cylindrical shape and a sensor location. Water vapor H_2O was selected as the molecule for evaluation of emission and absorption. The high absorption of water vapor in the infrared wavelength region may be exploited for plume detection. The models developed cover a temperature range of 300 ^{o} to 2700 ^{o}K at atmospheric pressure and wavelengths of 2 to 5 μm.

The numerical solution of the radiation transport equation (4-5) gives the local spectral intensity in the medium. In this chapter consideration is given to the development of numerical solutions of the equation of transfer, (4-5). The attention is limited to a plane source of radiation, incident on a cylindrical plume of pure water vapor as a medium of absorbing, emitting, and scattering.

5.1 Numerical Form of The Equation of Transfer

The theoretical development of the equation of transfer has been derived in chapter 3, but the numerical form of the equation will be presented here. For simplicity the prime which denoted radiation per unit solid angle in a single direction has

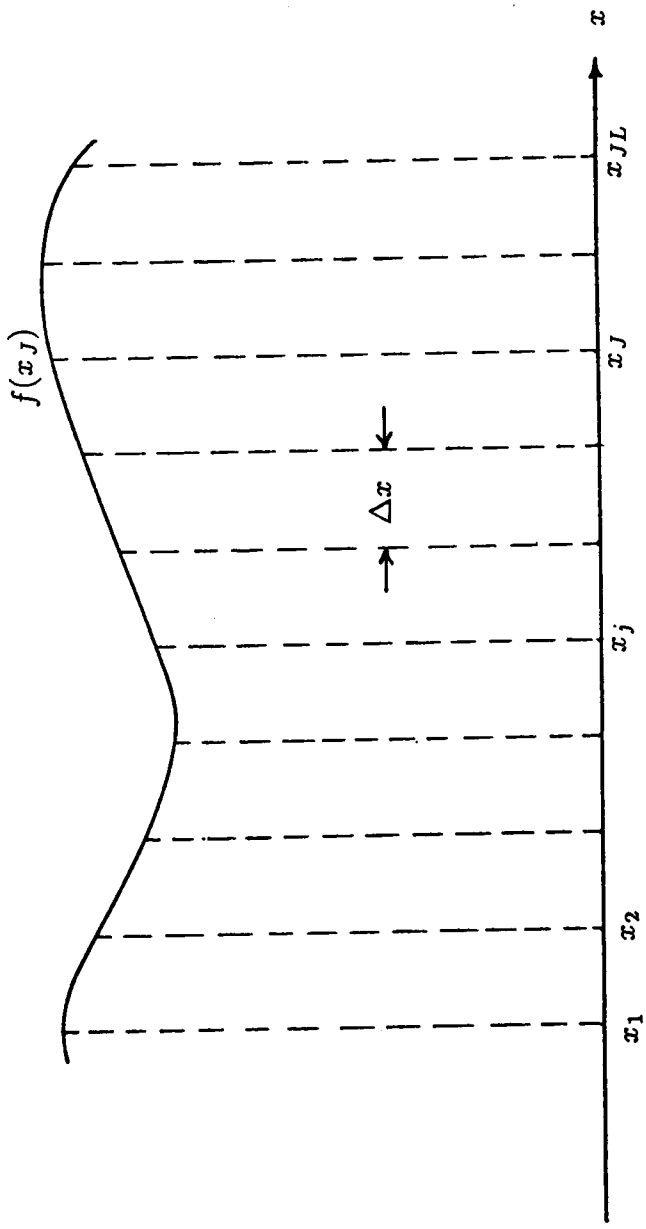


Figure 5.1 Equally spaced abscissas for numerical computation.

been eliminated. But keep in mind that the calculation will be done based on a single direction.

The optical thickness, equation (4-1), can be expressed by standard numerical integration techniques. It is also the basic formulation for evaluation of the integral terms in equations (4-5) and (4-11). One numerical approach among many, is the Trapezoidal rule, which is one of the most used formula to evaluate an integral.

Figure 5.1 shows the equally spaced abscissas for computation of the integral terms. Using this technique, equation (4-1) becomes

$$\tau(x_{i,j=J}) = \sum_{j=1}^{J} \beta_j K(x_{i,j}) \qquad (5-1)$$

where

$\beta_j = \frac{1}{2}\Delta x$, for $j = 1$ and $j = J$,

$\beta_j = \Delta x$, for $j \neq 1$ and $j \neq J$,

$j = 1, 2, ..., J, ..., JL.$

and

JL is the number of stations employed in marching from 0 to x and Δx is the step size, x / JL-1.

Similarly, the integral term in equation (4-5) can be expressed as

$$\int_0^{\tau_\lambda} I_\lambda(\tau_\lambda^*, \mu) exp\left[\frac{-[\tau_\lambda(x) - \tau_\lambda(x^*)]}{\mu}\right] \frac{K_\lambda(x^*)dx^*}{\mu} =$$

$$\sum_{j=1}^{J} \beta_j I(x_{i,j}) exp\left[\frac{-[\tau(x_{i,J}) - \tau(x_{i,j})]}{\mu}\right] \frac{K(x_{i,j})}{\mu} \qquad (5-2)$$

Substituting (5-1) and (5-2) into (4-5) yields

$$i(x_{i,J}) = i(x_{i,1}) exp\left[\frac{-\tau(x_{i,JL})}{\mu}\right] +$$

$$\sum_{j=1}^{J} \beta_j I(x_{i,J}) exp\left[\frac{-[\tau(x_{i,J}) - \tau(x_{i,j})]}{\mu}\right] \frac{K_{i,j}}{\mu} \qquad (5-3)$$

The source function, I, in equation (5-3) with the help of equation (4-11) can be written as

$$I(x_{i,j}) = (1-\Omega_i) i_{b_{i,J}} + \frac{\Omega_i \mu \Delta y}{4\pi S^2} \left\{ i(x_{i,1}) \exp\left[\frac{-\tau(x_{i,J})}{\mu}\right] + \sum_{j=1}^{J} I(x_{i,j}) exp\left[\frac{-[\tau(x_{i,J}) - \tau(x_{i,j})]}{\mu}\right] \frac{K_{i,j}}{\mu} \right\} \quad (5-4)$$

The source function, equation (5-4), will be evaluated for all values of λ (denoted by subscribe i) and all sequence of abscissas $x_{i,1}, ..., x_{i,J}, ..., x_{i,JL}$, which are spaced apart by a constant step Δx. After all values of $I(x_{i,j})$ are evaluated, the values of out going intensity from the plume can be calculated.

The integral term of the intensity leaving the plume boundary can be evaluated by using the standard Simpson's rule. The resultant equation is similar to equation (5-3) with two differences. First, the equation will be evaluated at the outer boundary of the plume (j=JL). Second, the integral term will be evaluated by using Simpson's rule rather than the Trapezoidal rule. The equation now can be expressed as

$$i(x_{i,JL}) = i(x_{i,1}) exp\left[\frac{-\tau(x_{i,JL})}{\mu}\right] + \sum_{j=1}^{JL} \gamma_j I(x_{i,j}) exp\left[\frac{-(\tau(x_{i,JL} - \tau(x_{i,j}))}{\mu}\right] \frac{K_{i,j}}{\mu} \quad (5-5)$$

where

$\gamma_j = \Delta x$, for $j = 1$ and $j = J$,

$\gamma_j = 2\Delta x$, for $j \neq 1$ and $j \neq J$, J odd,

and $\gamma_j = 4\Delta x$, for $j \neq 1$ and $j \neq J$, J even.

5.2 Absorption Coefficient Data to be Used

The absorption a_λ and scattering coefficient $\sigma_{S\lambda}$ are required for calculation of radiation heat transfer in a participating medium. The absorption of radiation by the gas depend on the radiative properties of the gas medium. Analytical determination of the absorption coefficient requires quantum-mechanical calculations. Penner [1] presented a detail analytical study of quantum-mechanics effect on a_λ. The absorption coefficient is also needed to determine the scattering coefficient and to compute the local optical thickness $\tau_\lambda(S)$.

The absorption coefficients of the water vapor for the present work have been taken from ref. [2]. These average absorption coefficients were obtained by fitting an equation, obtained from statistical theory methods, to experimental data. The plots of average absorption coefficients versus wavenumbers at various temperatures are shown in figures 5.2a-g.

The tabulated form of absorption coefficient is required for numerical solution of the radiation transport equation to evaluate the directional spectral intensity passing through the plume. In order to tabulate the values of absorption coefficient, a simple straight line approximation techniques has been used to convert these plots to numerical data. In this technique, several points along the curve have been chosen. Each two neighbor points have been connected by a straight line.

Figure (5.3) represents the straight line technique. The following procedure has been performed in order to find an equation for absorption coefficients in a small portion of the line. Two points, a and b, on the curve is connected with a

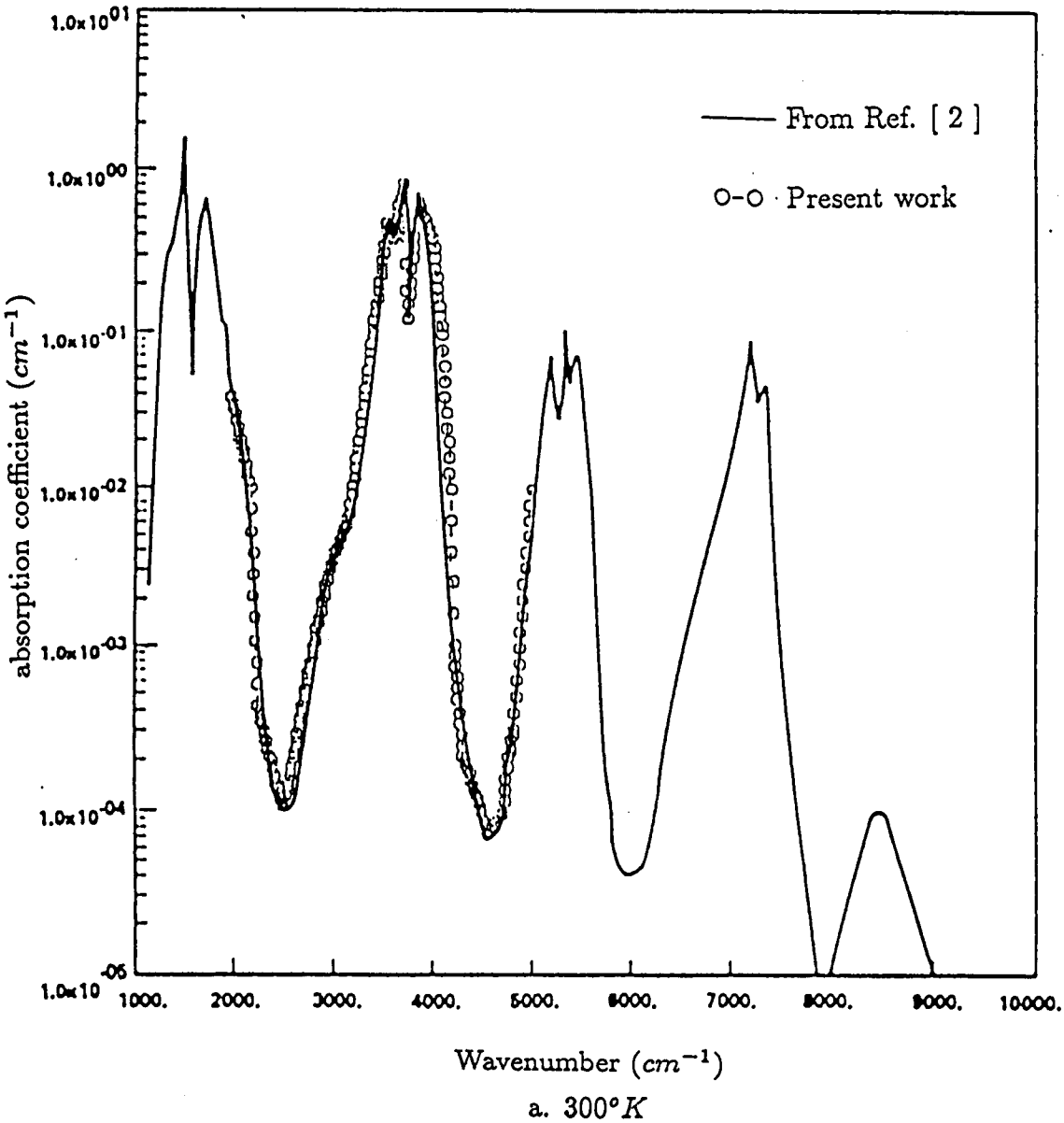
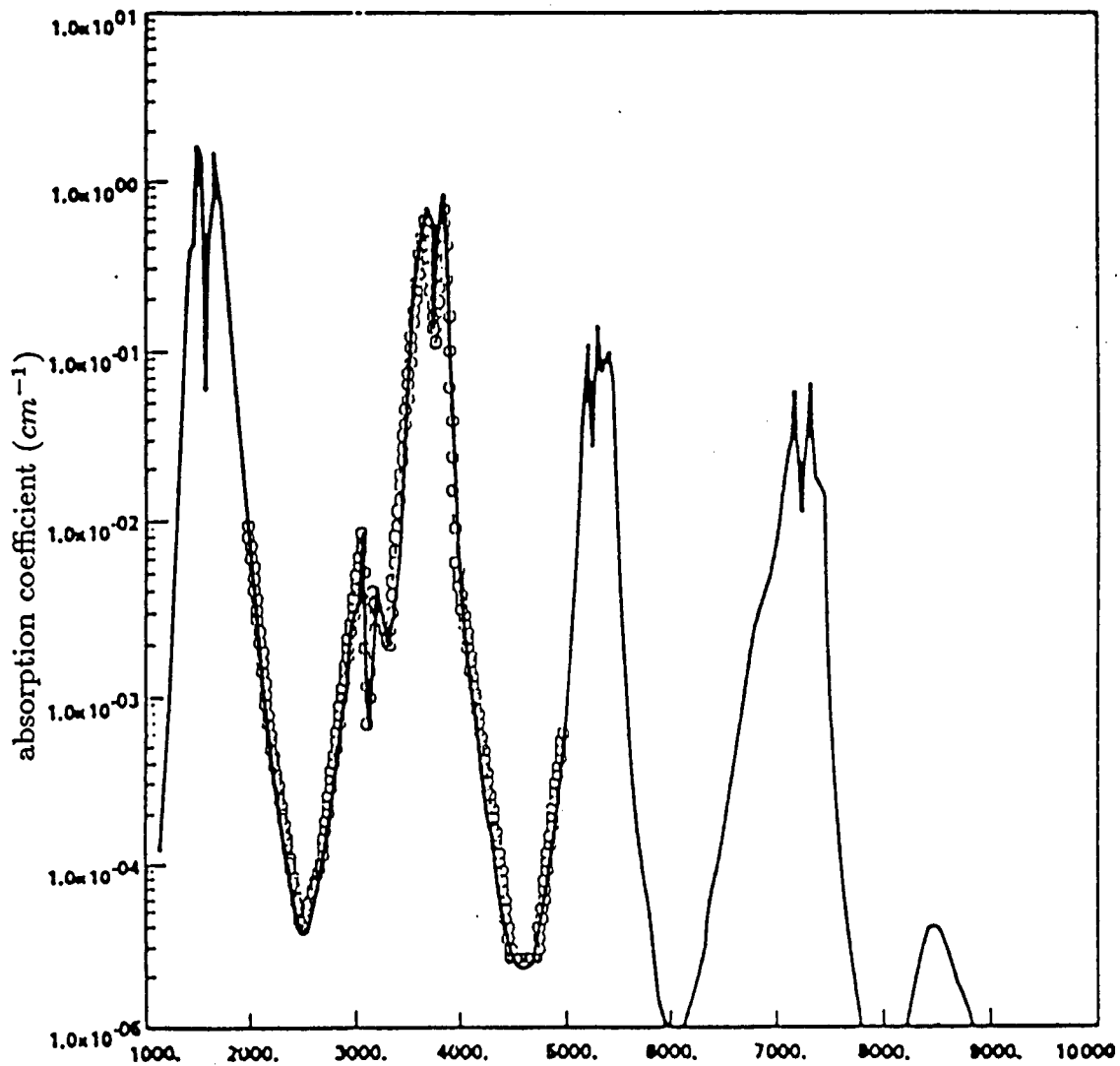
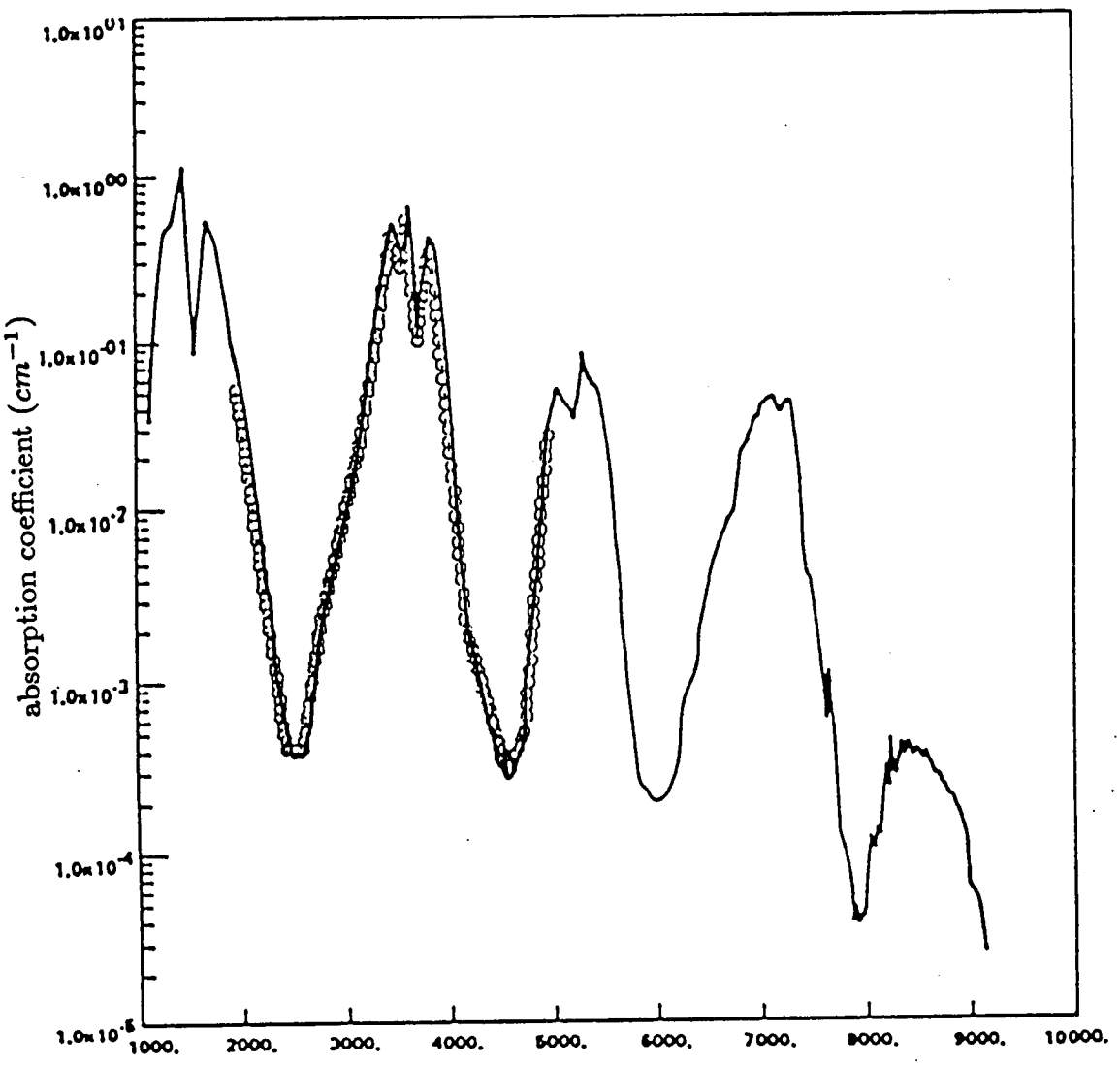


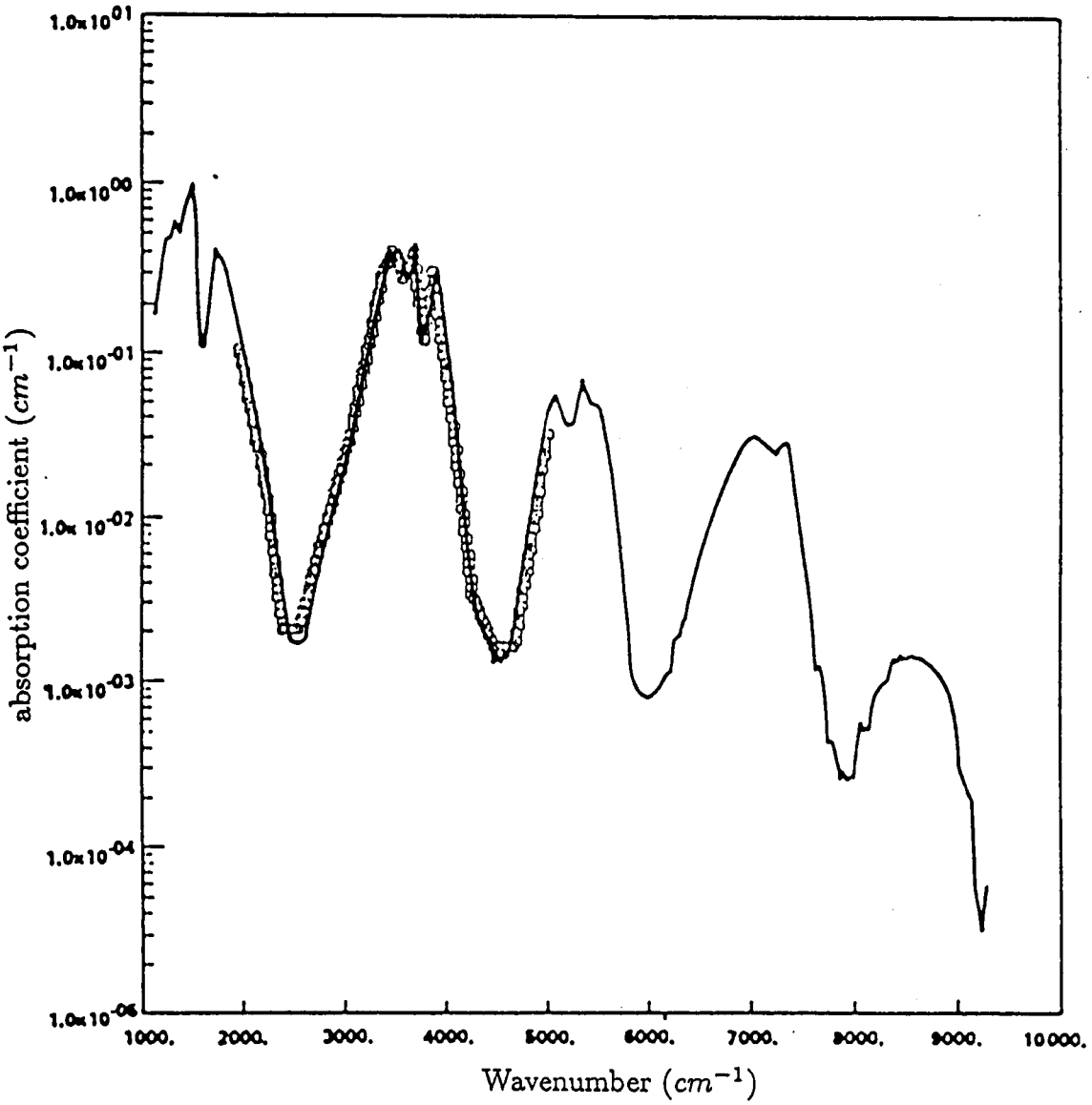
Figure 5.2 Mean absorption coefficient for water vapor at various temperatures.


1.0x10^01
1.0x10^00
1.0x10^-01
1.0x10^-02
1.0x10^-03
1.0x10^-04
1.0x10^-05
absorption coefficient (cm^{-1})
1000.
2000.
3000.
4000.
5000.
6000.
7000.
8000.
9000.
10000
Wavenumber (cm^{-1})

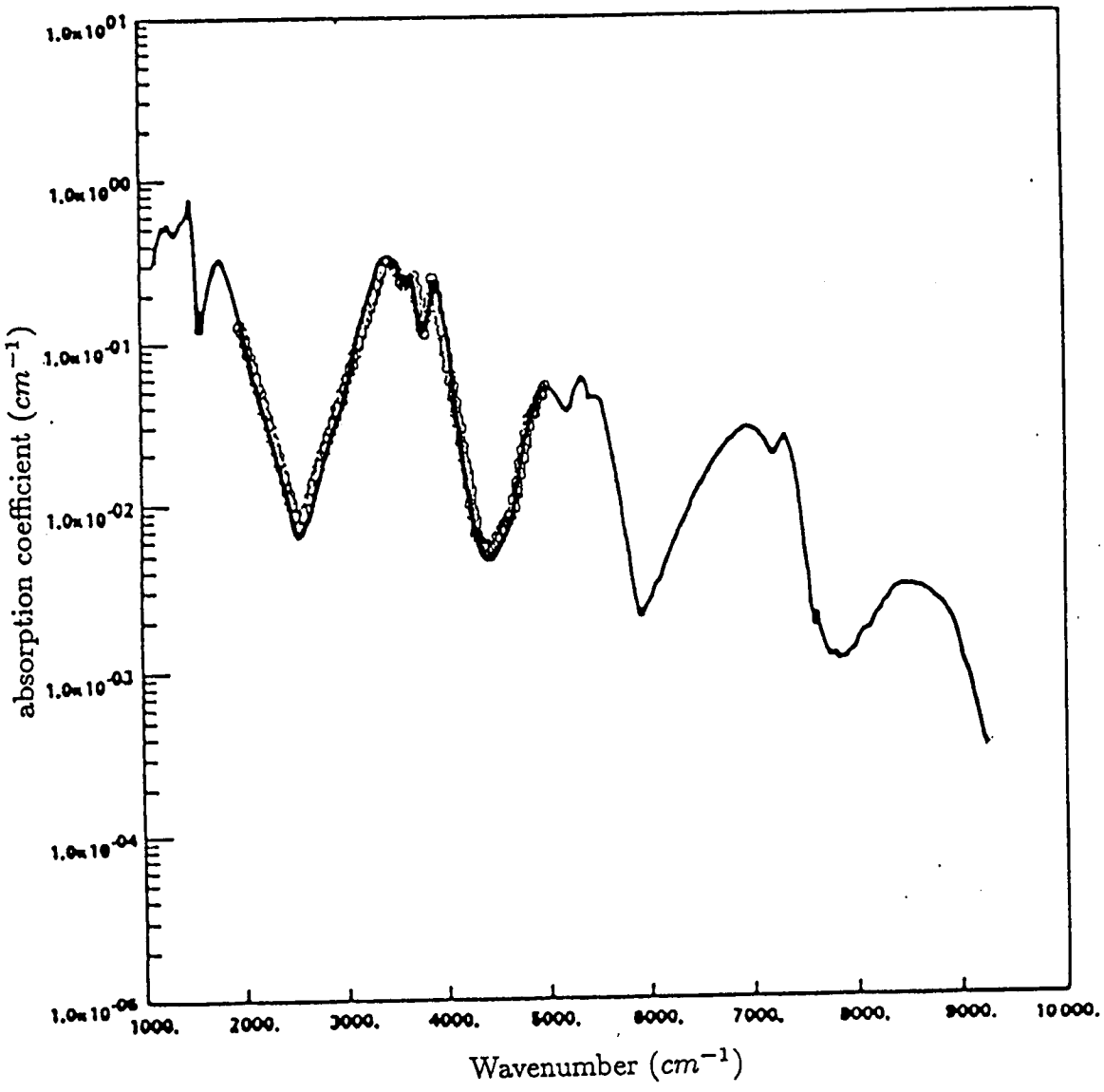
b. $600°K$


1.0x10^01
1.0x10^00
1.0x10^-01
1.0x10^-2
1.0x10^-3
1.0x10^-4
1.0x10^-5
absorption coefficient (cm^-1)
1000.
2000.
3000.
4000.
5000.
6000.
7000.
8000.
9000.
10000.
Wavenumber (cm^-1)

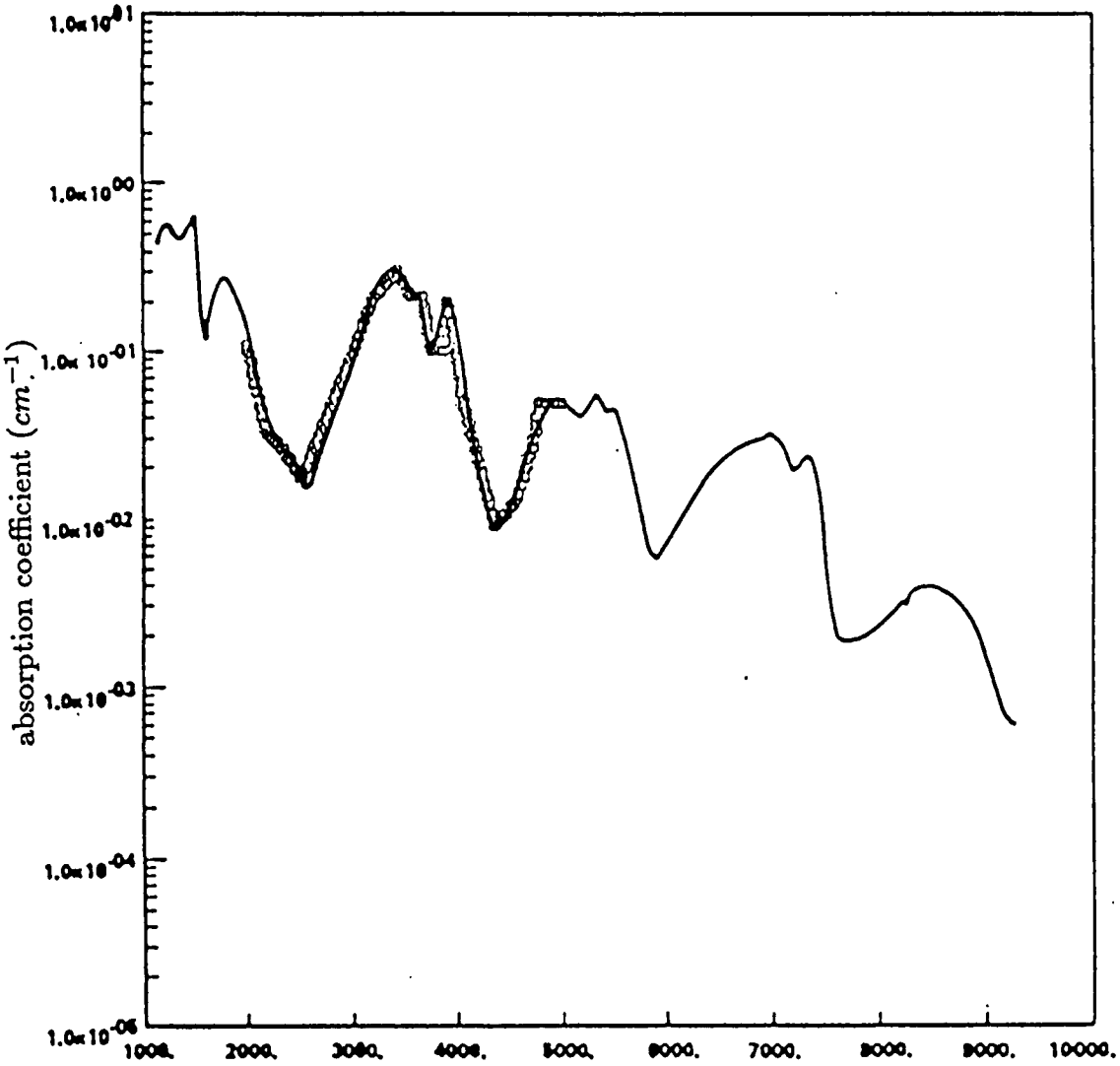
c. $1000^{o}K$


1.0x10^01
1.0x10^00
1.0x10^-01
1.0x 10^-02
1.0x10^-03
1.0x10^-04
1.0x10^-05
absorption coefficient (cm^{-1})
1000.
2000.
3000.
4000.
5000.
6000.
7000.
8000.
9000.
10000.
Wavenumber (cm^{-1})

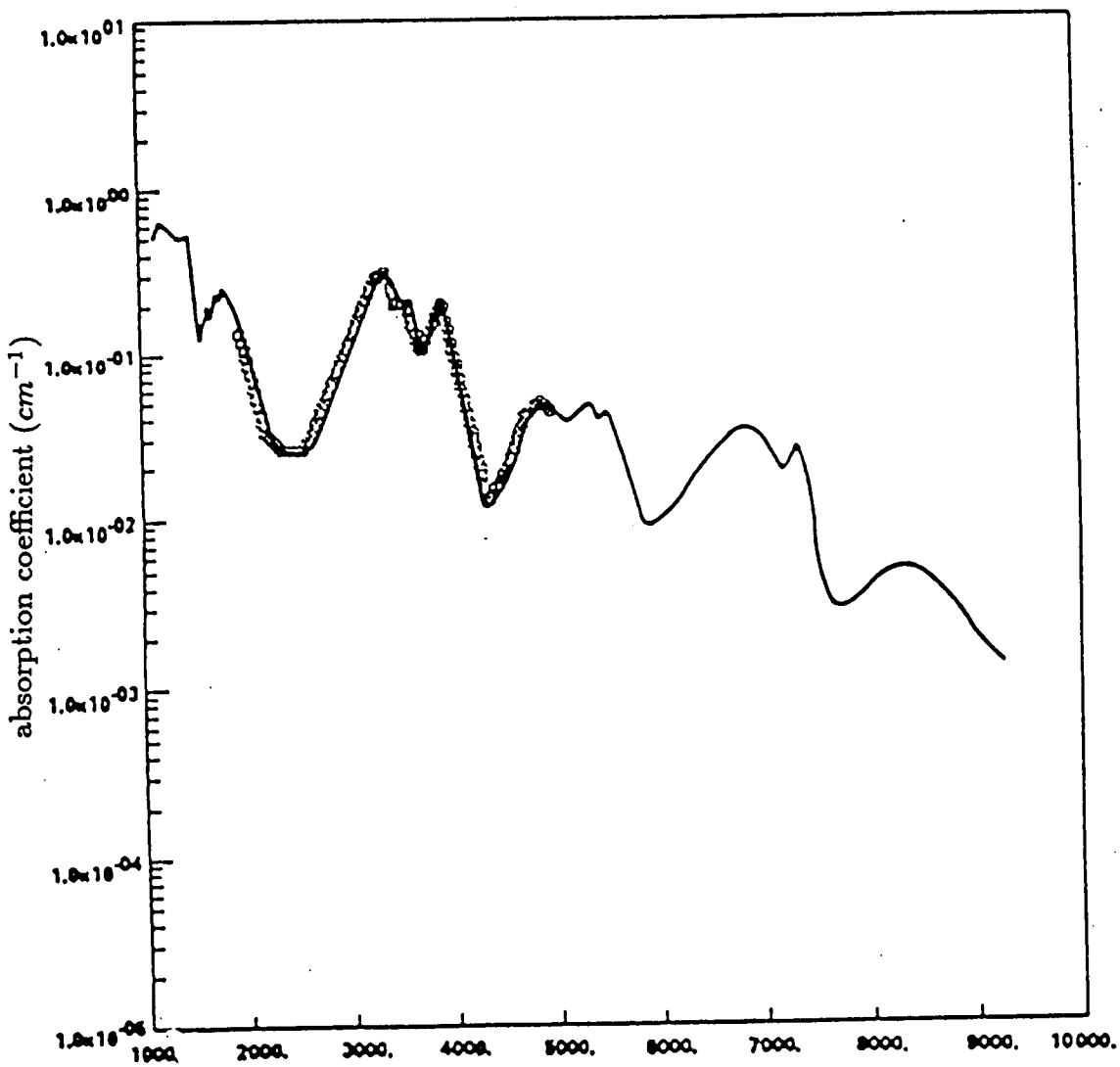
d. 1500°K


1.0x10^01
1.0x10^00
1.0x10^-01
1.0x10^-02
1.0x10^-03
1.0x10^-04
1.0x10^-05
absorption coefficient (cm^{-1})
1000.
2000.
3000.
4000.
5000.
6000.
7000.
8000.
9000.
10 000.
Wavenumber (cm^{-1})

e. $2000^{o}K$


absorption coefficient (cm^{-1})
1.0x10^01
1.0x10^00
1.0x 10^-01
1.0x10^-02
1.0x10^-03
1.0x10^-04
1.0x10^-05
1000.
2000.
3000.
4000.
5000.
6000.
7000.
8000.
9000.
10000.
Wavenumber (cm^{-1})

f. 2500°K


absorption coefficient (cm^{-1})
1.0x10^01
1.0x10^00
1.0x10^-01
1.0x10^-02
1.0x10^-03
1.0x10^-04
1.0x10^-05
1000.
2000.
3000.
4000.
5000.
6000.
7000.
8000.
9000.
10000.
Wavenumber (cm^{-1})

g. $2700°K$

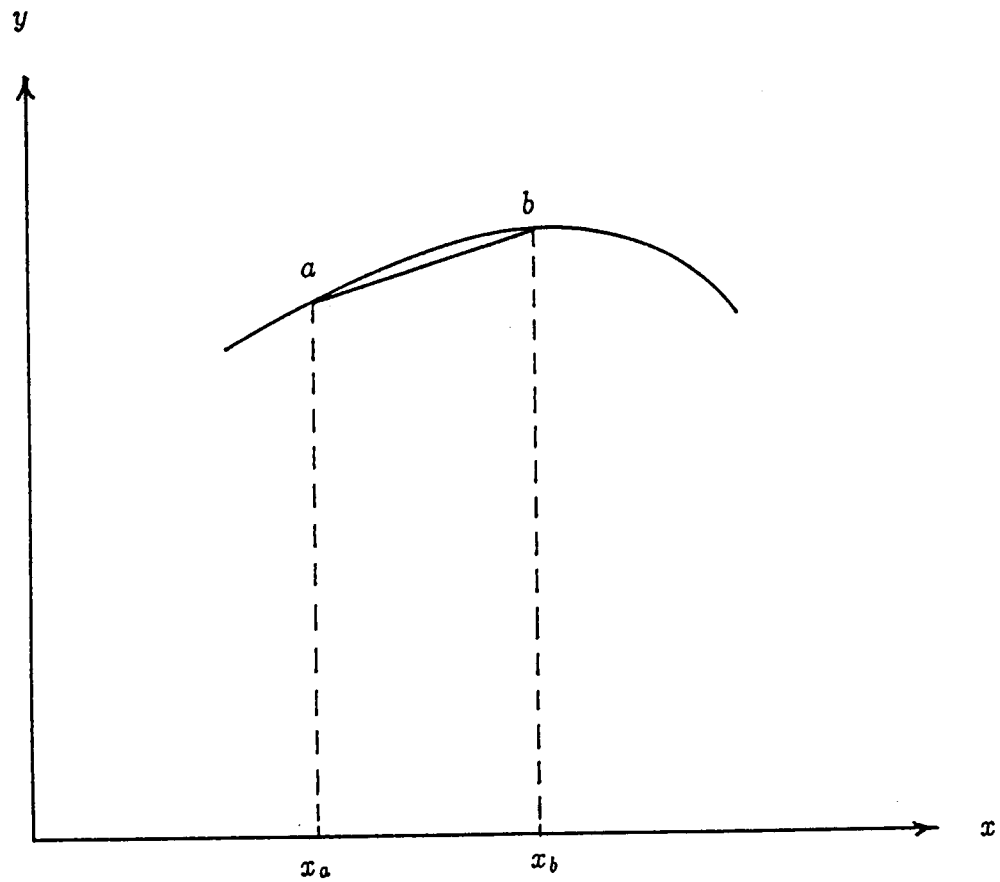


Figure 5.3 Straight line technique for numerical calculation of absorption coefficient.

straight line, then the coordinate values of a and b are read. The equation of the line is evaluated, thus at any point between a and b the absorption coefficients are calculated from this equation. The comparison results from this techniques with the actual curves are shown in figures 5.2a-g.

5.3 Temperature Distribution

Evaluation of local spectral intensity requires the temperature distribution in the medium to be known. The temperature distribution is also needed to determine the absorption coefficients so that the optical depth $\tau_\lambda(x)$ can be computed.

The temperature distributions for the non-isothermal participating gas media have been assumed to have the form of a Gaussian distribution radially across the plume. For the hot gas plume, the temperature profile has its maximum value at the center of the plume and minimum at the edge of the plume. For the cold gas the temperature profile has its minimum value at the center of the plume and maximum at the edge of the plume. Figure 5.4 represents the Gaussian temperature distribution for the hot water vapor plume.

The shape of the plume has been assumed to be cylindrical, thus the equation for temperature profile varies with the radius, r, of the plume cross section. The equation for the Gaussian temperature profile is

$$T(r) = T_{max} exp\left[(\frac{r}{R})^2 ln(\frac{T_{min}}{T_{max}})\right] \qquad (5-6)$$

With the above equation, the absorption and scattering coefficients at each point in the medium can be evaluated, which will be used in calculating the local spectral intensity.

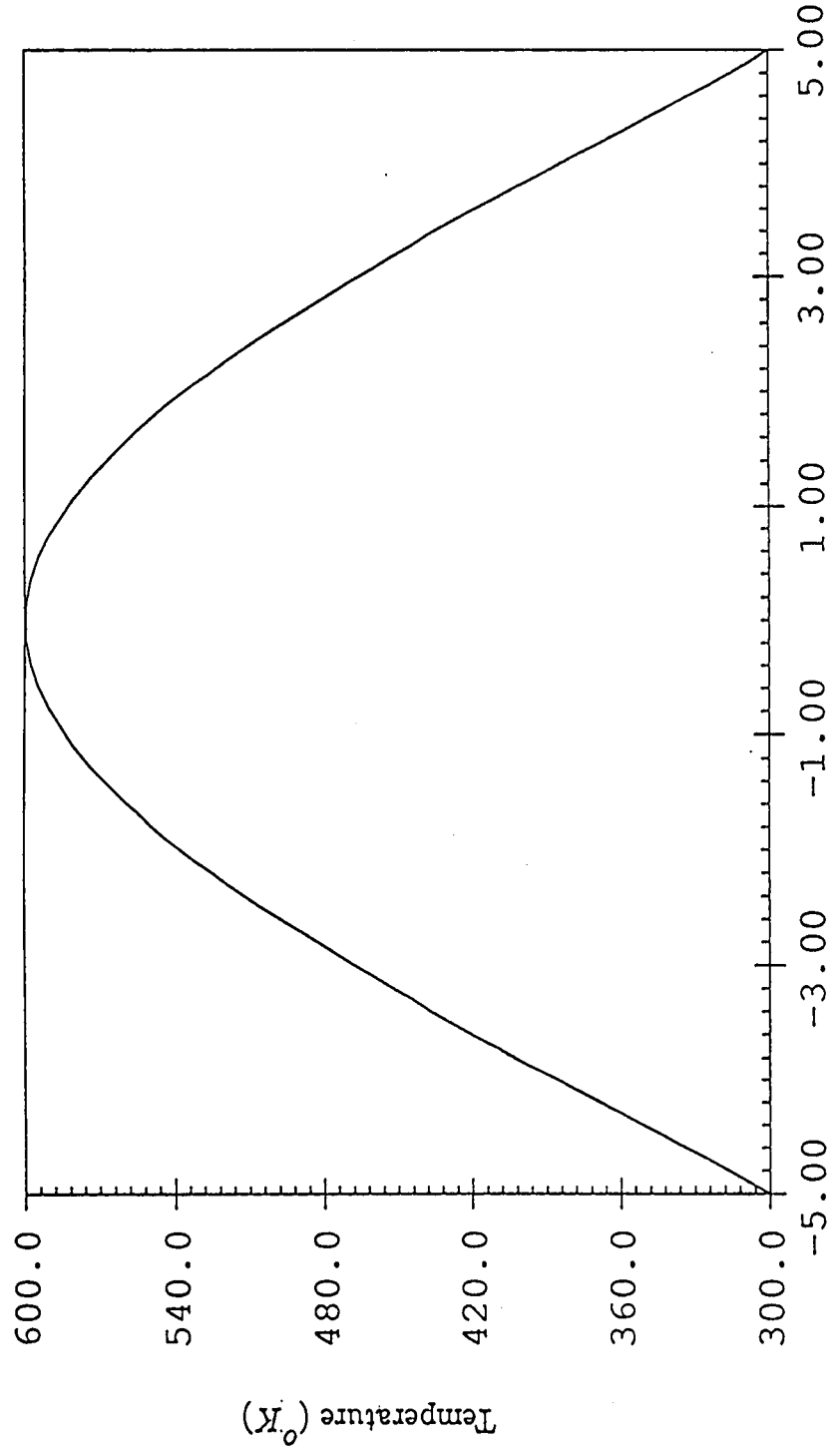


Figure 5.4 The Gaussian temperature distribution across the plume.

5.4 Numerical Procedure

The computer program for solving the directional intensity arriving at the detector will now be discussed. The following procedure has been adopted to find the reduction or amplification of the intensity passing through the participating media. This program generates the required input data and evaluates the intensity based on the mathematical model described in section 5.1. A flowchart of the main program is shown in figure (5.5). As shown in the flowchart, the main program first calls subroutine ABSCOF to compute the absorption coefficient and then reads the input data such as temperatures of the plate, plume centerline (T_{max}), and plume edges (T_{min}) and the plume size of under investigation. The calculation of directional intensity is evaluated at each Y location and at each single wavelength. Marching through the plume at a single direction, the main program calls subroutines TEMP and INTPOL to compute the optical thickness and the blackbody intensity. The main program then calls several other subroutines to evaluate the directional intensity at a single wavelength. The directional intensity for all other wavelengths will be evaluated by repeating the above processes. The above processes are done for evaluation of the directional intensity of a single element subtending a small solid angle. Finally, repetition of the above processes will give the directional intensity for the rest of the elements on the radiation source.

The detailed description of each subroutine used in the main program are given in following sections.

5.4.1 Subroutine ABSCOF

This subroutine evaluates the curve fit value of the absorption coefficient at

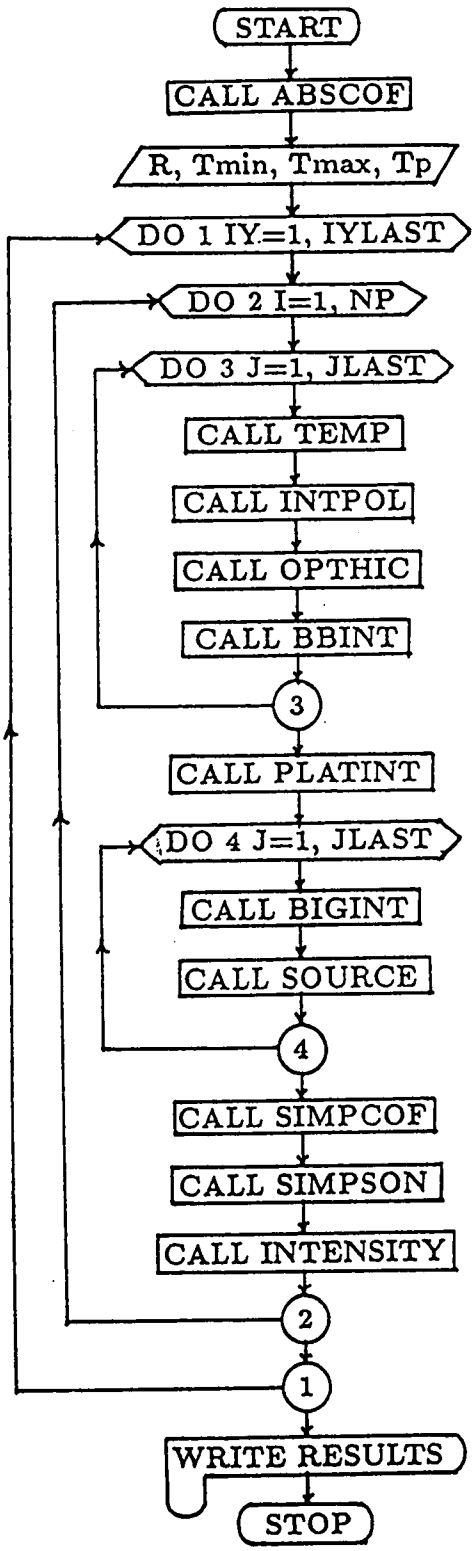


Figure 5.5 Flowchart of the Main program.

temperatures 300, 600, 1000, 1500, 2000, 2500, and 2700 ^oK. In order to determine these data, first it reads in the input values from seven input files. Each file represents a set of data at a certain temperature. Each set of data contains the coordinates of all the selected points on a particular curve. The slope of each segment of the curve which is represented by a straight line is evaluated, then the equation of that line is obtained. When all the equations of these lines are obtained, the values of absorption coefficients as a function of wavelength can be determined. The computed values of absorption coefficients are tabulated seperately for each set of temperatures mentioned above. These data are called to subroutine INTPOL to evaluate the scattering and extiction coefficients.

5.4.2 Subroutine TEMP

This subroutine computes the local temperature in the plume. The Gaussian temperature distribution, equation (5-5), provides these data. This equation indicates that the temperature is a function of radius, but has a constant value at a fixed radius. Figure (5.6) shows the plots of temperature for several different values of radius, also it indicates that when r increases, the value of temperature decreases.

5.4.3 Subroutine INTPOL

At each value of ΔS, the radius of that point is calculated prior to finding the temperature of that point. After the temperature is calculated, it is necessary to find the exact value of absorption and scattering coefficients. When the exact values of the absorption and scattering coefficients are not known at this temperature, an interpolation technique is used to find these coefficients. These interpolations are done between the existing data points which have been calculated in section 5.4.1.

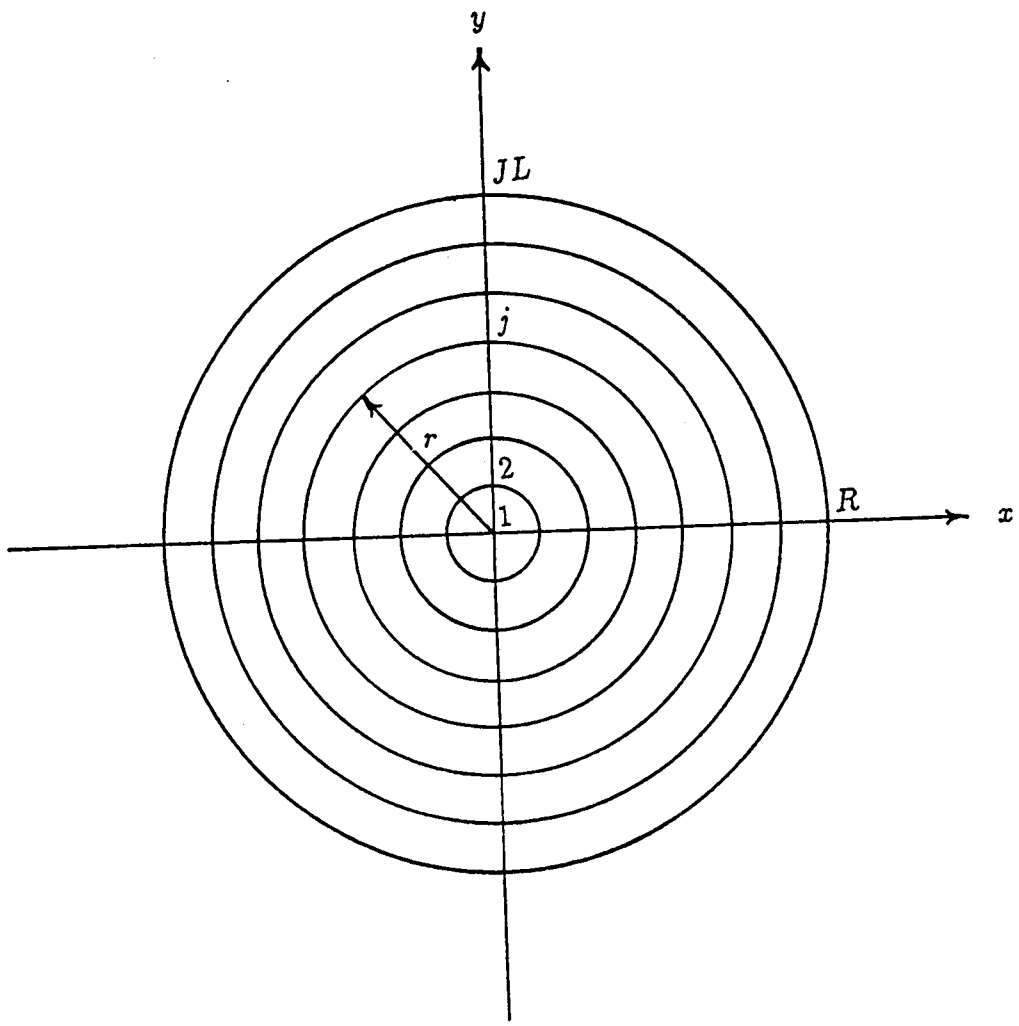


Figure 5.6 Temperature distribution across the hot plume at different radii ($T_1 = T_{max}$ *and* $T_{JL} = T_{min}$)

5.4.4 Subroutine OPTHIC

At each ΔS interval, the values of optical thickness are needed. This subroutine evaluates the local optical thickness. The extinction coefficient at each λ is given as input data and optical thickness is calculated. The integral term in equation (4-1) is evaluated using the Trapezoidal rule.

5.4.5 Subroutine BBINT

The intensity of blackbody radiance, $i_{b_{i,j}}$, is calculated in this subroutine. The temperature and λ are the input data for this subroutine. The spectral intensity of the blackbody is calculated by the Planck's law, equation (4-14). The calculated values from this subroutine will be used in the evaluation of the source function equation (5-4).

5.4.6 Subroutine SIMPCOF

To evaluate the summation term in equation (5-5), it is required to have the values of the constant multiplying coefficient γ_j. These coeffiecients are defined in equation (5-5). These constants are generated in this subroutine.

5.4.7 Subroutine PLATINT

Intensity entering the plume boundary , $i(x_{i,1})$, is calculated by this subroutine. By knowing the plate temperature and using equation (4-15) or (4-23), the intensity to the plume boundary is evaluated at each λ. This is equivalent to the intensity coming from the flat plate radiation source.

5.4.8 Subroutine SIMPSON

The summation term of the intensity leaving the plume boundary, equation (5-5), is computed in this subroutine. Simpson's rule is used to compute this summation term.

5.4.9 Subroutine BIGINT

This subroutine evaluates the summation term in the equation of source function equation (5-4). The calculated results from this summation term is used for evaluation of the source function.

5.4.10 Subroutine SOURCE

The values of source function are computed in this subroutine. This subroutine uses the output values from several different subroutines to evaluate the source function at every λ within the plume.

CHAPTER VI

DISCUSSION OF NUMERICAL RESULTS

The numerical radiation transport model was developed in chapter V. In this chapter consideration is given to numerical solution of the equation of transfer. Attention is limited to a plane source of radiation, incident on a cylindrical plume shape of water vapor as the absorbing, emitting, and scattering medium . The numerical models developed cover a temperature range of 300 to $2700^{o}K$ at atmospheric pressure and wavelengths of 2 to 5 μm.

6.1 Blackbody Radiation Source with Absorbing and Emitting Media

The physical description of this case has been presented in chapter IV. Now the numerical results will be discussed in light of the theoretical structure of the model. The boundary conditions for this case are given by equations (4-20) and (4-22). The schematic used in the radiation transport model for a simulated leak plume with a cylindrical geometry is shown in Figure 6.1. The plume cross section for numerical calculation of directional intensity is shown in Figure 6.2. This figure defined the nomenclature used in this chapter.

Figures 6.3 and 6.4 are typical numerical results calculated for variations of intensity at different Y locations. Figure 6.3 indicates that for a cold background plate with hot gas plumes, the intensity has its maximum value at $Y = 0$ and minimum value at $Y = R$. The intensity peak values are different for each wavelength due to the strong dependence of the absorption coefficients on wavelength. Figure 6.4 shows the minimum intensity at $Y = 0$ and maximum value at $Y = R$, for the case of hot background plate and cold gas plume. Most of the incoming intensity

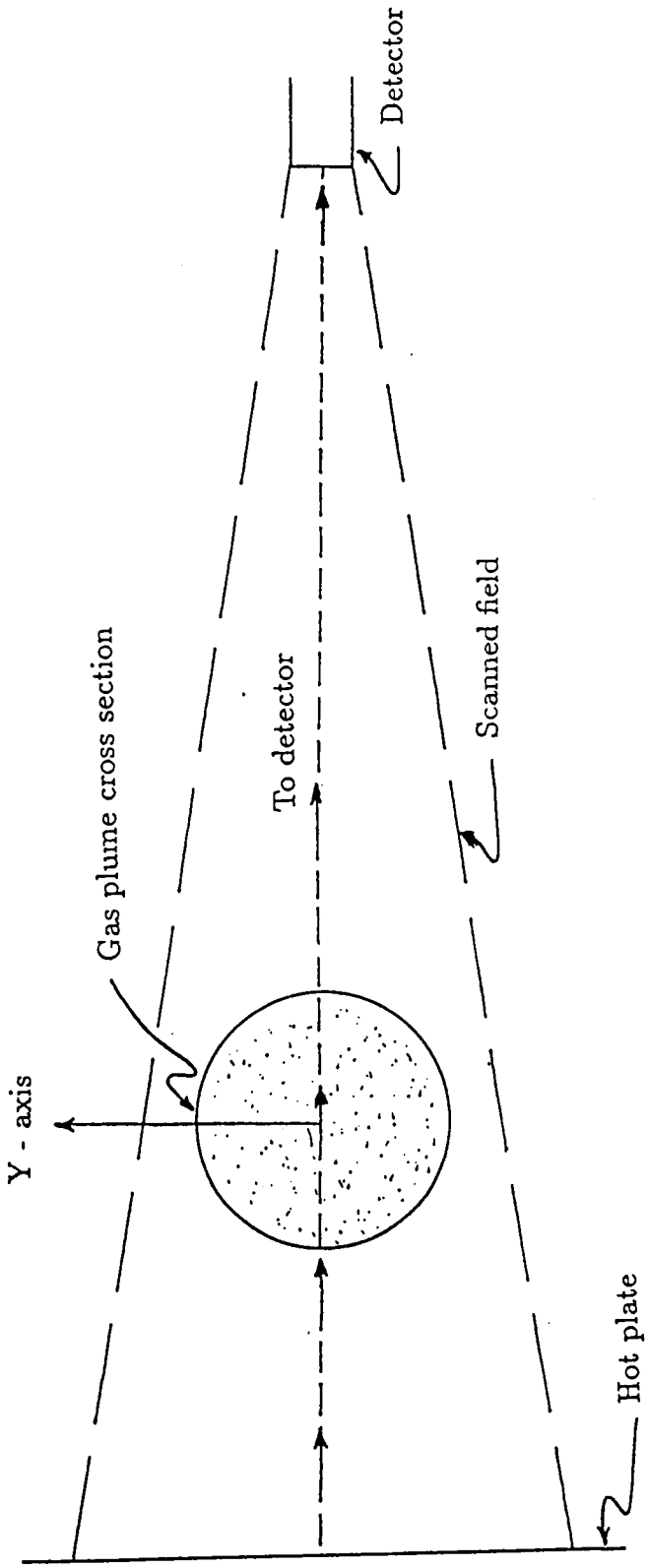


Figure 6.1 Geometrical arrangement.

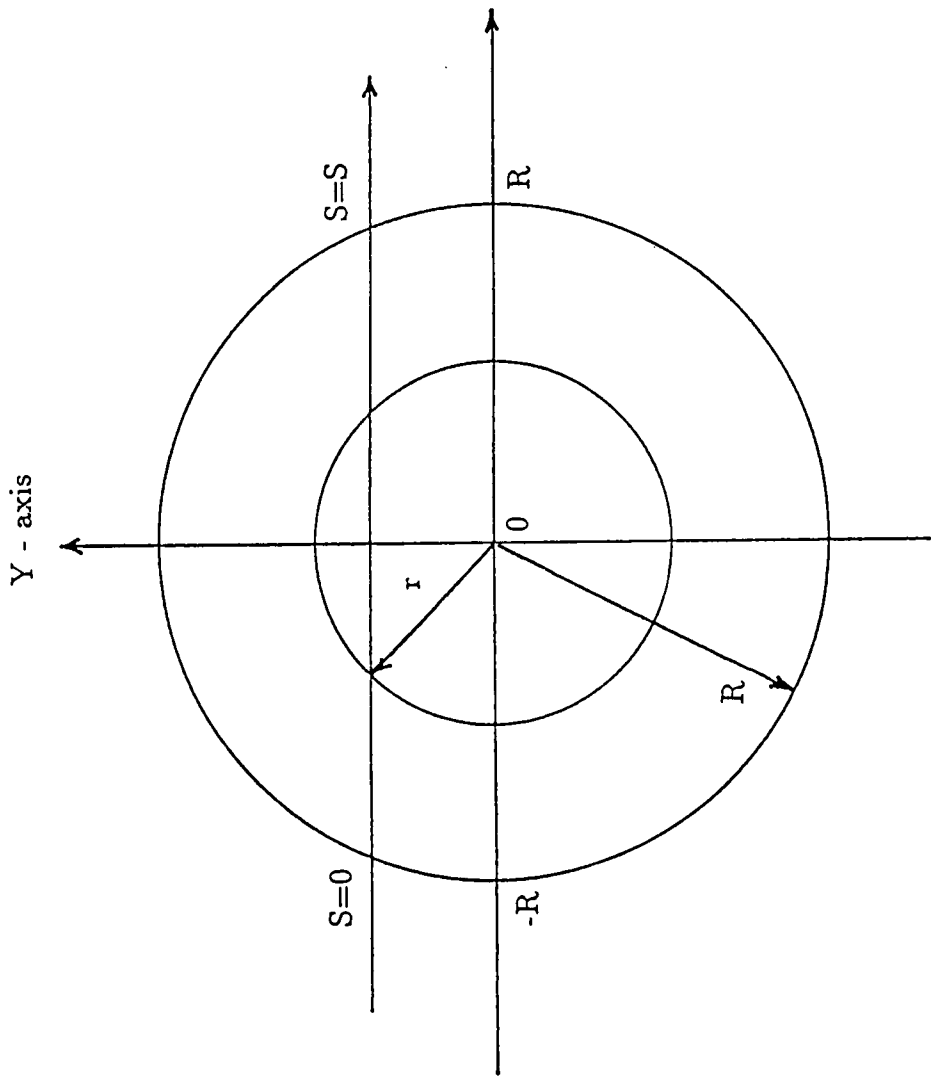


Figure 6.2 Plume cross section for numerical calculation

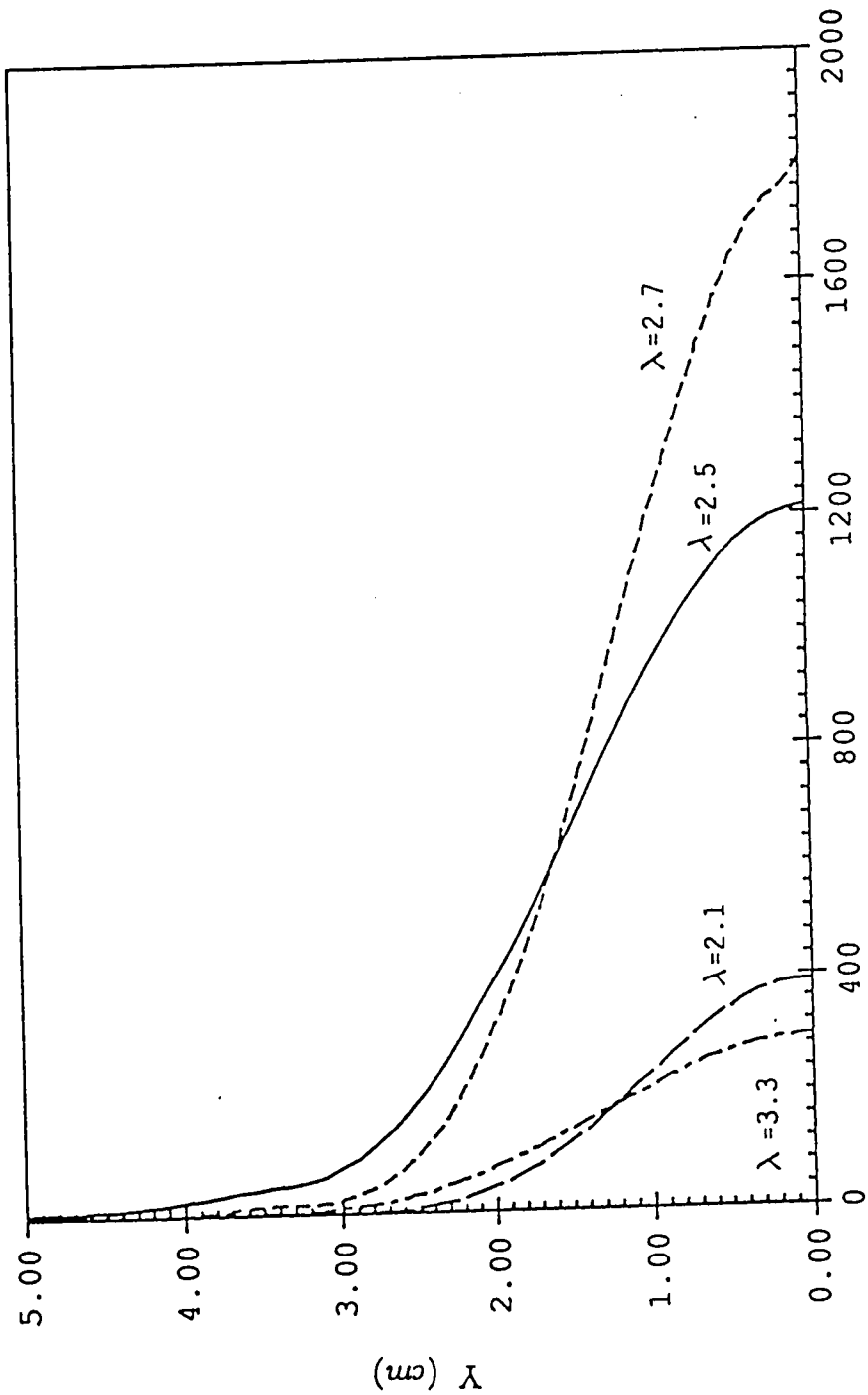


Figure 6.3 Spectral intensity vs. Y for cold background plate with hot gas plume.
($T_p = 300°K$, $T_{max} = 1000°K$, $T_{min} = 300°K$)

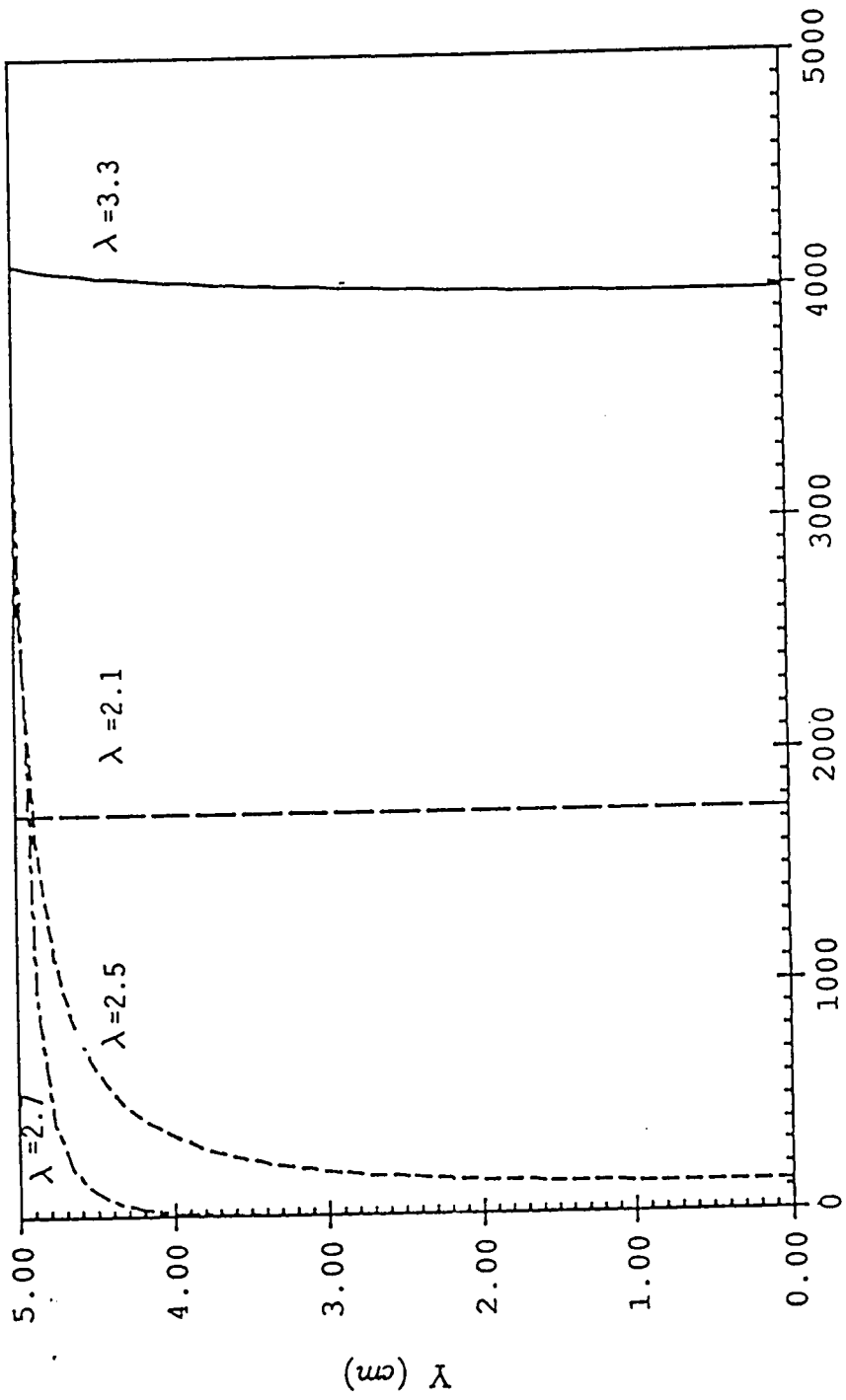


Figure 6.4 Spectral intensity vs. Y for hot background plate with cold gas plume.
($T_p = 800°K$, $T_{max} = 400°K$, $T_{min} = 300°K$)

will be absorbed by cold gas at the center line, where $Y = 0$ and S is maximum. At larger values of Y the travel path, S, becomes shorter resulting in a reduced absorption of the incoming energy.

The variation of intensity with wavelength is shown in Figures 6.5 and 6.6. For the case of hot plate with a cold plume, Figure 6.5 indicates that most of the incoming energy has been absorbed at wavelengths between 2.4 and 2.9 μ for different Y values, but for the case of cold plate with a hot gas plume, Figure 6.6 shows that most of the energy has been emitted by the hot gas. The results from Figures 6.5 and 6.6 suggest the choice of a band filter of 2.4 - 2.9μ for the IR camera. This indicates that at this wavelength range, most of the incoming energy has been absorbed or emitted by the gas plume.

Intensity variation as a function of wavelength for three different plume diameters is shown in Figure 6.7. This figure indicates that the absorption effect is significant even for very small plume sizes. The cold gas absorbs the incoming intensity from warm background, mostly in the wavelengths between 2.36 and 3.2μ and some in the wavelength range of 4.52 to 5.0 μ. The amount of absorption depends on the actual size of the plume which reflects the increase of the plume absoption depth. Figure 6.8 shows the similar effect for plume sizes from 4.0 to 6.0 cm diameter. The effect of emission is clearly shown at $\lambda = 2.7\mu$ which has its maximum peak value at this wavelength.

The integrated intensity is defined by equation (4-12) which is equivalent to the area under the curves in Figure 6.8. These curves are similar to the Figures 6.6 and 6.7. The integrated results for $2.0 \leq \lambda(\mu) \leq 5.0$ are shown in Figures 6.9 and 6.10. The integrated intensities as a function of the actual distance across the plate geometry are plotted in these figures. These integrated intensities are related to the ambient, plate, and plume temperatures. The ambient integrated

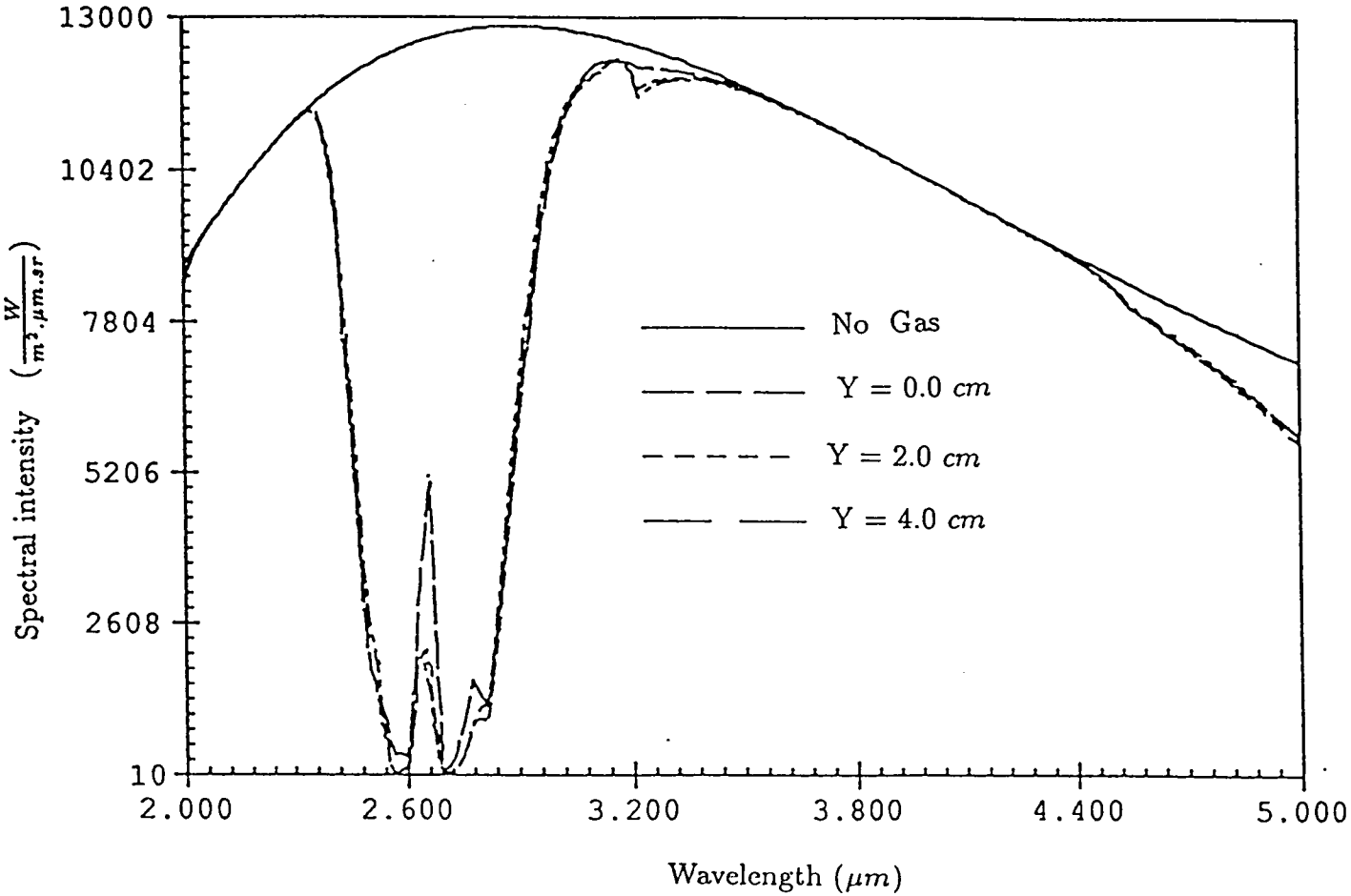


Figure 6.5 Spectral intensity vs. wavelength for hot background plate with cold gas plume at different Y locations.
($T_p = 1000^o K$, $T_{max} = 600^o K$, $T_{min} = 300^o K$)

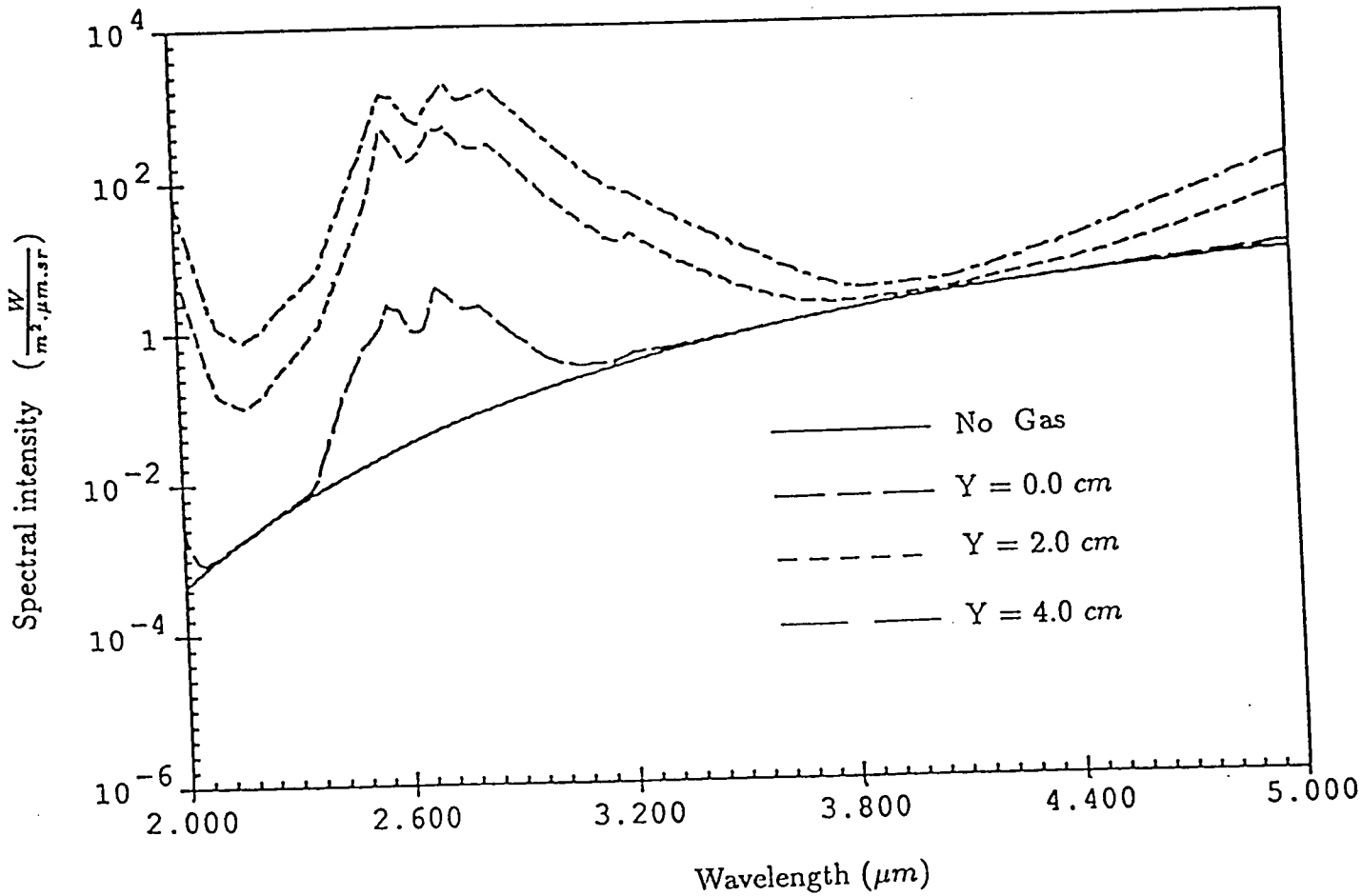


Figure 6.6 Spectral intensity vs. wavelength for cold background plate with hot gas plume at different Y locations.
($T_p = 300^oK$, $T_{max} = 1000^oK$, $T_{min} = 300^oK$)

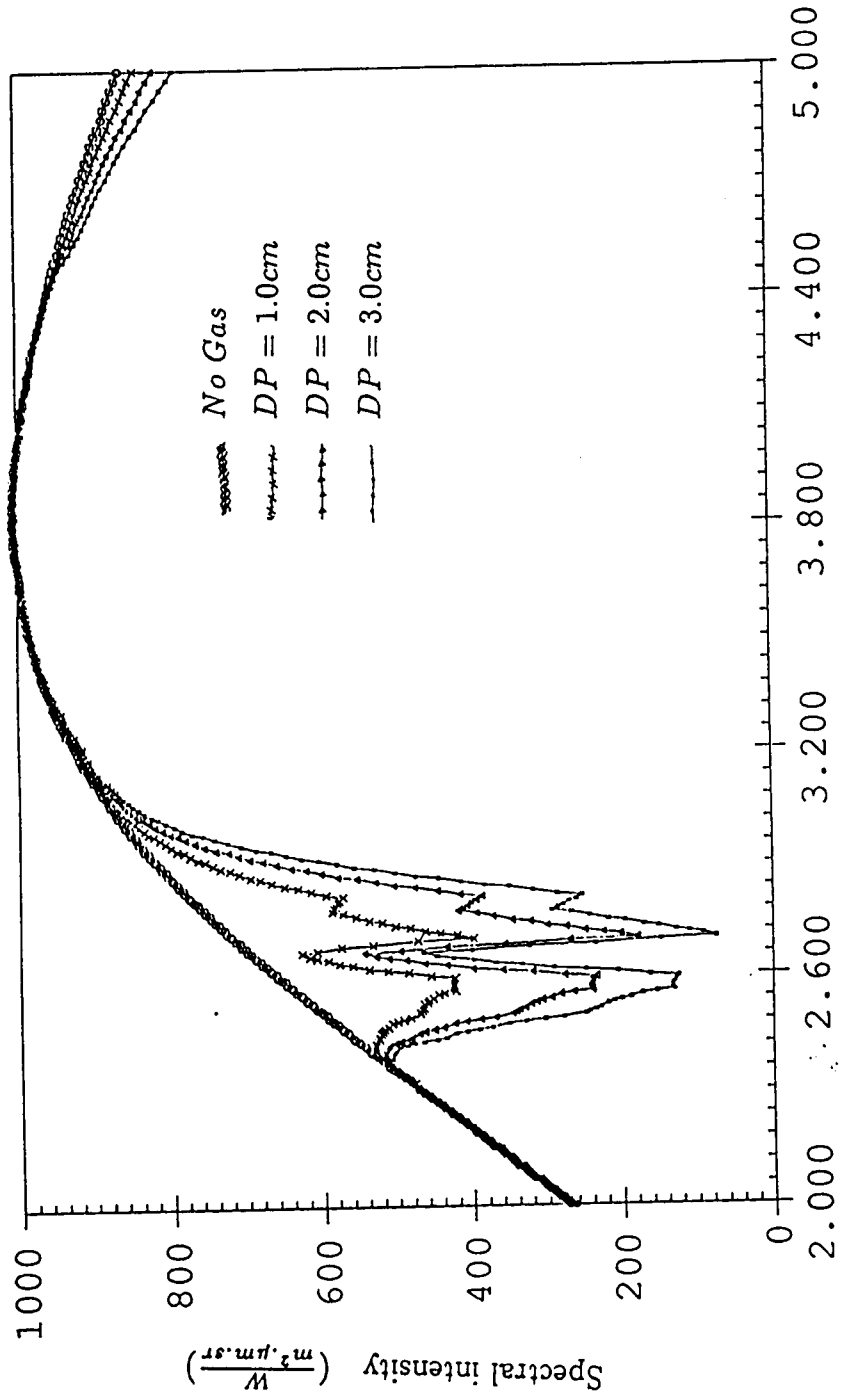


Figure 6.7 Spectral intensity vs. wavelength at different plume diameters.
($T_p = 755°K$, $T_{max} = 373°K$, $T_{min} = 300°K$)

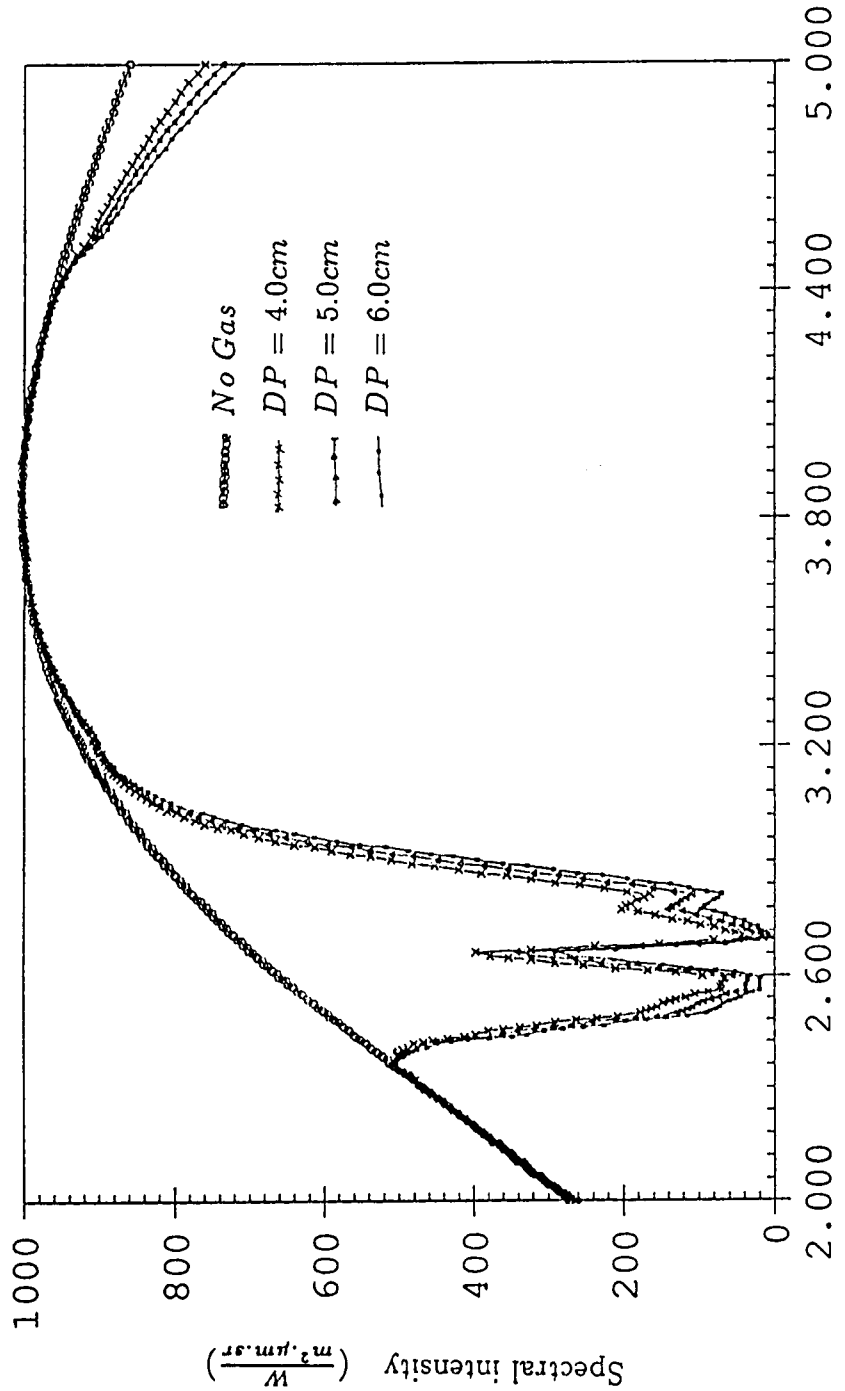


Figure 6.8 Spectral intensity vs. wavelength at different plume diameters.
($T_p = 755°K$, $T_{max} = 373°K$, $T_{min} = 300°K$)

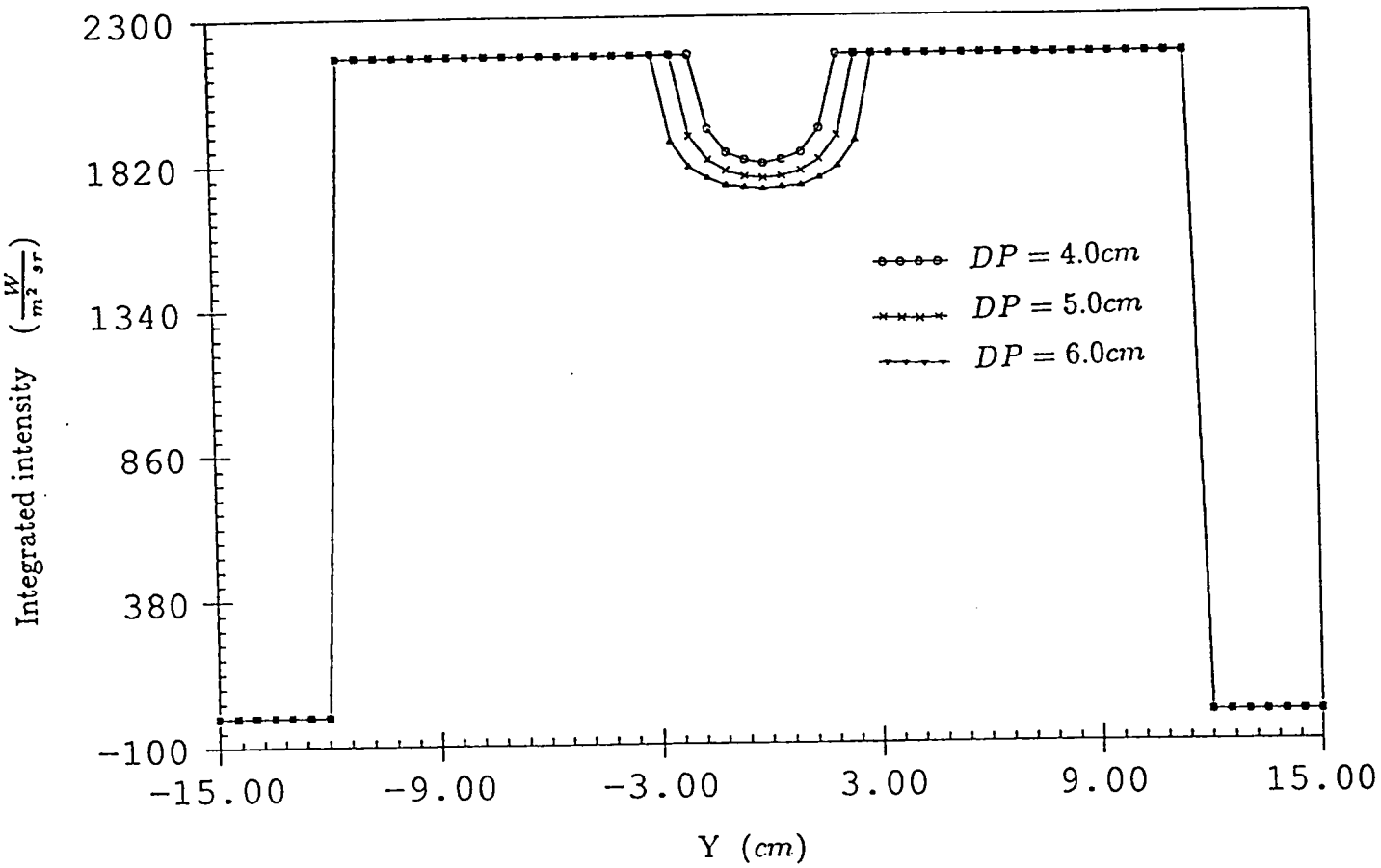


Figure 6.9 Integrated intensity vs. Y at different plume diameters.
($T_p = 755^oK$, $T_{max} = 373^oK$, $T_{min} = 300^oK$ and $2.0 \leq \lambda \leq 5.0\mu m$)

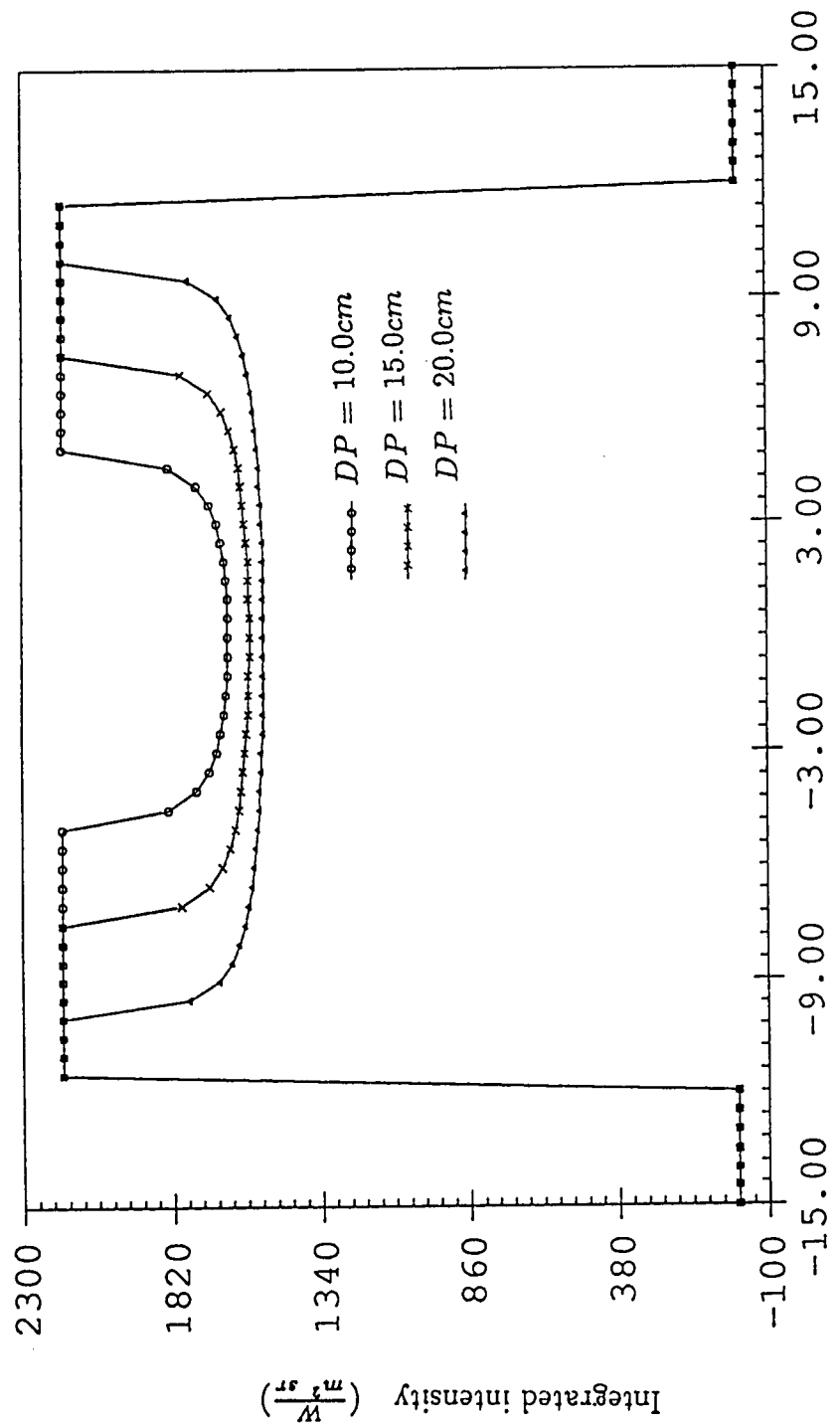


Figure 6.10 Integrated intensity vs. Y at different plume diameters.
($T_p = 755°K$, $T_{max} = 373°K$, $T_{min} = 300°K$ and $2.0 \leq \lambda \leq 5.0\mu m$)

intensity is shown in the interval of $-15.0 \leq Y(cm) \leq -12.0$ and $15.0 \geq y(cm) \geq 12.0$. The observed value of plate integrated intensity is shown for $-12.0 \leq y(cm) \geq +12.0$; it decreases in the center, due to the presence of the absorbing plume. This decay of the integrated intensity is due to the combination of absorption and emission of the plume. The reduction of the integrated intensity for three different plume sizes are shown in Figures 6.9 and 6.10. The maximum absorption effect appears at the center of the plume (at $Y = 0$) which is directly related to the plume sizes. The value of the minimum of integrated intensity decreases with increased plume diameter. The leak size is directly proportional to the extent of reduction in the integrated intensity and this can be used as a calibration technique for the leak size.

Figures 6.11 and 6.12 show the reduction of the incoming integrated intensity from background radiation for a wavelength range of $2.5 \leq \lambda(\mu) \leq 2.86$. This wavelength range has been chosen with the aid of Figures 6.7 and 6.8 which indicates that most of the the background intensities will be absorbed by the plume in this range. The results from these figures prove that for this narrow wavelength band, the integrated intensity reduces much more than for the case of the wavelength band $2.0 \leq \lambda(\mu) \leq 5.0$ indicated by Figures 6.9 and 6.10. One should notice that even though the integrated intensity reduction is much more noticeable in the case of $2.5 \leq \lambda(\mu) \leq 2.86$ than for the case of $2.0 \leq \lambda(\mu) \leq 5.0$, the integrated incoming intensity is also reduced dramatically. This can be seen by comparing the maximum values of the intensity on these figures.

The percentage of the integrated intensity reduction, due to the absorption by the plume, as a function of the plume radius is shown in Figure 6.13. As it appears, the percentage of the integrated intensity increases with the increase of the plume radius. For the case of $2.5 \leq \lambda(\mu) \leq 2.86$, the percentage of integrated

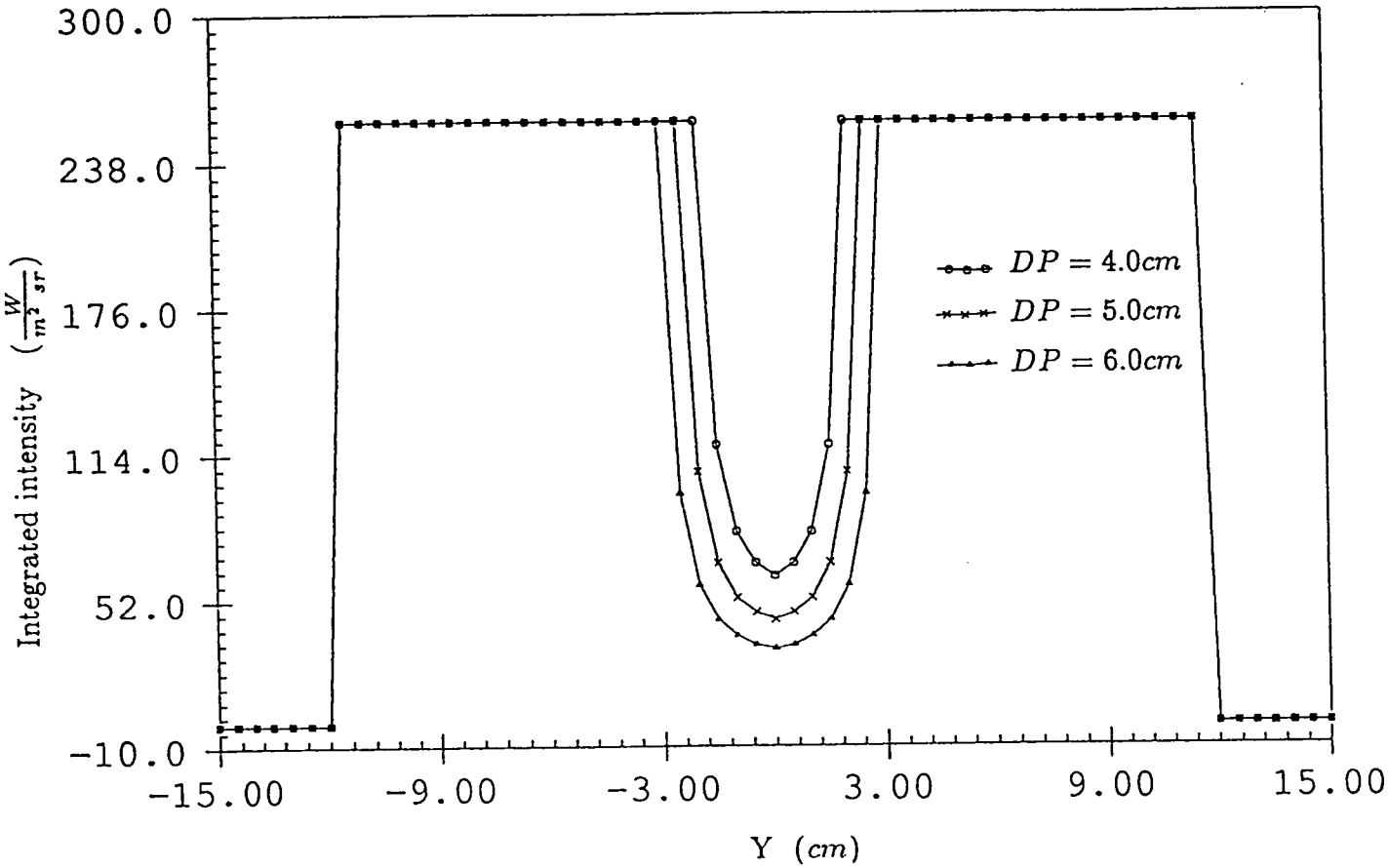


Figure 6.11 Integrated intensity vs. Y at different plume diameters.
($T_p = 755°K$, $T_{max} = 373°K$, $T_{min} = 300°K$ and $2.5 \leq \lambda \leq 2.86\mu m$)

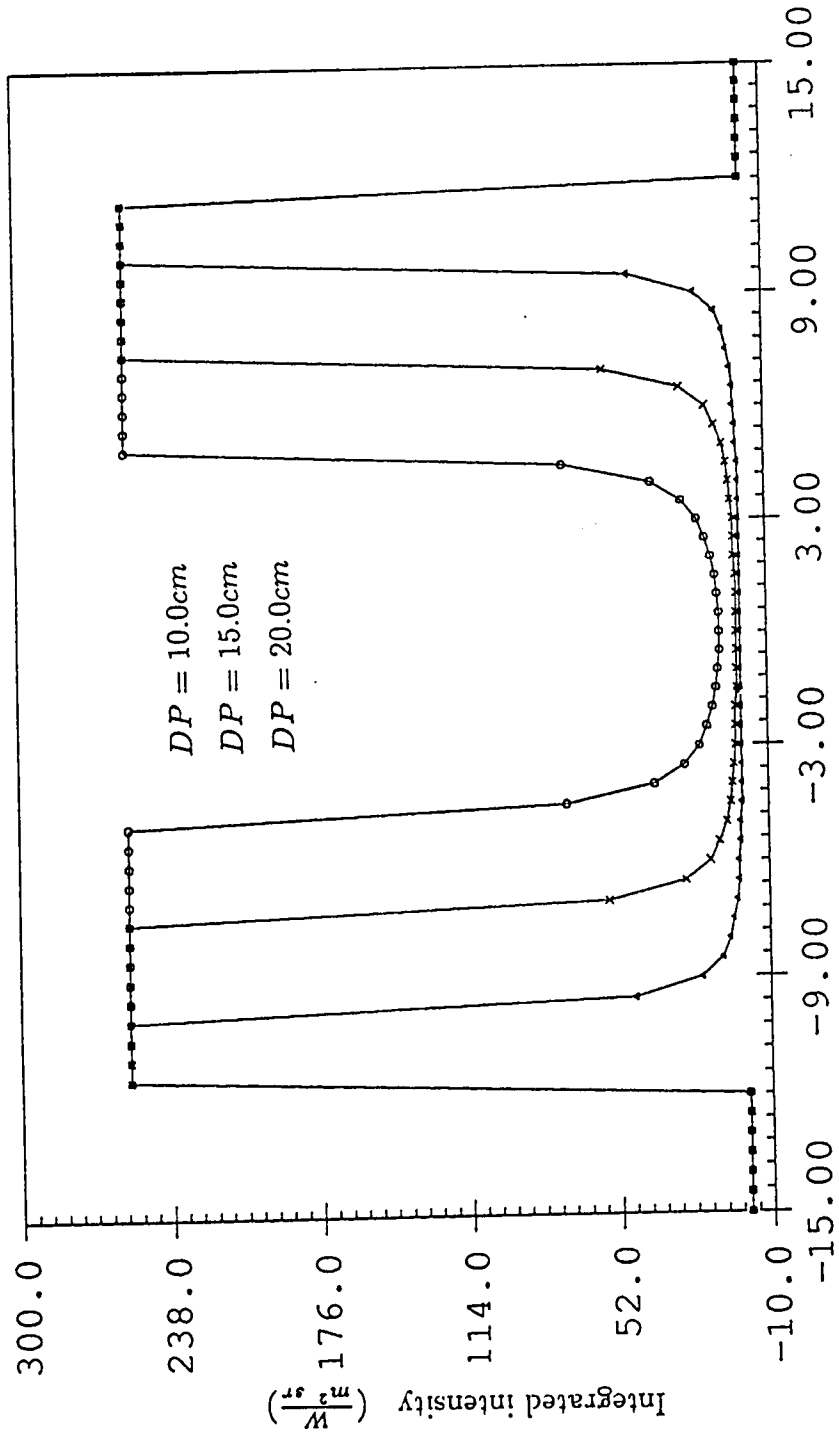


Figure 6.12 Integrated intensity vs. Y at different plume diameters.
($T_p = 755°K$, $T_{max} = 373°K$, $T_{min} = 300°K$ and $2.5 \leq \lambda \leq 2.86\mu m$)

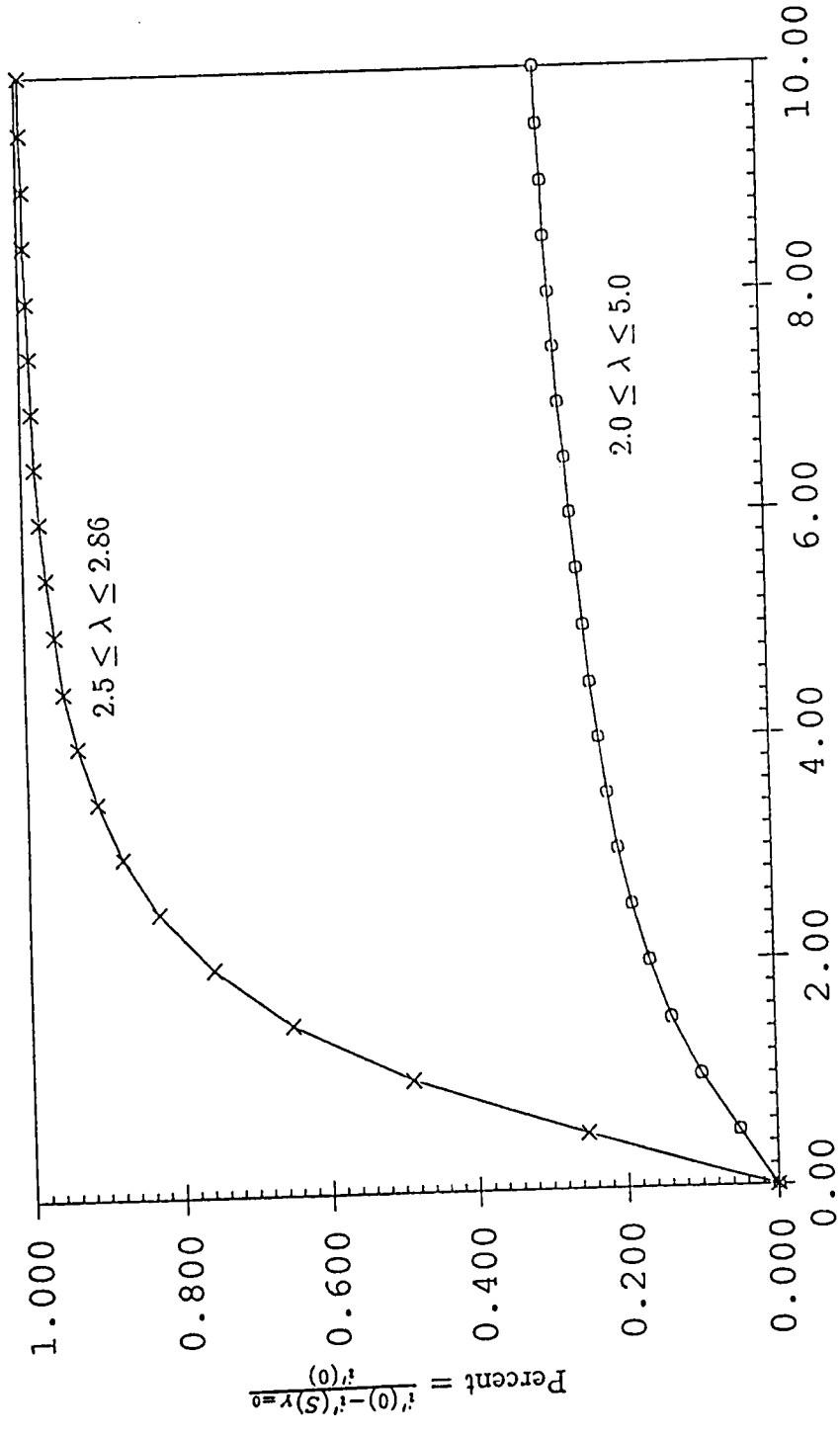


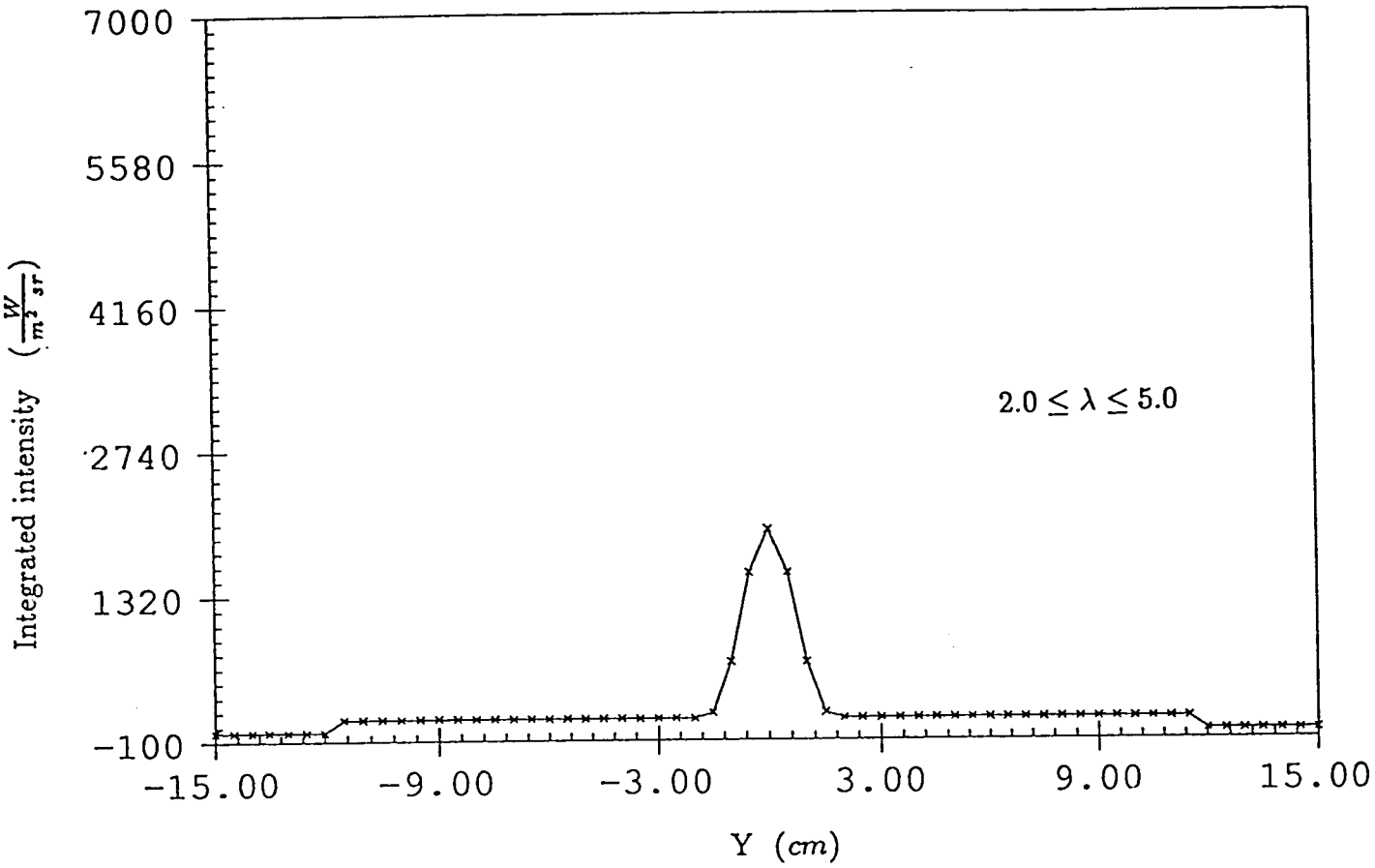
Figure 6.13 Percentage of Integrated intensity reduced vs. R
($T_p = 755°K$, $T_{max} = 373°K$, $T_{min} = 300°K$)

intensity reduction is about 100% at $R = 10$. Similarly for the case of $2.0 \leq \lambda(\mu) \leq 5.0$, the percentage of integrated intensity reduction is only about 30% at the same value of $R = 10$.

These important results indicate that there is a distinct region of the spectra that can be utilized to monitor the major types of gas leaks. The region from 2.5 to 2.9 μ can be used to monitor leaks which are along the line-of-sight of the optical system and hence are blocking the radiation emitted by the hotter surfaces in the background. The significant reduction of the background radiation intensity in this region is a very sensitive warning signal for leaks of this type.

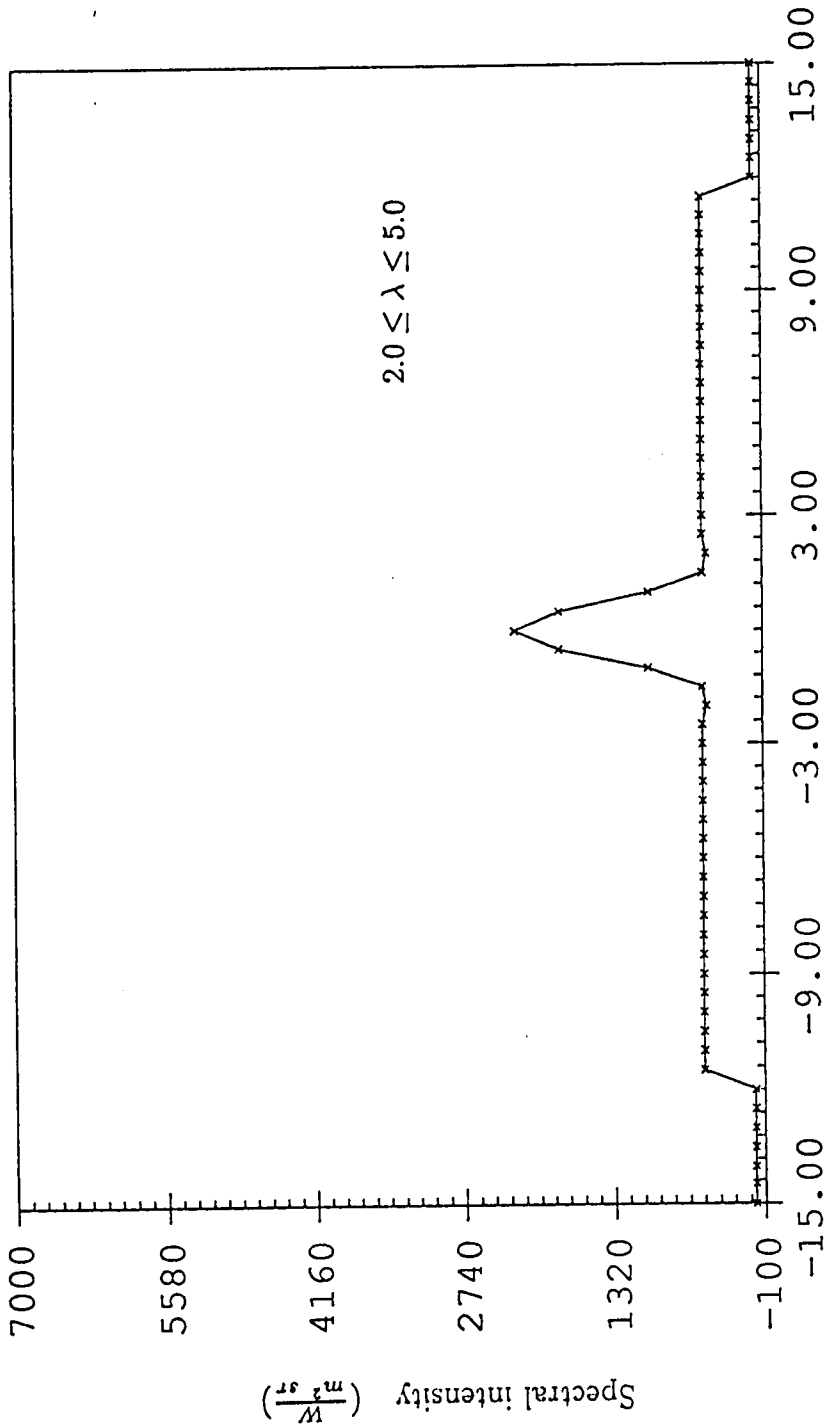
The effect of emission is more pronounced in hotter gases, since the emission of gases at low temperatures will be negligible compared to their absorption. To demonstrate this phenomenon, the following set of results are presented for the case of a hot gas plume against several different background radiation sources.

Figures 6.14a-6.14e show the effect of absorption and spontaneous emission for a fixed plume temperature and a fixed plume cross section. These figures indicate that the integrated incoming intensity increases mainly due to the emission from the hot gas. When the temperature of the background radiation source increases, the effect of the absorption will be more noticeable. The effect of the media absorption is shown in Figures 6.14c-6.14e. Figure 6.14c indicates that with the plate temperature of $700^{o}K$, the absorption effect can be seen near the edges of the plume, since the plume has its lowest value ($300^{o}K$) in that areas. Near the center of the plume, where the temperature has its maximum value, the emission of the gas becomes more significant than the absorption effect. Similar phenomenon occurs for plates with higher temperature, as it shown in Figures 6.14d and 6.14e.

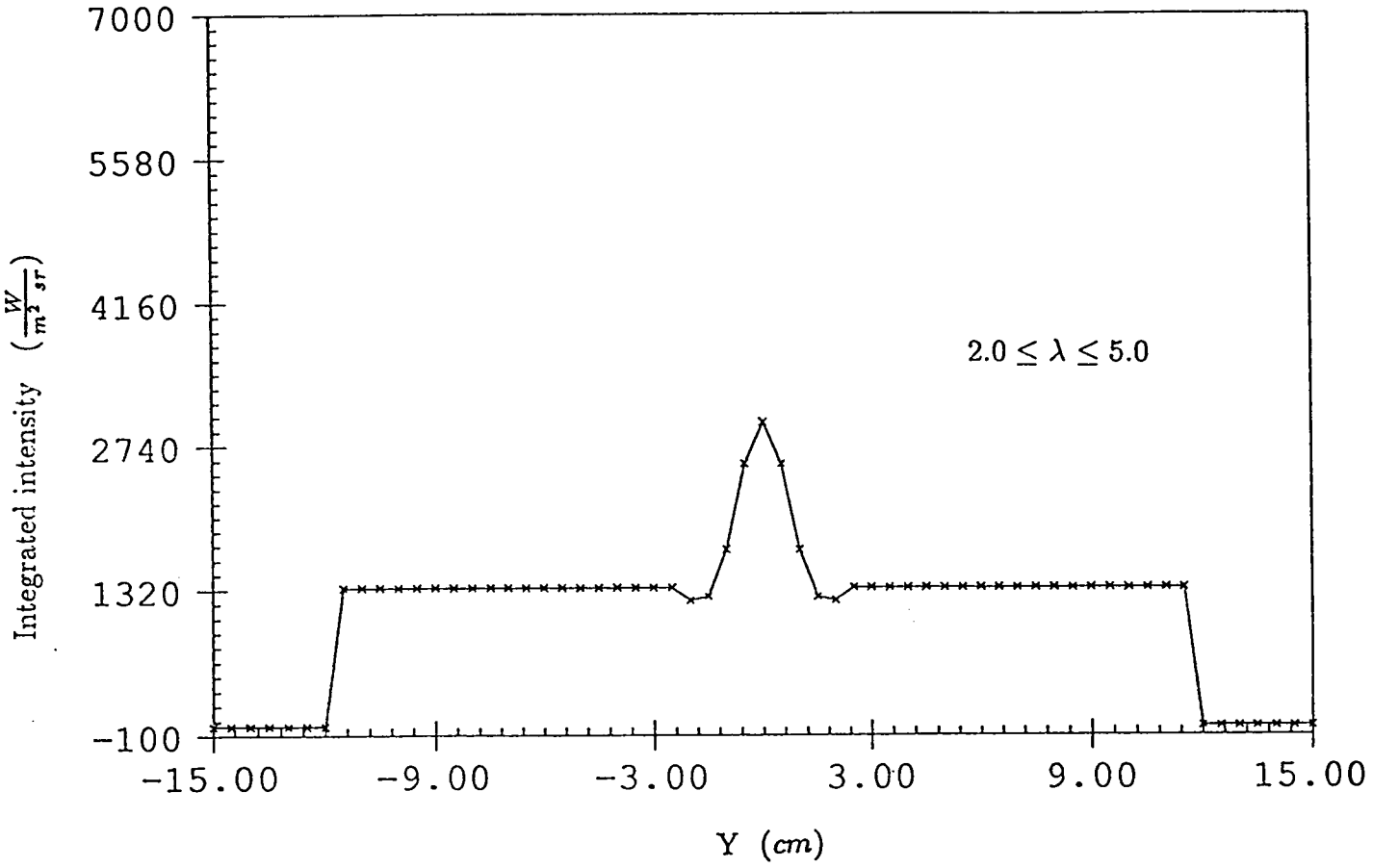


a. $T_p = 500°K$

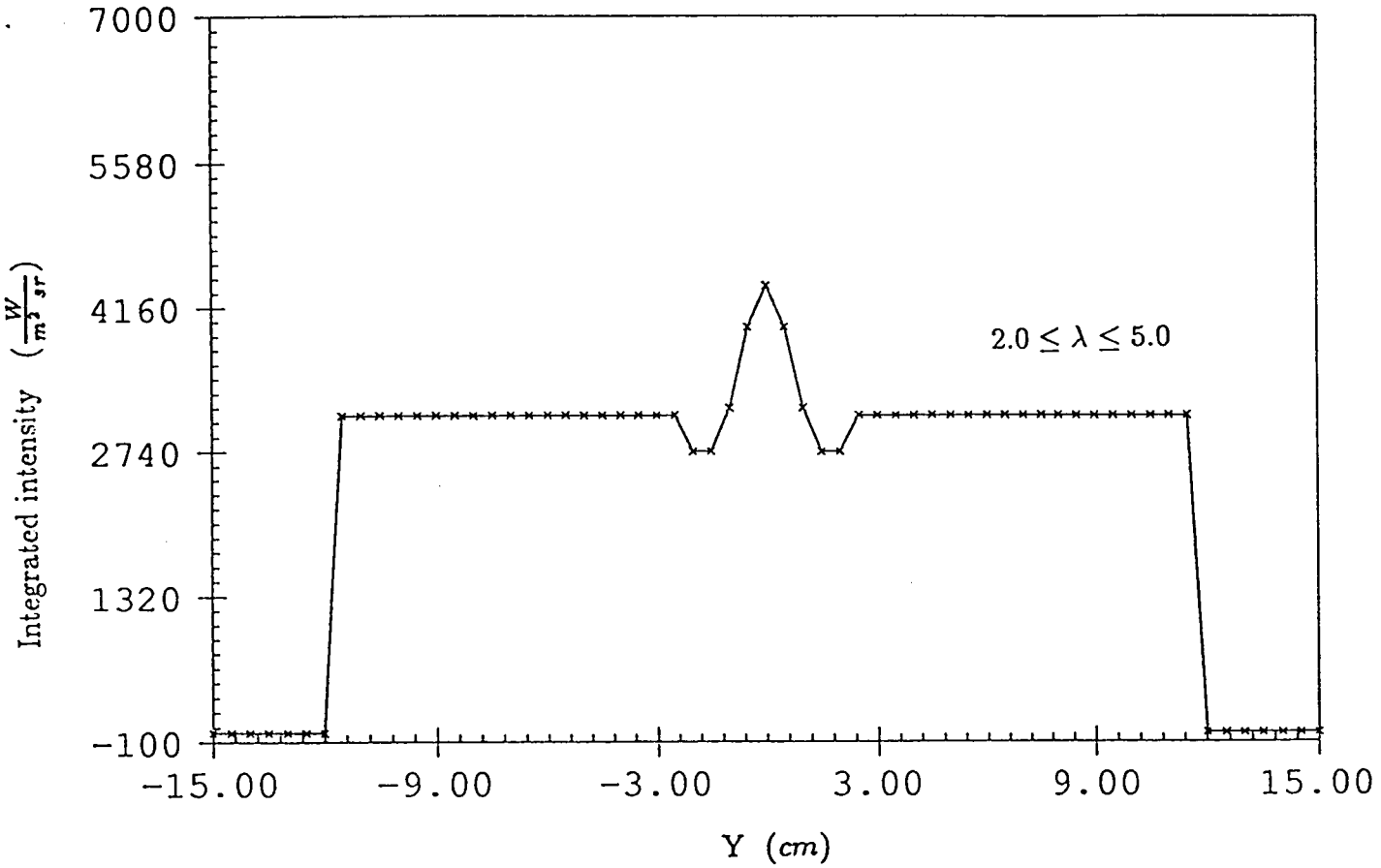
Figure 6.14 Integrated intensity vs. Y at different plate temperatures.
($T_{max} = 1200°K$, $T_{min} = 300°K$ *and* $DP = 5.0$ *cm*)


7000
5580
4160
2740
1320
-100
Spectral intensity $\left(\frac{W}{m^2 sr}\right)$
-15.00
-9.00
-3.00
3.00
9.00
15.00
Y (cm)
$2.0 \leq \lambda \leq 5.0$

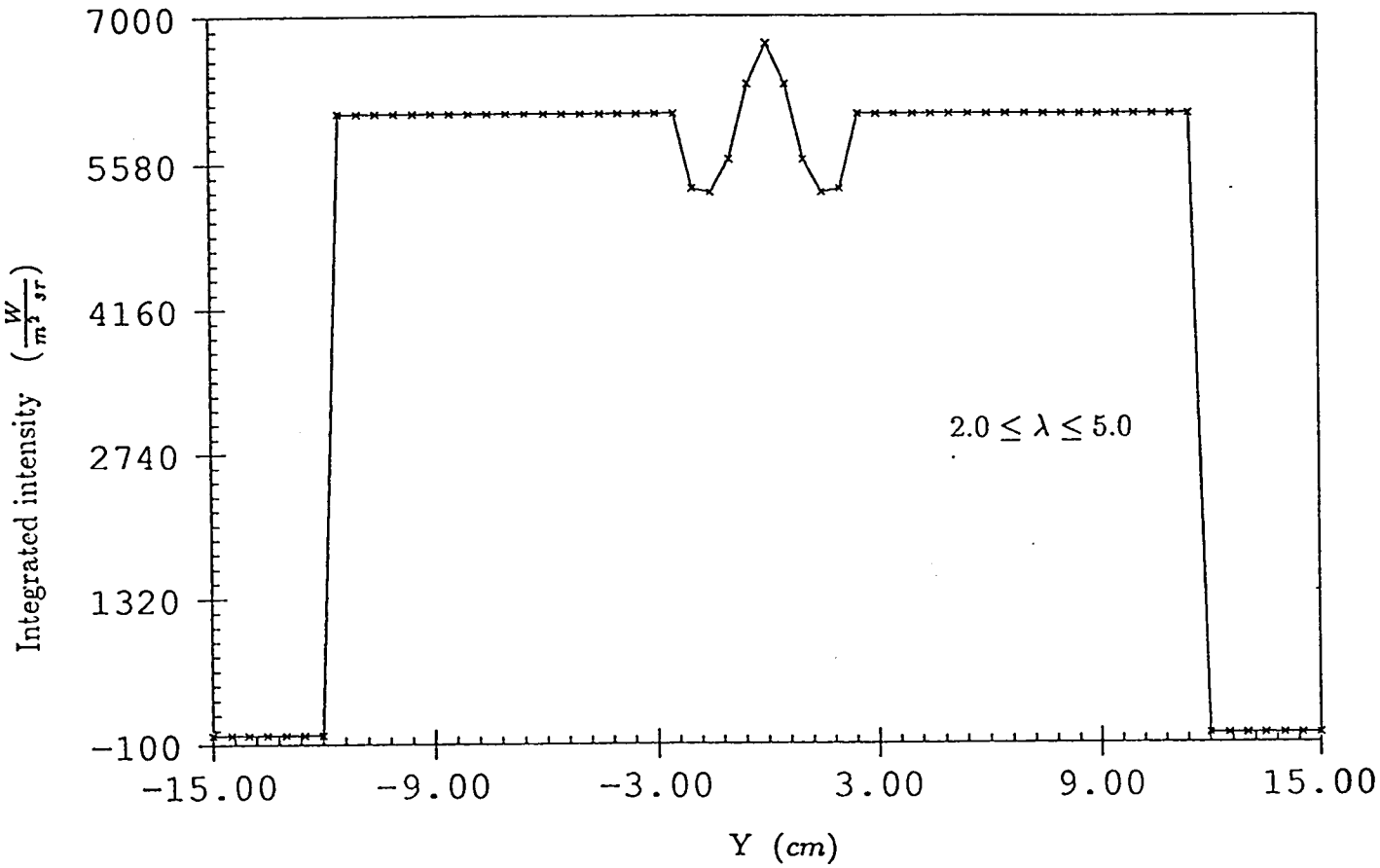
b. $T_p = 600°K$


7000
5580
4160
2740
1320
-100
Integrated intensity $\left(\frac{W}{m^2\,sr}\right)$
$2.0 \leq \lambda \leq 5.0$
-15.00
-9.00
-3.00
3.00
9.00
15.00
Y (cm)

c. $T_p = 700°K$


7000
5580
4160
2740
1320
-100
Integrated intensity $(\frac{W}{m^2\,sr})$
$2.0 \leq \lambda \leq 5.0$
-15.00
-9.00
-3.00
3.00
9.00
15.00
Y (cm)

d. $T_p = 800°K$


7000
5580
4160
2740
1320
-100
Integrated intensity $(\frac{W}{m^2\ sr})$
$2.0 \leq \lambda \leq 5.0$
-15.00
-9.00
-3.00
3.00
9.00
15.00
Y (cm)

e. $T_p = 900°K$

6.2 Blackbody Radiation Source With Absorbing, Emitting and Scattering Media

Numerical results for radiation transport in absorbing, emitting, and isotropic scattering media will be presented in this section. The scattering coefficient is needed to calculate the radiation transport equation when scattering is included in the radiation calculation. The scattering coefficients have been calculated with the help of the absorption coefficients and non-dimensional values of albedo, $\Omega_{0\lambda}$. The albedo for scattering is defined as the ratio of the scattering coefficient, $\sigma_{s\lambda}$, to the extinction coefficient, $K_\lambda = \sigma_{s\lambda} + a_\lambda$,

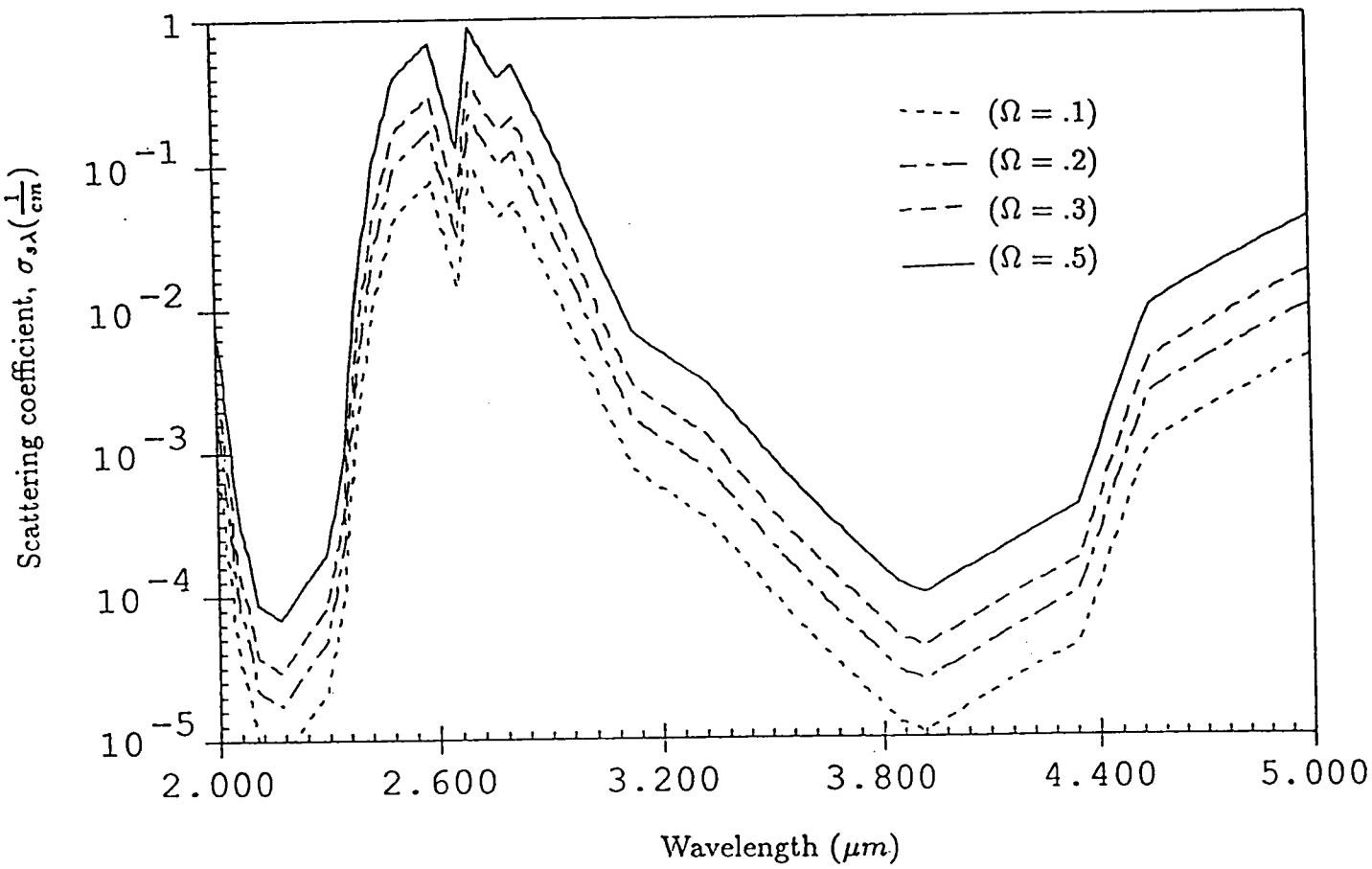
$$\Omega_{0\lambda} \equiv \frac{\sigma_{s\lambda}}{K_\lambda} \qquad (6-1)$$

where a_λ is absorption coefficient. This equation can be rearranged to give a equation for scattering coefficient which is

$$\sigma_{s\lambda} = \left[\frac{\Omega_{0\lambda}}{1-\Omega_{0\lambda}}\right] a_\lambda \qquad (6-2)$$

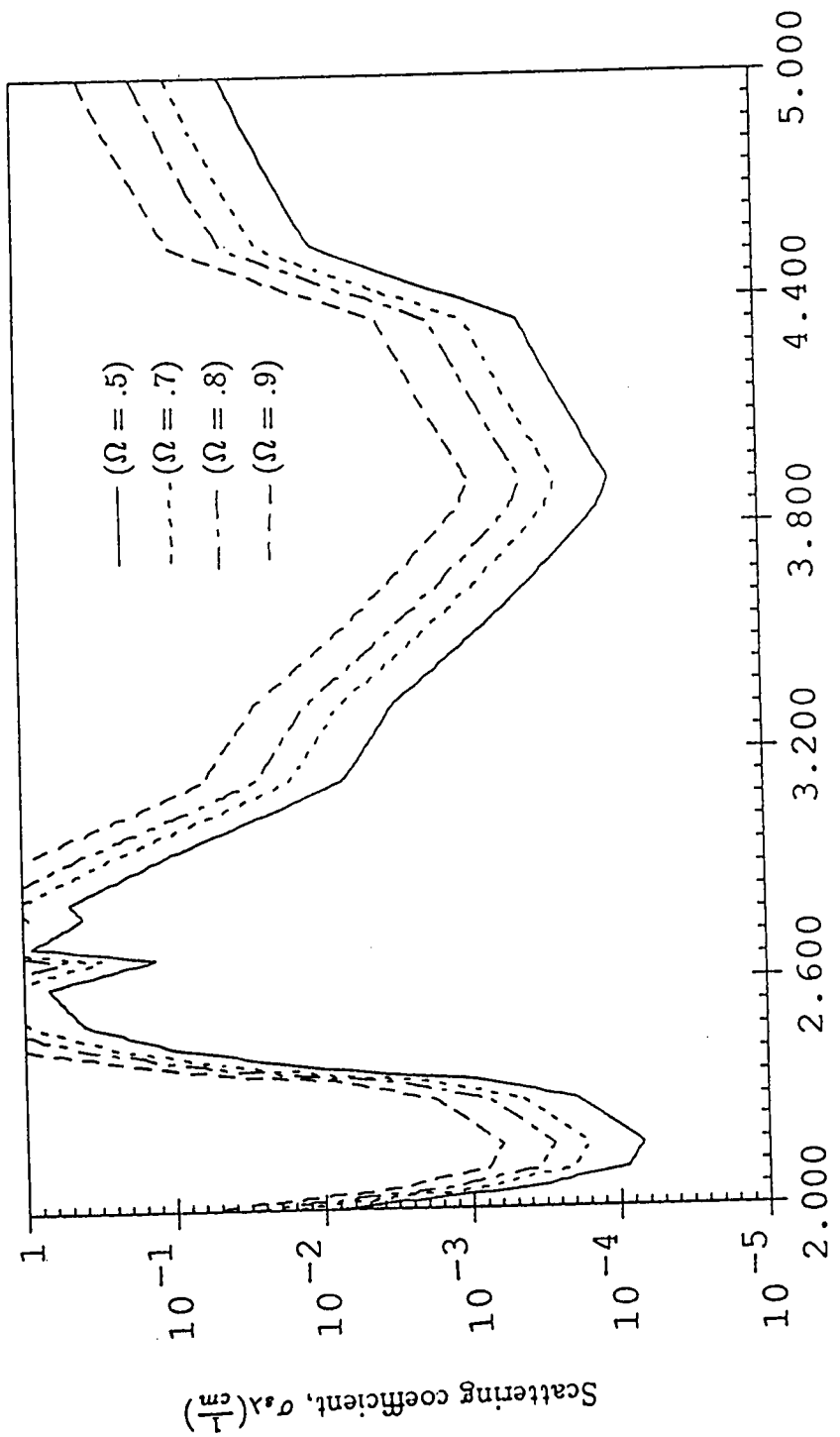
Since absorption coefficients are known at fixed temperatures and wavelength intervals, scattering coefficients can be evaluated at a fixed albedo for those temperatures and wavelengths. Figures 6.15a and 6.15b show the variation of absorption coefficient for albedos of 0.1 - 0.9 with plume temperature of $300^o K$ and wavelength interval of 2 to 5μ

The source function equation for isotropic scattering was developed in chapter IV. For isotropic scattering, the source function equation (5-4) is coupled with the local intensity in the media. This equation must be solved simultaneously with the intensity equation (5-3). The effect of the source function versus wavelength for different values of albedo is shown in Figure 6.16. This figure indicates that for small albedo, the values of source function are very close to the blackbody



a. $0.1 \leq \Omega \leq 0.5$

Figure 6.15 Scattering coefficient vs. wavelength at a fixed temperature of $300°K$.



b. $0.5 \leq \Omega \leq 0.9$

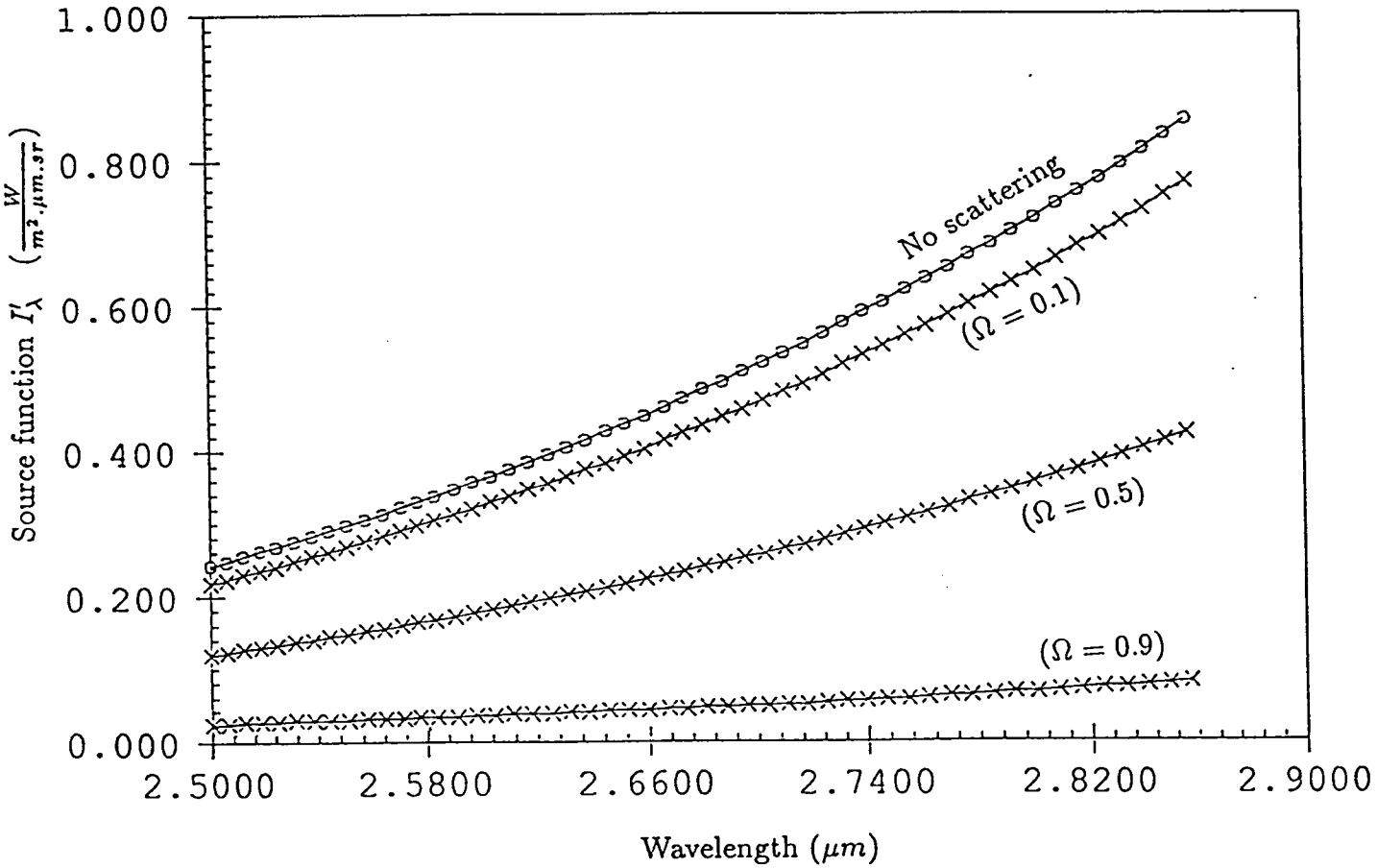


Figure 6.16 Source function vs. wavelength at diferent albedos
($T_p = 755°K$, $T_{max} = 373°K$, $T_{min} = 300°K$, $DP = 10cm$, and Y=0.0)

intensity and for higher values of albedo these values become smaller than black-body intensity.

Figure 6.17 is the comparison of source function as a function of distance, S, through the plume at a single wavelength and fixed albedo. Presence of scattering reduces the value of the source function across the plume cross section at $Y = 0$. Figures 6.18a and 6.18b are similar to the Figures 6.17, but for different fixed wavelengths. As is shown in these figures, for all values of λ, similar profiles are created but at different levels.

Variation of intensity with wavelength is shown in Figures 6.19 which indicates that for low values of albedo and moderately warm background plates the scattering effect is not very noticeable. The effect of scattering for higher values of $\Omega_{0\lambda}$ is shown in this figure. Increasing the values of the $\Omega_{0\lambda}$ will expand the wavelength band which means incoming intensity will be reduced much more for the $\Omega_{0\lambda}$ =0.9 than for $\Omega_{0\lambda}$ =0.1. This effect can be understood because for higher values of albedo the extinction coefficients become greater and so does the optical thickness. The larger optical thickness means less energy can pass through the gas, thus the wavelength range will be larger for this case. In addition, it can be noticed that the emission at $\lambda = 2.7$ is much more pronounced for low values of albedo than high values of albedo which means that scattering effect is stronger than emission.

Figure 6.20 is very similar to Figure 6.19 with the only difference being the higher temperatures for this case. It is important to notice that even though the plate temperature is much higher, since the gas is fairly cold, most of the spectral intensities are absorbed and scattered in wavelength interval of 2.36 - 3.2 μ. In wavelength range of 2.0 to 2.36 μ and 3.56 to 4.4 μ, these figures show that the intensity is totally independent of absorption, emission, and scattering of the

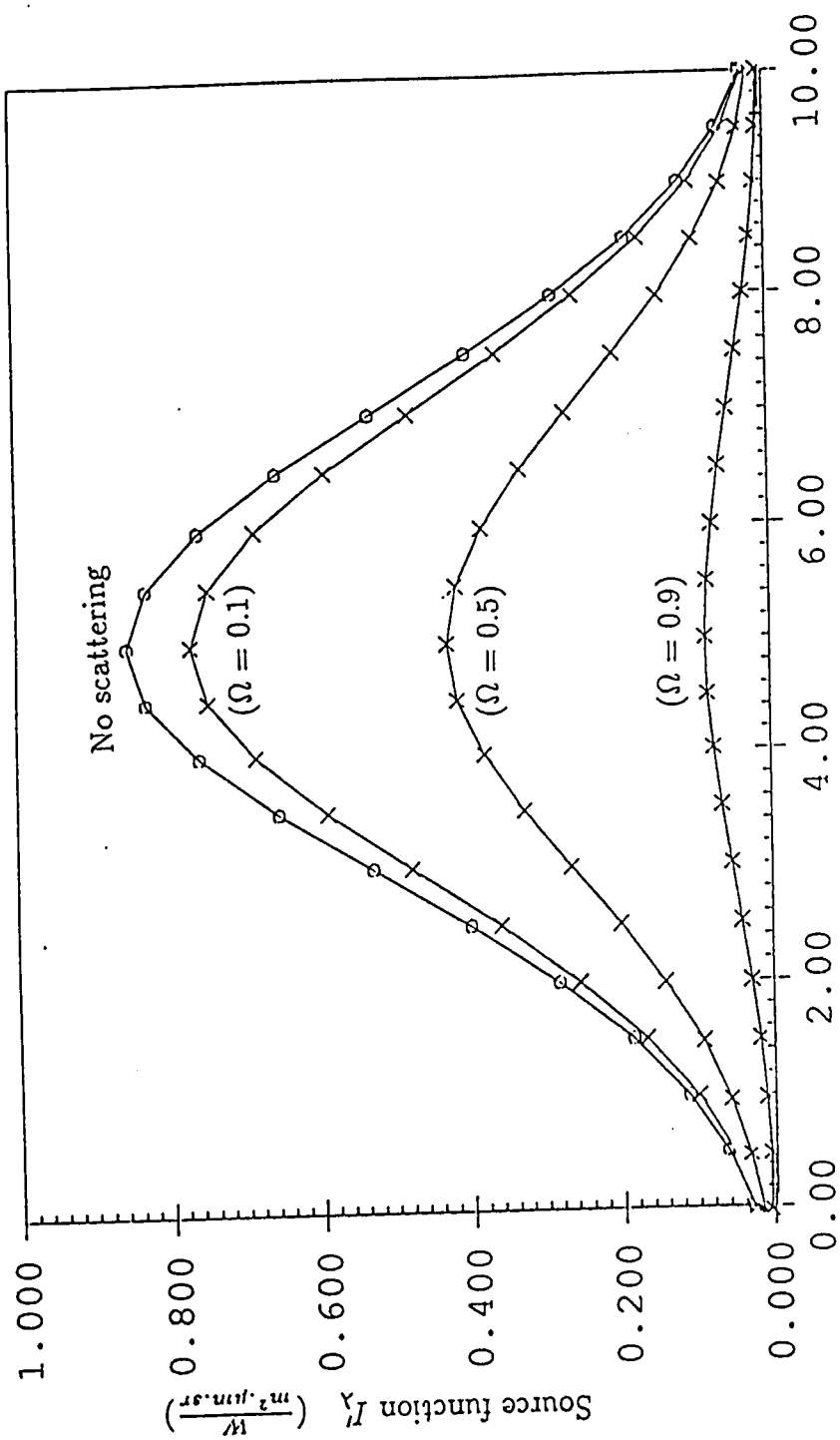
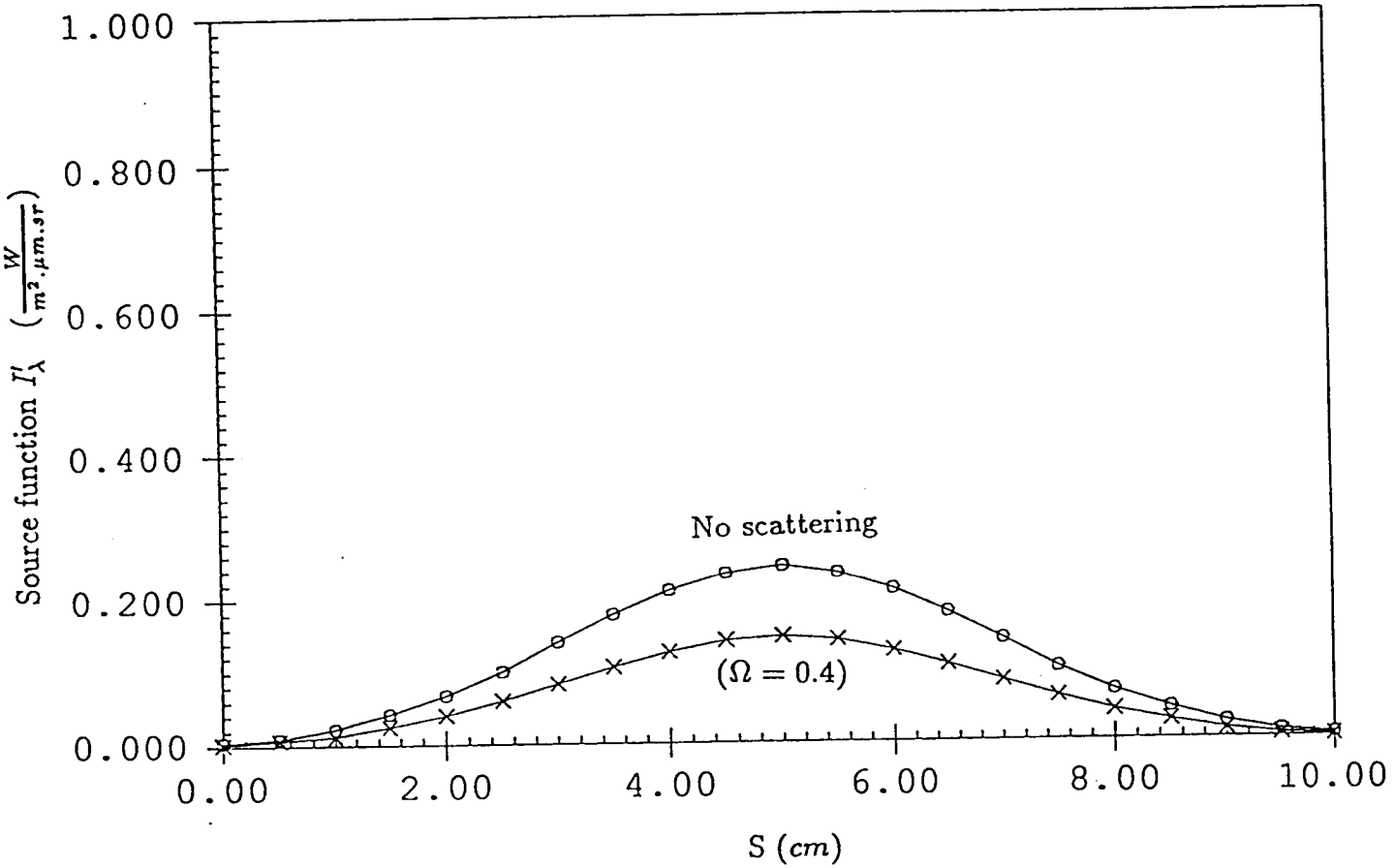
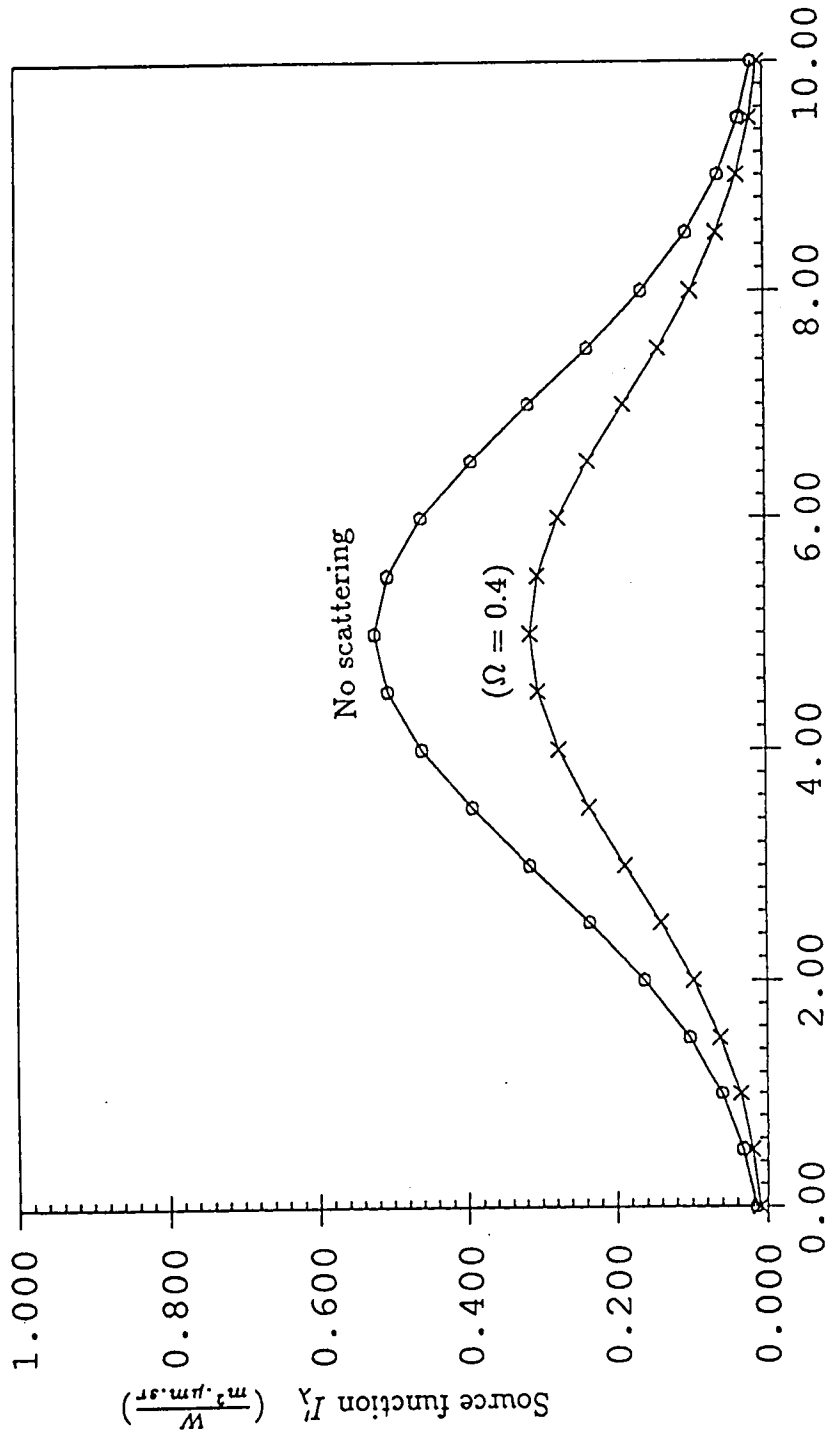


Figure 6.17 Source function vs. position across the plume for different albedos. ($T_p = 755°K$, $T_{max} = 373°K, T_{min} = 300°K, DP = 10\ cm$, $and\ \lambda = 2.86\mu m$)



a. $\lambda = 2.5\mu m$

Figure 6.18 Source function vs. position across the plume.
($T_p = 755°K$, $T_{max} = 373°K$, $T_{min} = 300°K$, $DP = 10\ cm$)



b. $\lambda = 2.7\mu m$

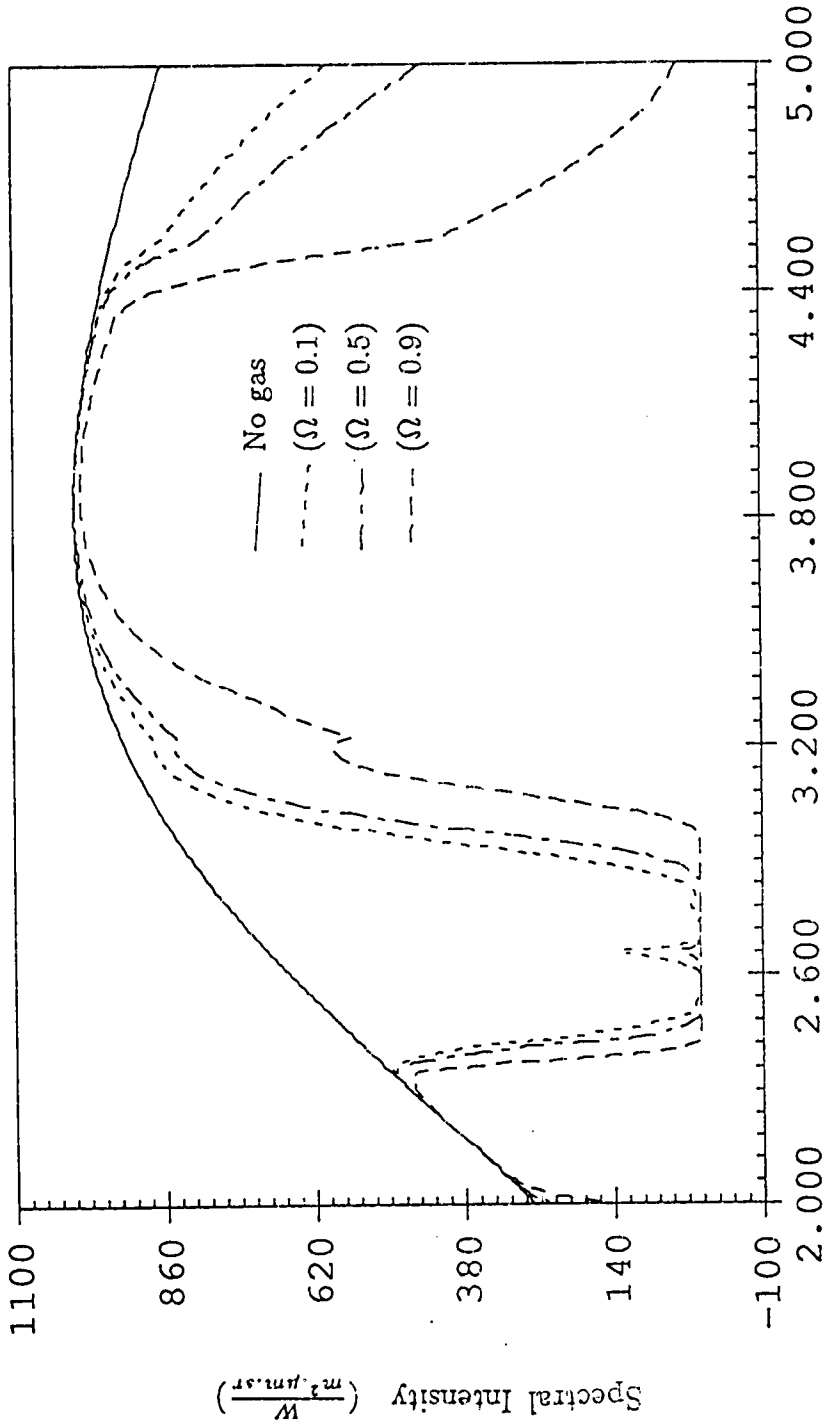


Figure 6.19 Spectral intensity vs. wavelength for hot background plate with cold gas plume. ($T_p = 755°K$, $T_{max} = 373°K$, $T_{min} = 300°K$, *and* $DP = 10cm$)

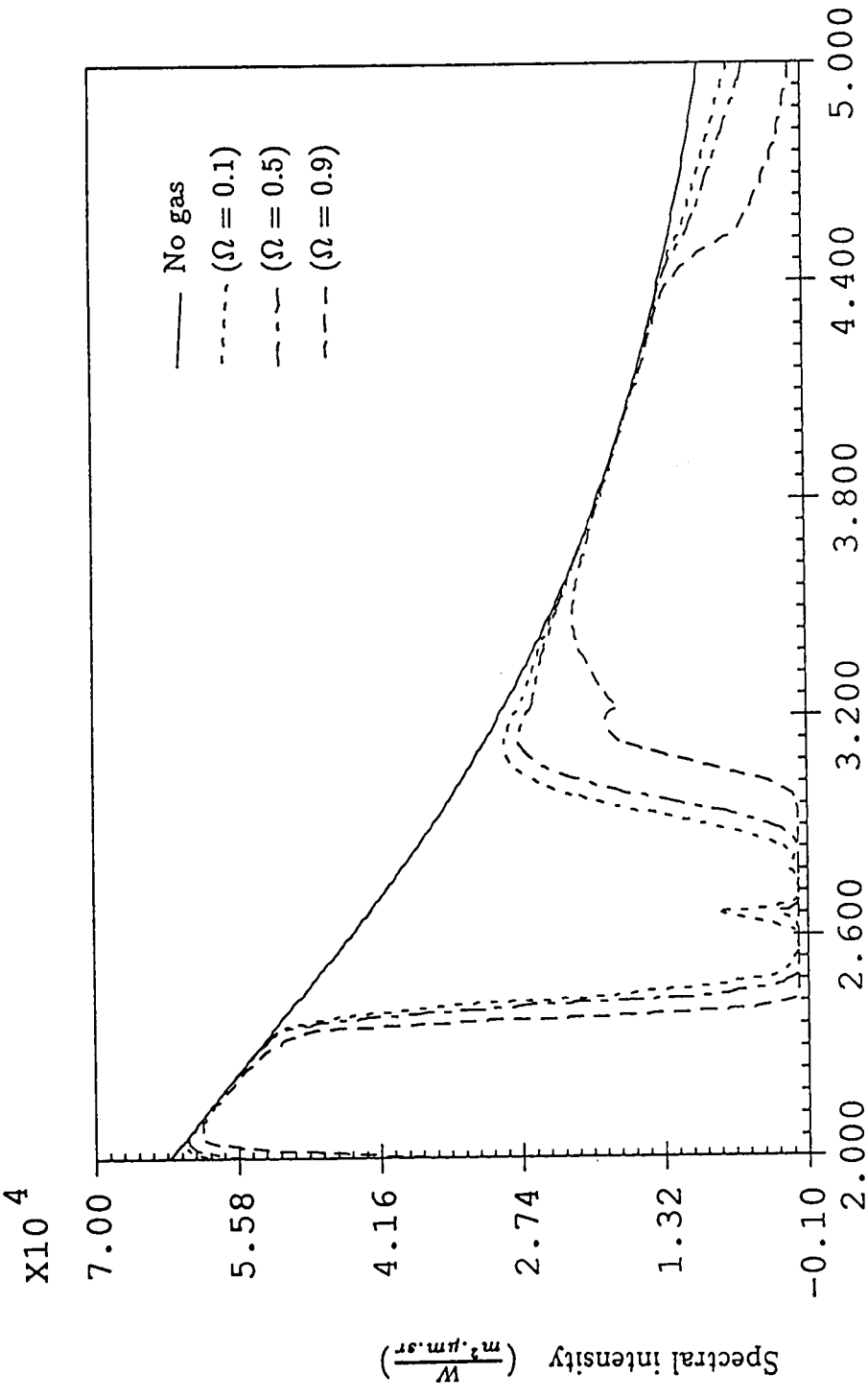
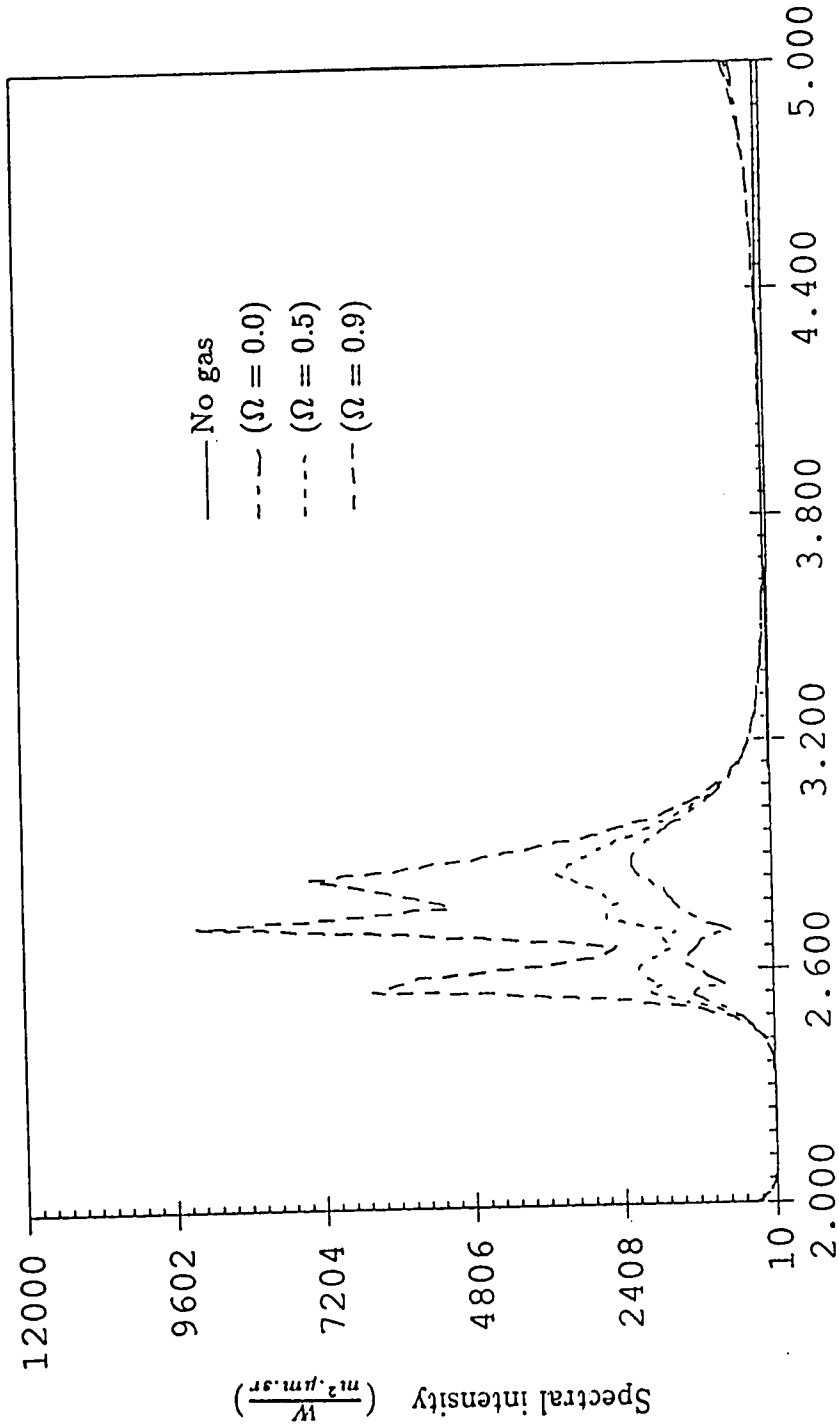


Figure 6.20 Spectral intensity vs. wavelength for hot background plate with cold gas plume.
($T_p = 1755°K$, $T_{max} = 373°K$, $T_{min} = 300°K$, *and* $DP = 10cm$)

media. This important result indicates that at these wavelength ranges, the presence of the plume will not affect the incoming intensity which means the integrated incoming intensity will pass through the plume without being affected. Hence the background radiation can be readily monitored independent of scattering or any other intervention by the plume media.

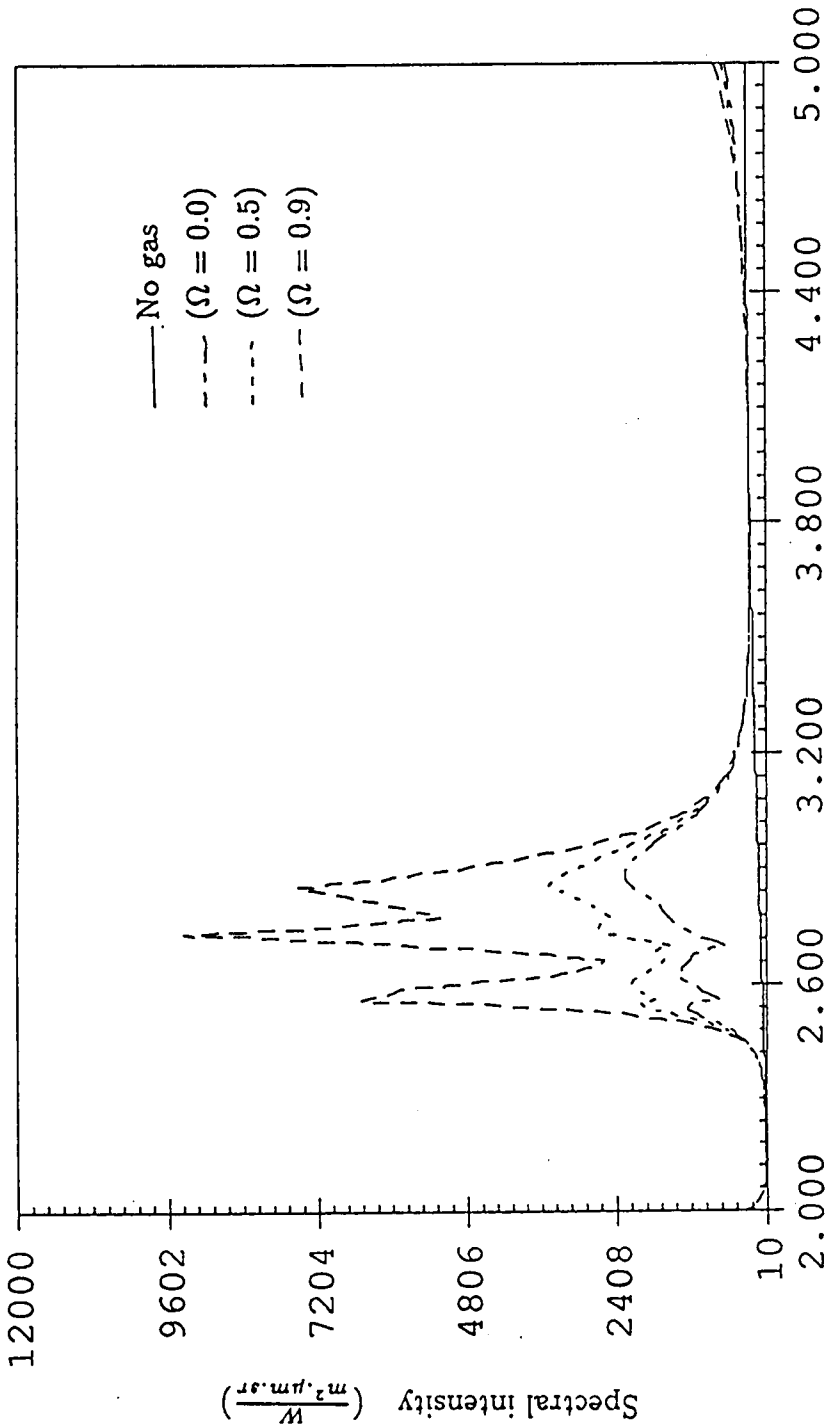
Figures 6.21a - 6.21e are the plots of the directional spectral intensity versus wavelengths at $Y = 0$. These intensity variations are for the case of hot gas at temperature of 1200^oK and are presented for three different fixed values of albedos of 0.0, 0.5, and 0.9. The albedo of 0.0 is for the case when no scattering is present and the participating gas media is effected by absorption and emission only. The extreme case of $\Omega_{0\lambda} = 0.9$ indicates that the media is predominantly a scattering media and albedo of 0.5 is the value between these two extreme cases. The plate temperature is the only variable in these figures. The effects of absorption, emission, and scattering are shown in these figures. Figure 6.21a - 6.21c indicate that the emission from the gas strongly over-powers the absorption effect for $\Omega_{0\lambda}$= 0.0. For albedo values of 0.5 and 0.9, the scattering effect is stronger than the absorption and even the emission effect, specially for $\Omega_{0\lambda}$=0.9. The effect from the increase in temperature of the background radiation becomes more noticeable for $T_p \geq 800^oK$. At plate temperature of 800^oK, the plot for $\Omega_{0\lambda}$=0.0, Figure 6.21d, shows the effect of combination of both absorption and emission. This effect can be seen by intersecting of the intensity variation line with the background intensity line. The portions of the curve under the background intensity line indicates the absorption effect and those above this line indicate the effect of emission. Figure 6.21e shows that for $\Omega_{0\lambda}$=0.0 absorption overcomes the emission in most of the wavelength band and for $\Omega_{0\lambda}$=0.5, the emission is being somewhat effected by combination of absorption and scattering of the media and



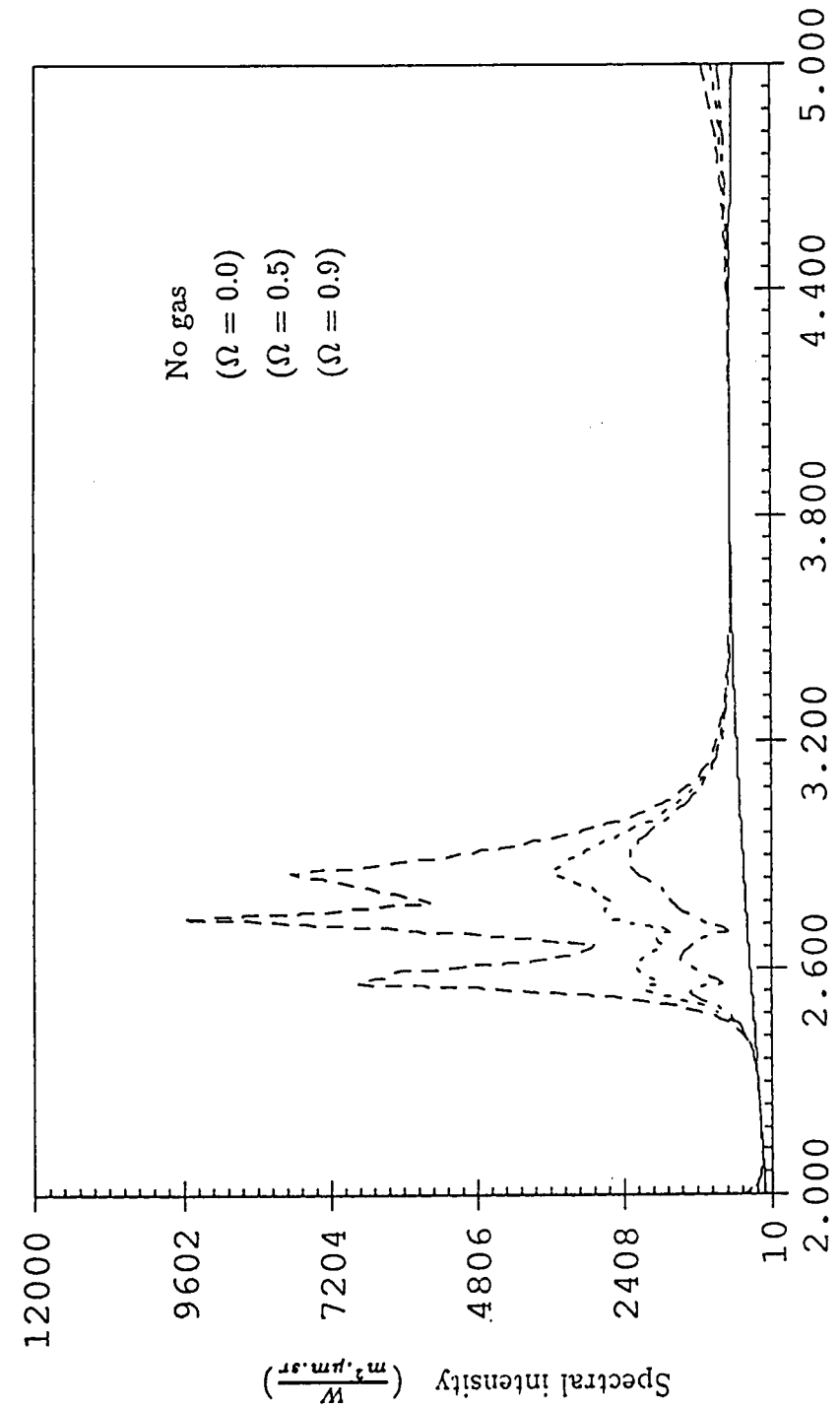
a. $T_p = 500°K$

Figure 6.21 Spectral intensity vs. wavelength at different plate temperatures with hot gas plume.

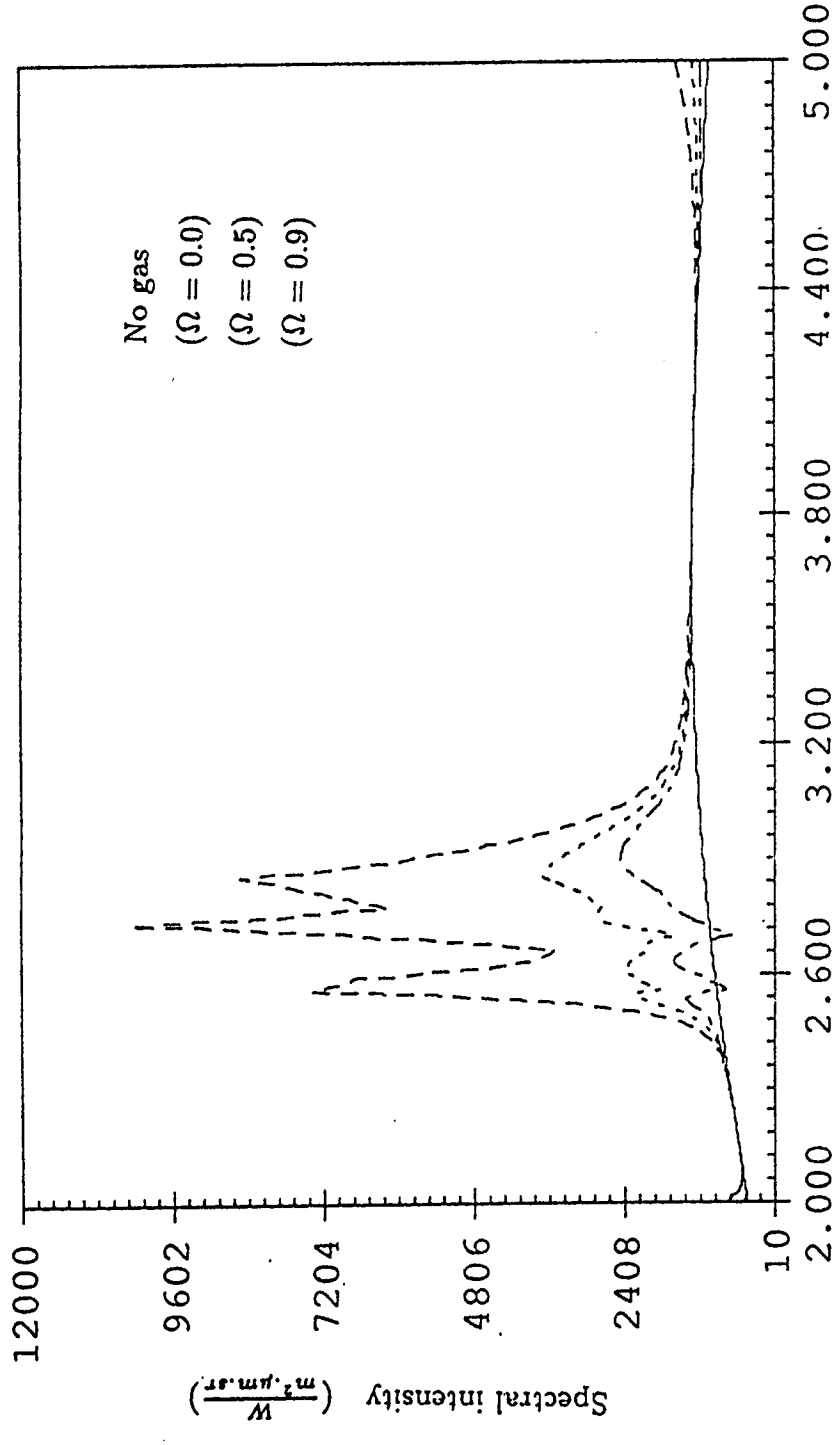
$(T_{max} = 1200°K,\ T_{min} = 300°K,\ and\ DP = 5cm)$


No gas
(Ω = 0.0)
(Ω = 0.5)
(Ω = 0.9)
12000
9602
7204
4806
2408
10
Spectral intensity $(\frac{W}{m^2.\mu m.sr})$
2.000
2.600
3.200
3.800
4.400
5.000
Wavelength (μm)

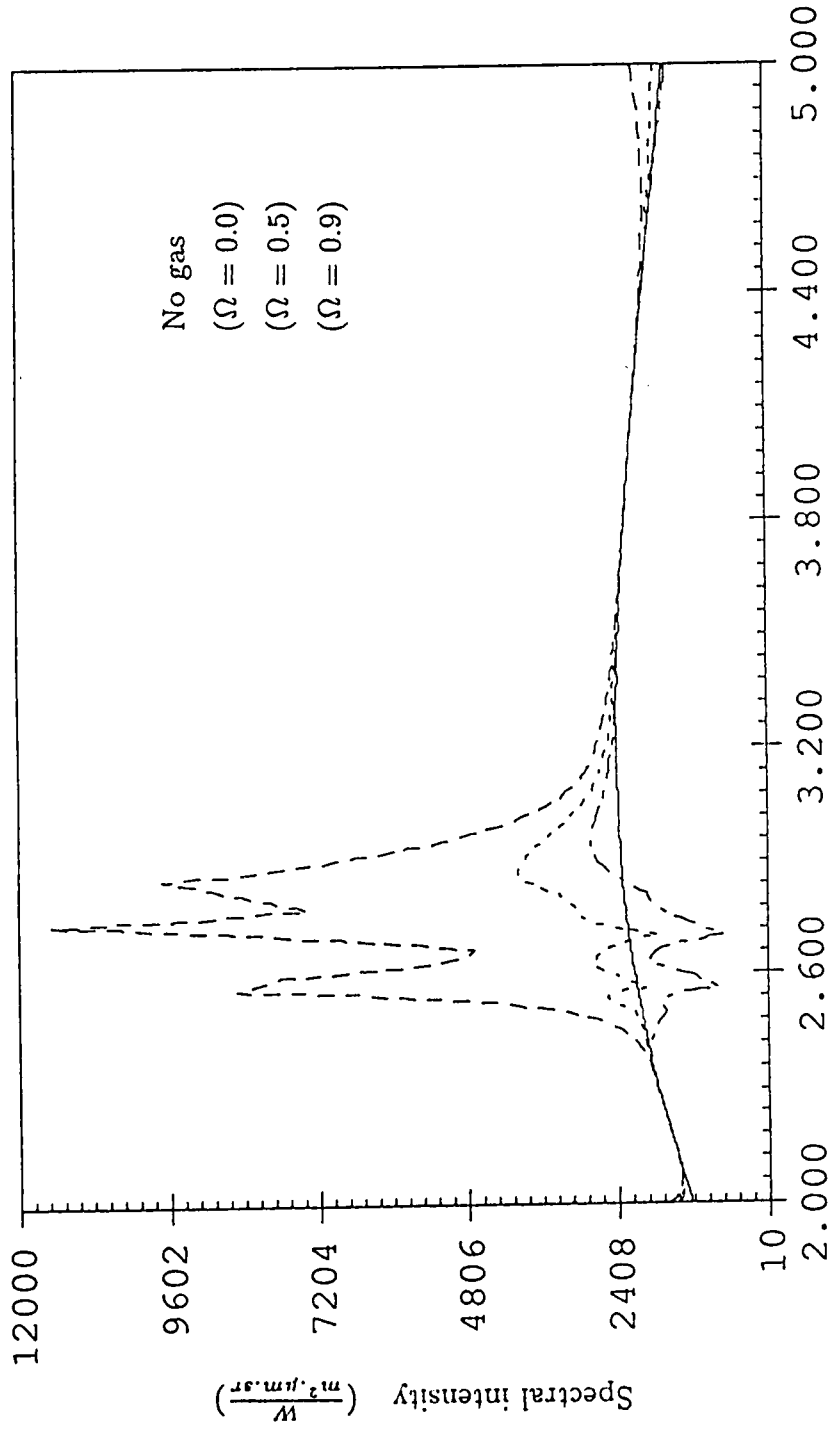
b. $T_p = 600°K$


No gas
(Ω = 0.0)
(Ω = 0.5)
(Ω = 0.9)
12000
9602
7204
4806
2408
10
2.000
2.600
3.200
3.800
4.400
5.000
Spectral intensity (W/m².μm.sr)
Wavelength (μm)

c. $T_p = 700°K$


No gas
($\Omega = 0.0$)
($\Omega = 0.5$)
($\Omega = 0.9$)
12000
9602
7204
4806
2408
10
2.000
2.600
3.200
3.800
4.400
5.000
Spectral intensity $\left(\frac{W}{m^2.\mu m.sr}\right)$
Wavelength (μm)

d. $T_p = 800°K$


No gas
($\Omega = 0.0$)
($\Omega = 0.5$)
($\Omega = 0.9$)
12000
9602
7204
4806
2408
10
2.000
2.600
3.200
3.800
4.400
5.000
Spectral intensity $(\frac{W}{m^2.\mu m.sr})$
Wavelength (μm)

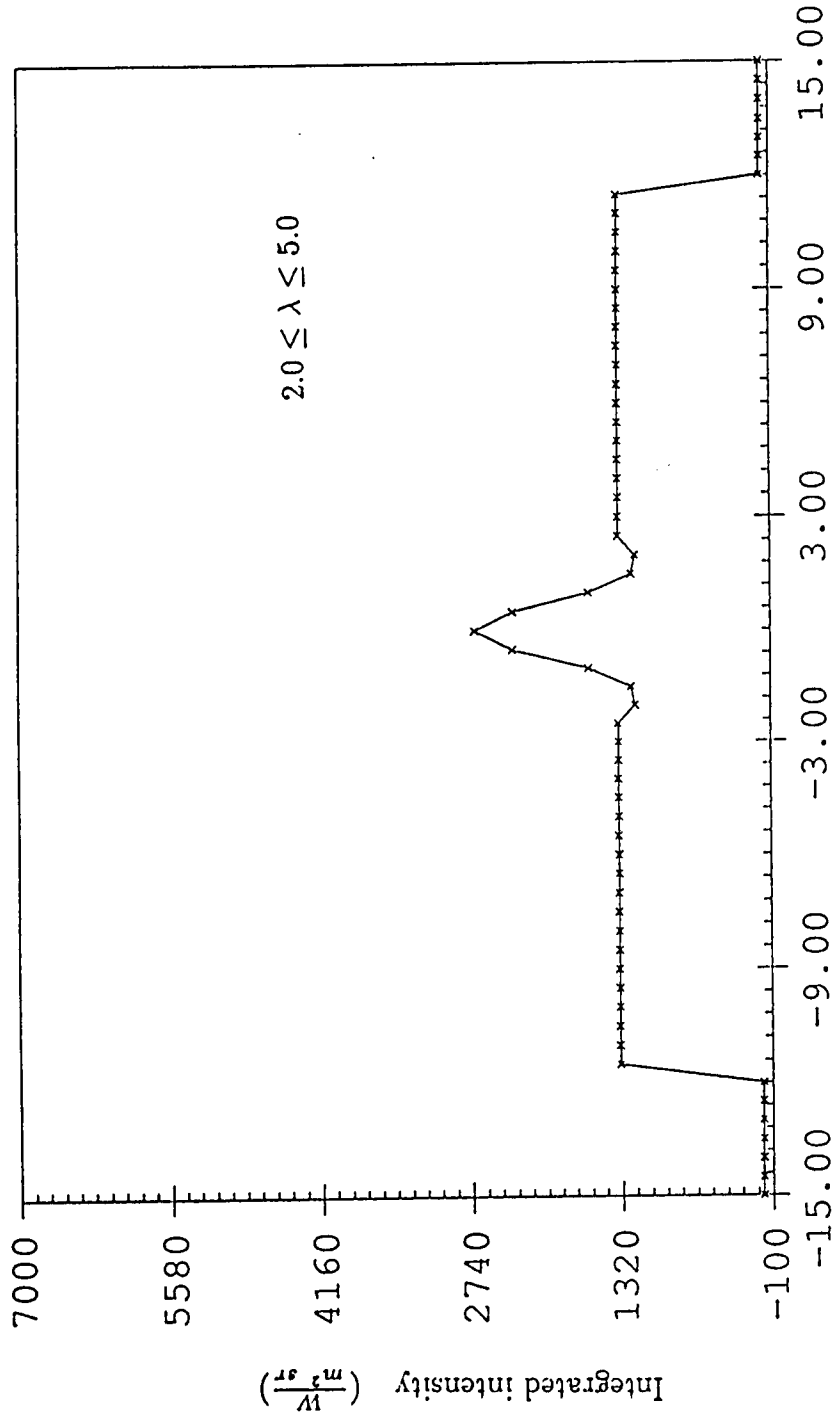
e. $T_p = 900°K$

for $\Omega_{0\lambda}$=0.9, the effect of scattering is strongly visible over the absorption and emission.

The effect of absorption, emission, and scattering of the gas media over the integrated intensity across the plume cross section at $(Y = 0)$ are shown in Figures 6.22. These figures have been plotted for a fixed radiation source temperature of $700^{o}K$ and gas temperature of $1200^{o}K$. The albedo will be the only variable for these figures which cover the range of 0.2 to 0.9. These plate temperatures are similar to those in Figures 6.14.

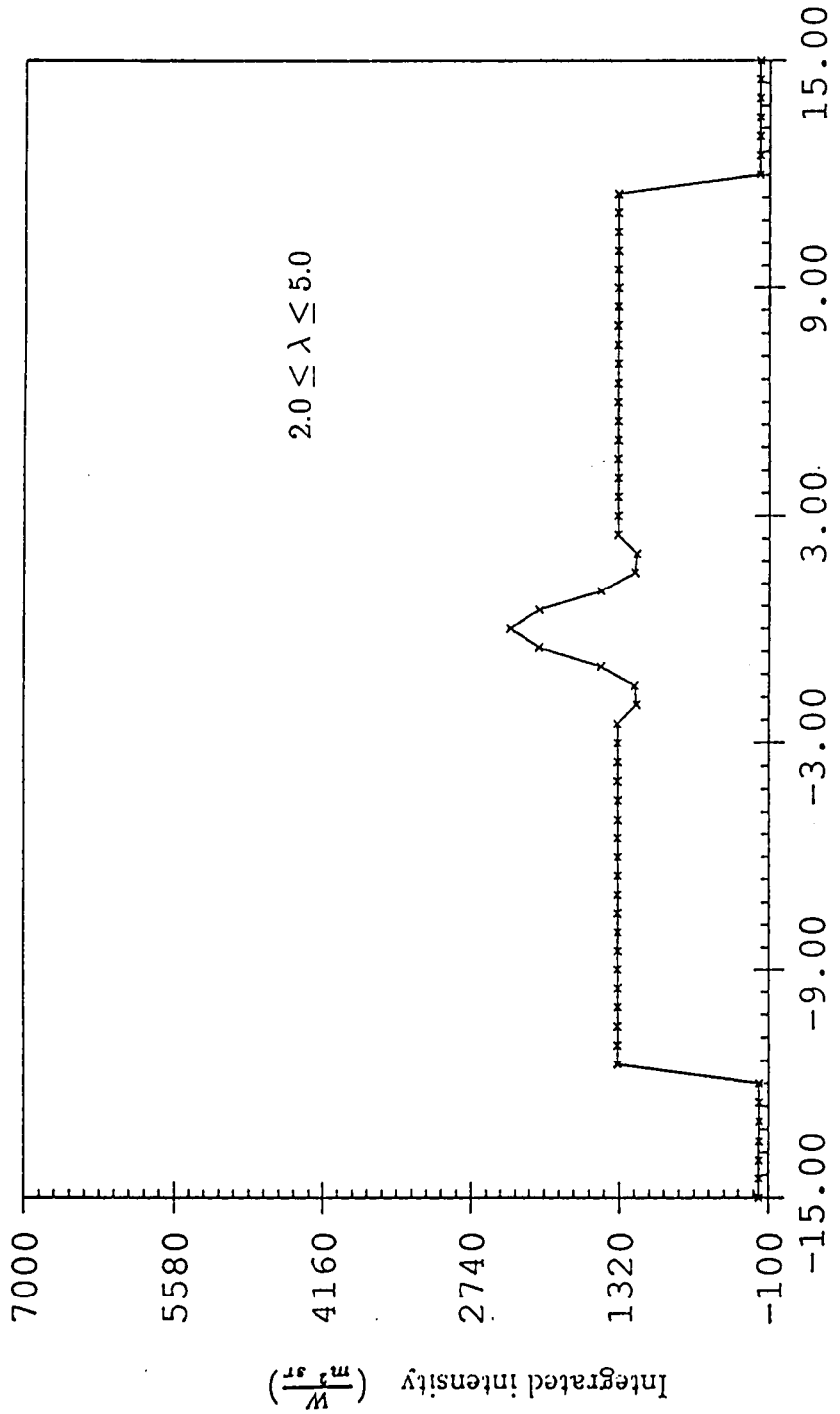
Figures 6.22d and 6.22e show that for large values of albedo ($\Omega_{0\lambda} \geq 0.8$) the scattering effect dominates emission effect. Increasing $\Omega_{0\lambda}$ will decrease the peak value of the emission at 2.7 μ. Figure 6.22e ($\Omega_{0\lambda}$=0.9) shows that the peak value of the emission no longer exists. From a different point of view, it can be expressed that the effect of scattering for this case is similar to the effect of absorption with the difference that the incoming energy has been scattered rather than absorbed.

It can be seen from Figures 6.23 that for a hotter background radiation source, the effects are somewhat different from the results shown in Figure 6.22. In Figures 6.23a and 6.23b, it is recognized that even at low values of $\Omega_{0\lambda}$ the effect of scattering and absorption on the emission are significant from the hot gas. These effects are more pronounced in Figures 6.23d and 6.23e. These figures show that for $\Omega_{0\lambda}$ =0.8, 0.9, the scattering effect is strong enough to overcome emission, totally. This can be easily distinguished in Figure 6.23e.

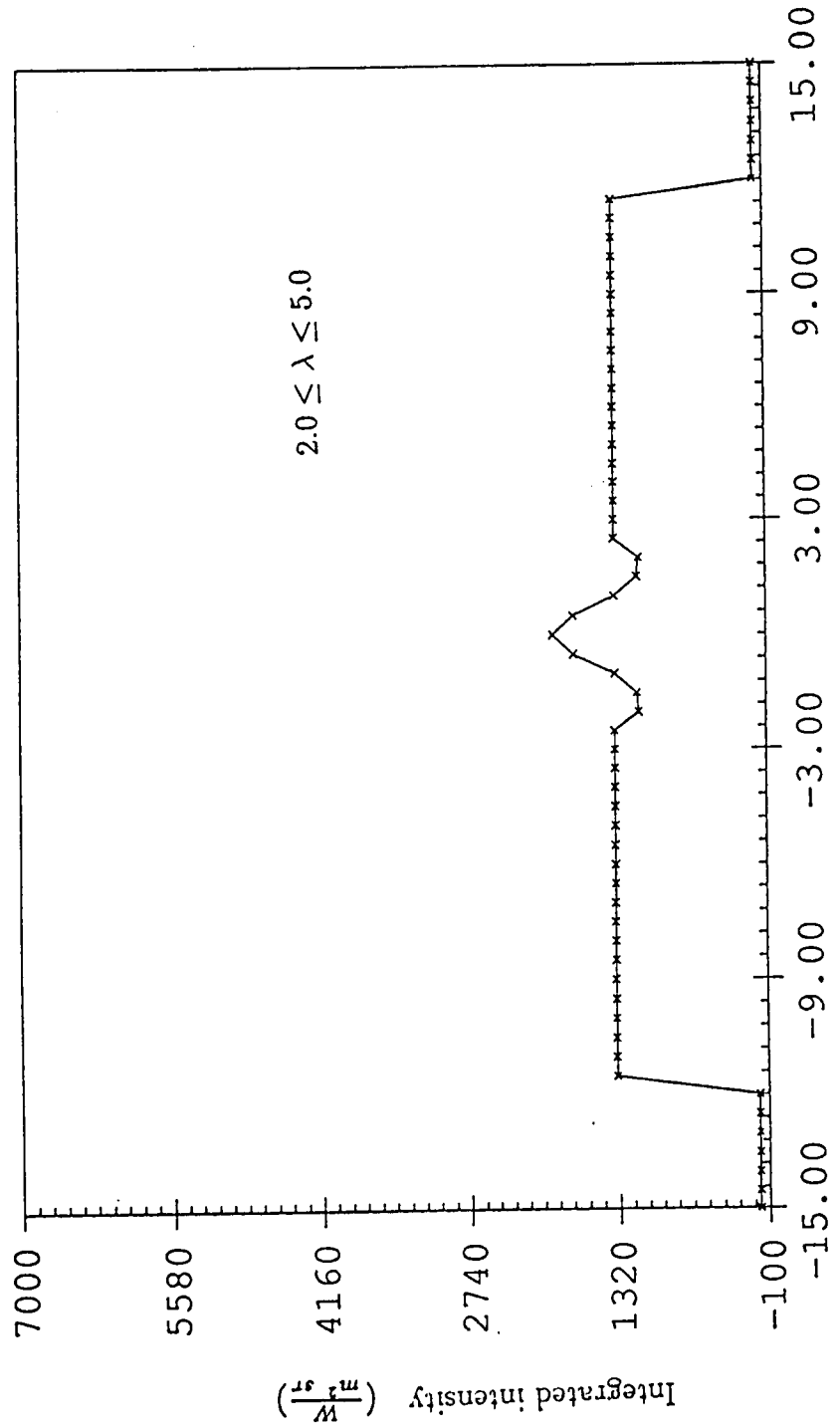


a. $\Omega = 0.2$

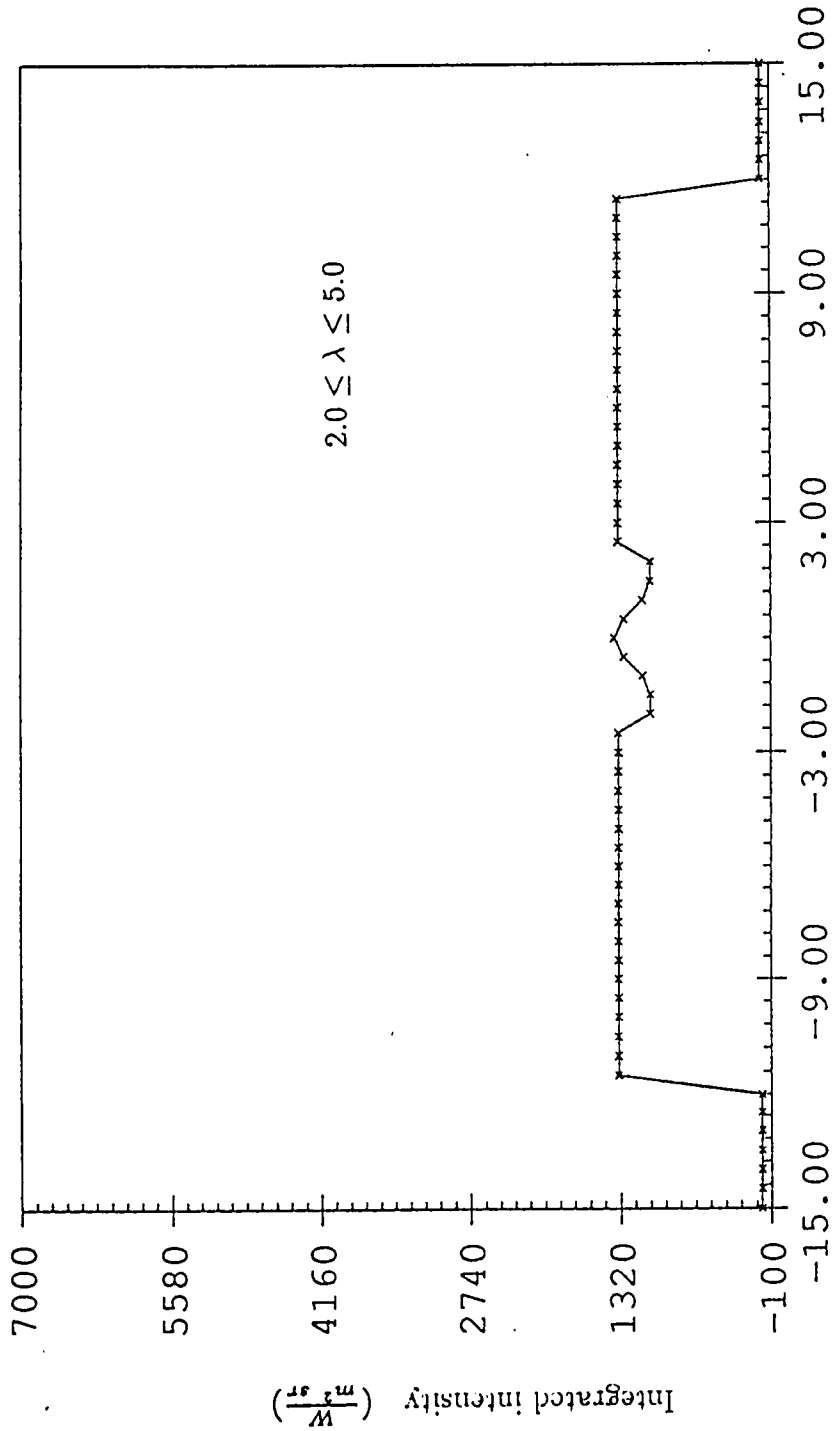
Figure 6.22 Integrated intensity vs. Y at different albedos.
($T_p = 700°K$, $T_{max} = 1200°K$, $T_{min} = 300°K$, *and* $DP = 5\ cm$)


7000
5580
4160
2740
1320
-100
-15.00
-9.00
-3.00
3.00
9.00
15.00
$2.0 \leq \lambda \leq 5.0$
Integrated intensity $\left(\frac{W}{m^2\,sr}\right)$
Y (cm)

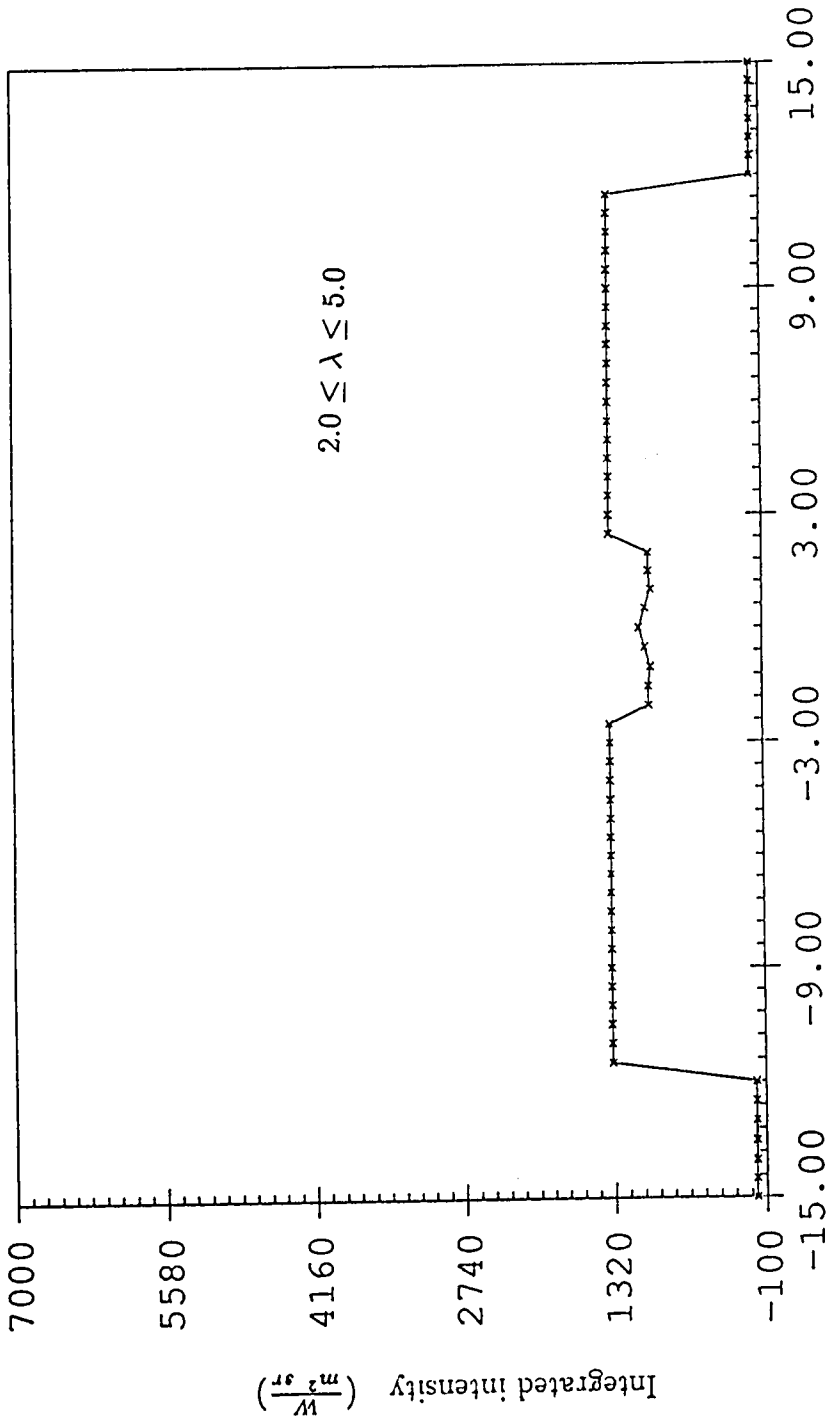
b. $\Omega = 0.4$


$2.0 \leq \lambda \leq 5.0$
Integrated intensity $\left(\frac{W}{m^2\ sr}\right)$
7000
5580
4160
2740
1320
-100
-15.00
-9.00
-3.00
3.00
9.00
15.00
Y (cm)

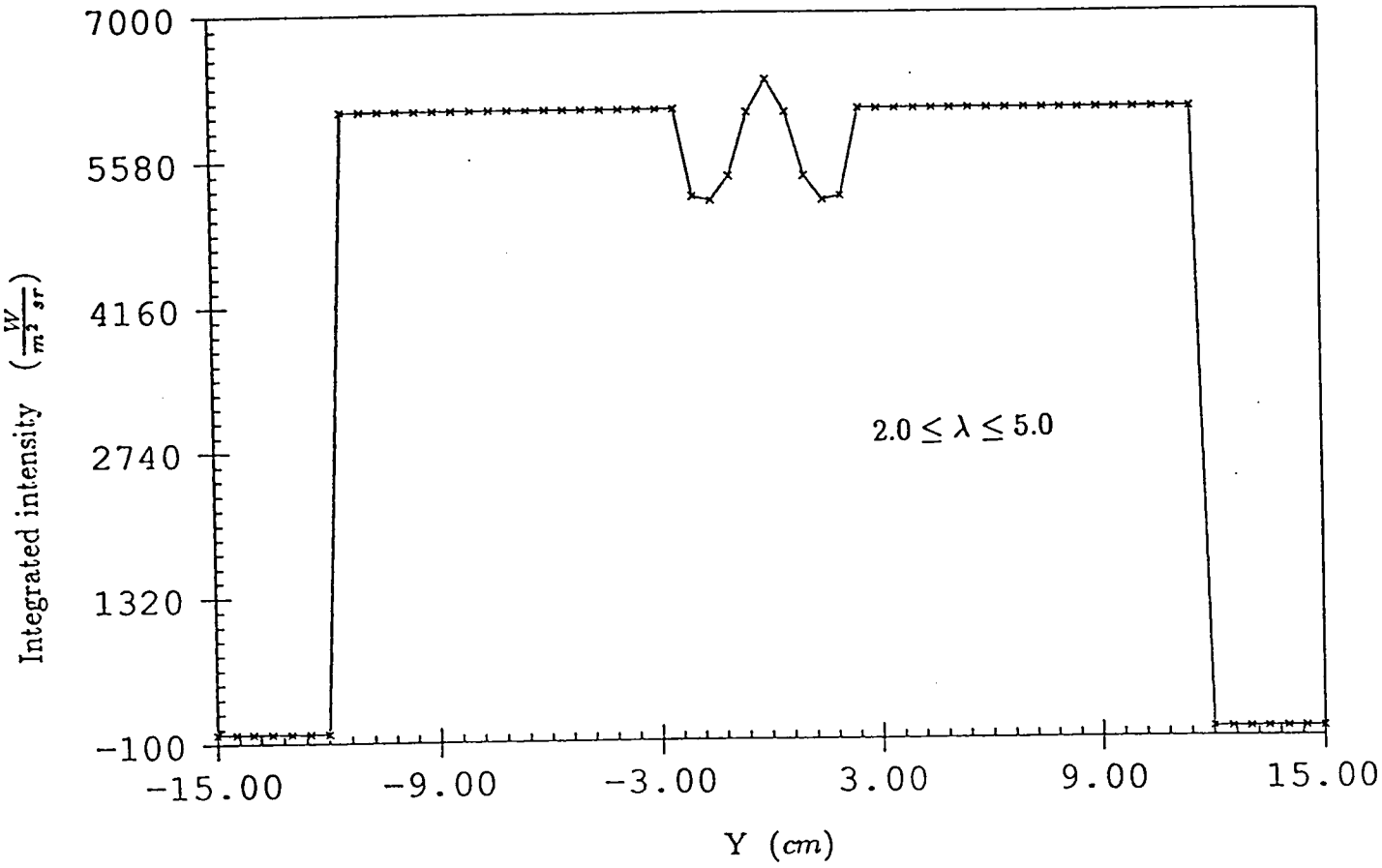
c. $\Omega = 0.6$


7000
5580
4160
2740
1320
-100
-15.00
-9.00
-3.00
3.00
9.00
15.00
Y (cm)
Integrated intensity $(\frac{W}{m^2 sr})$
$2.0 \leq \lambda \leq 5.0$

d. $\Omega = 0.8$

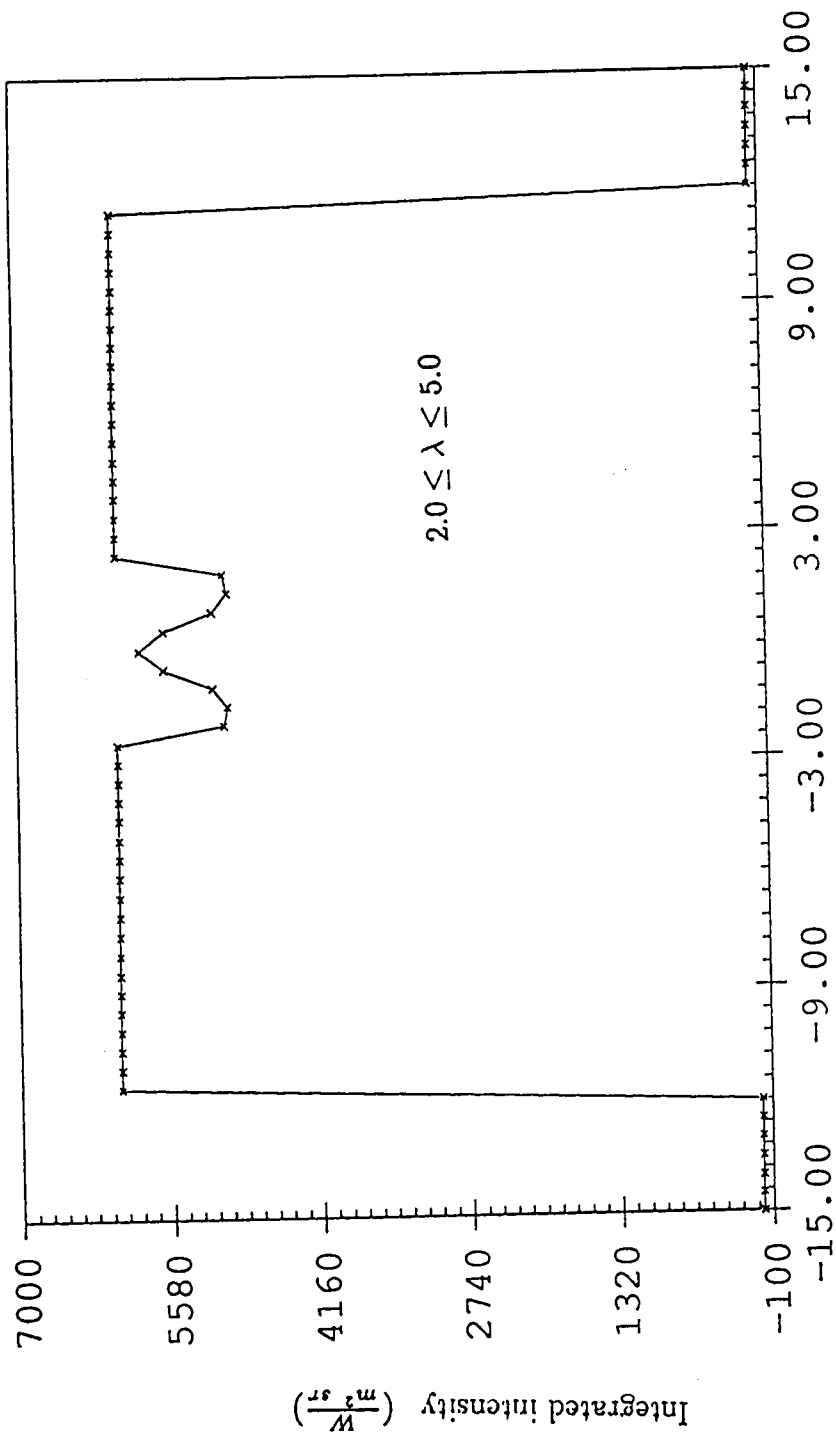

7000
5580
4160
2740
1320
-100
-15.00
-9.00
-3.00
3.00
9.00
15.00
Y (cm)
Integrated intensity $(\frac{W}{m^2\ sr})$
$2.0 \leq \lambda \leq 5.0$

e. $\Omega = 0.9$

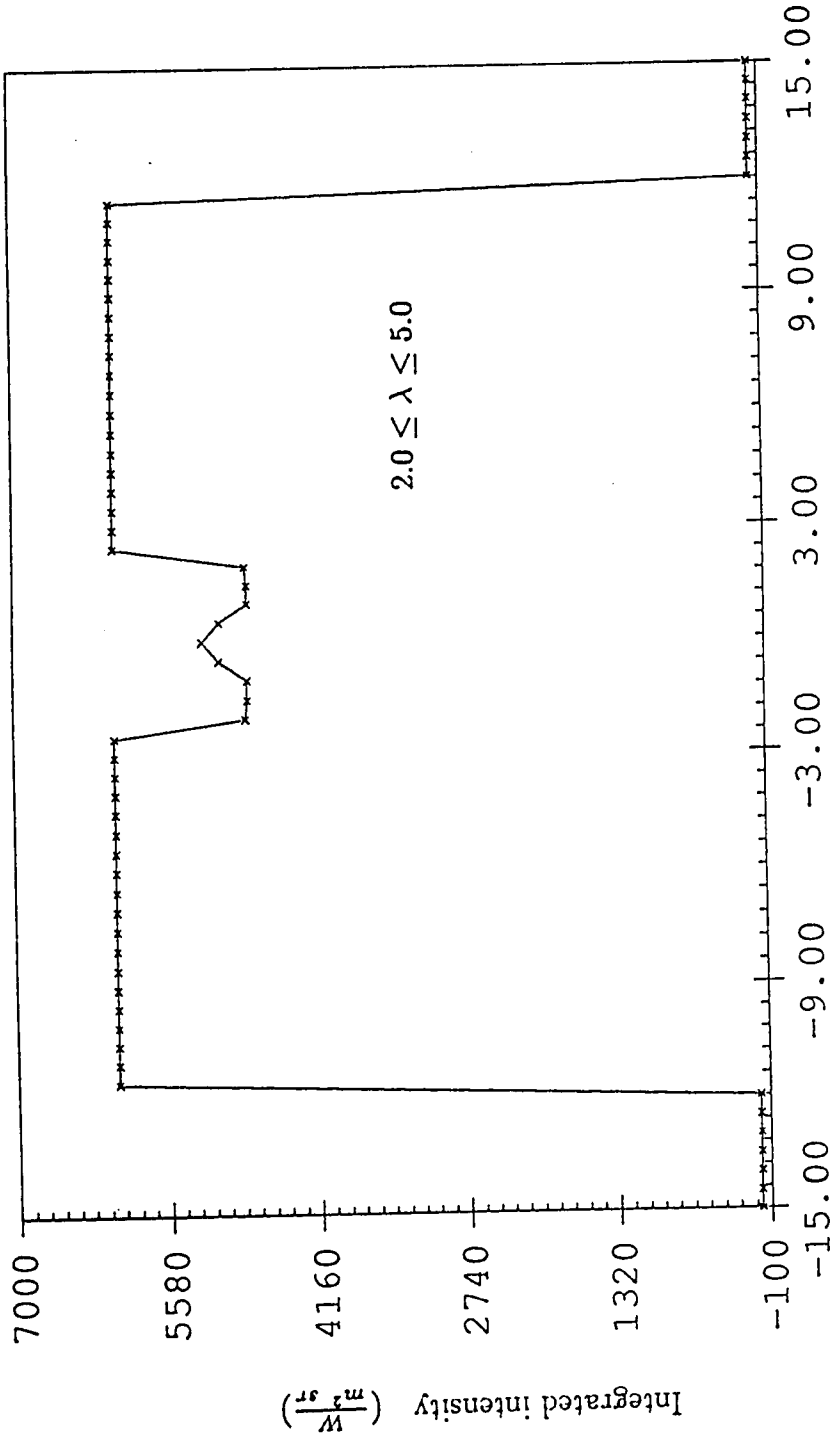


a. $\Omega = 0.2$

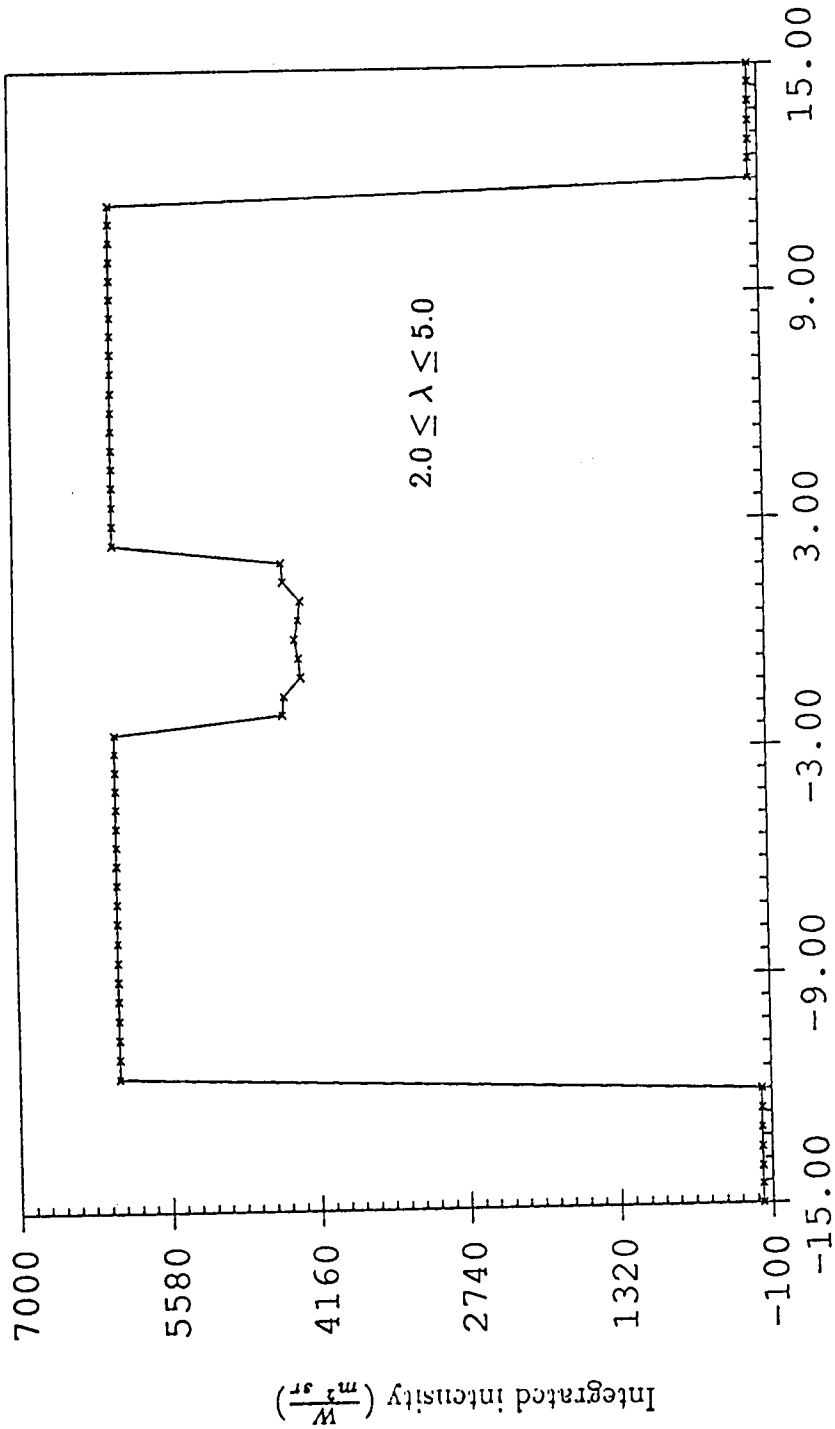
Figure 6.23 Integrated intensity vs. Y at different albedos.
($T_p = 900°K$, $T_{max} = 1200°K$, $T_{min} = 300°K$, *and* $DP = 5\ cm$)


Integrated intensity $(\frac{W}{m^2 sr})$
7000
5580
4160
2740
1320
-100
-15.00
-9.00
-3.00
3.00
9.00
15.00
Y (cm)
$2.0 \leq \lambda \leq 5.0$

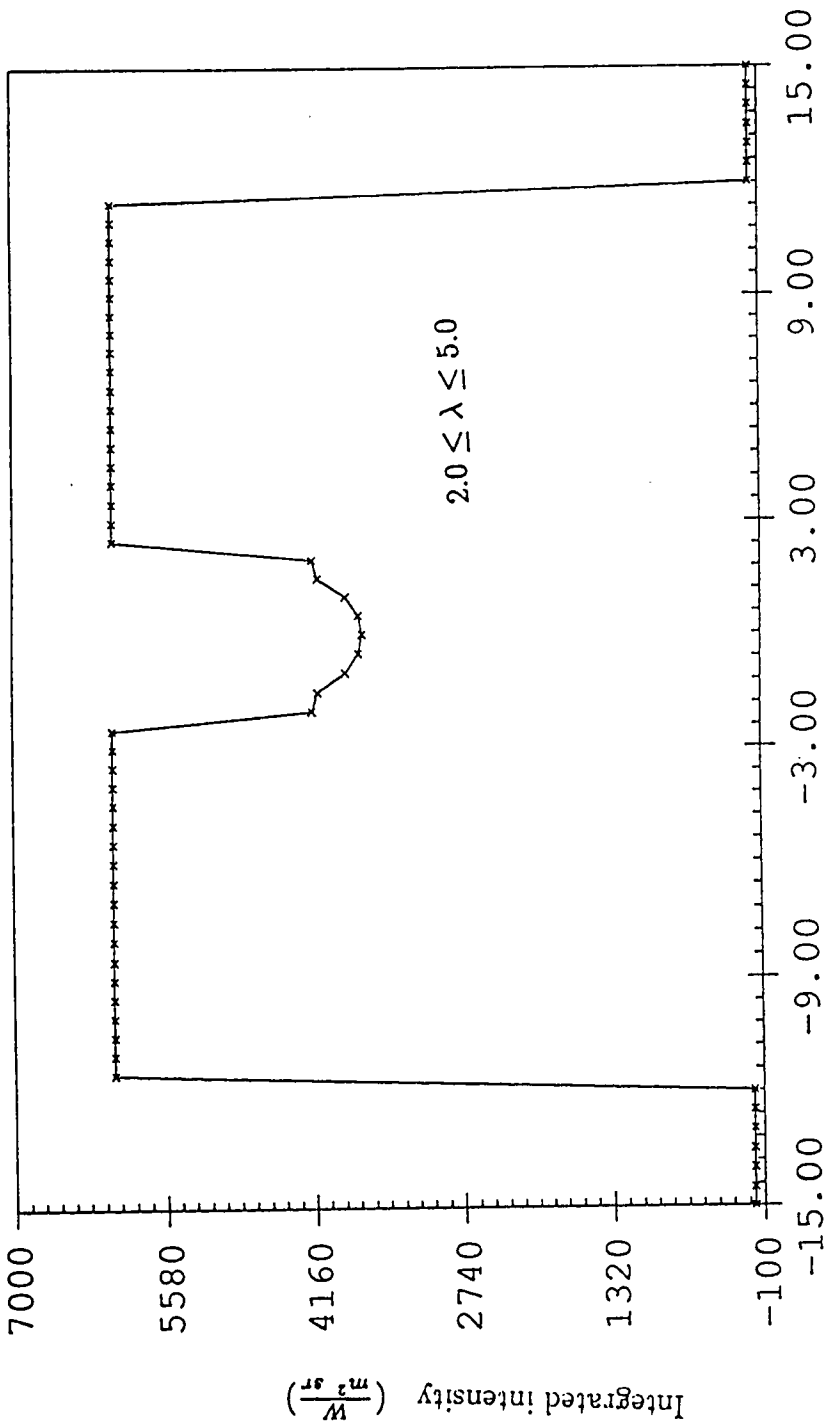
b. $\Omega = 0.4$


7000
5580
4160
2740
1320
-100
-15.00
-9.00
-3.00
3.00
9.00
15.00
Y (cm)
Integrated intensity $(\frac{W}{m^2\ sr})$
$2.0 \leq \lambda \leq 5.0$

c. $\Omega = 0.6$


7000
5580
4160
2740
1320
-100
-15.00
-9.00
-3.00
3.00
9.00
15.00
Y (cm)
Integrated intensity ($\frac{W}{m^2 sr}$)
$2.0 \leq \lambda \leq 5.0$

d. $\Omega = 0.8$


7000
5580
4160
2740
1320
-100
-15.00
-9.00
-3.00
3.00
9.00
15.00
Y (cm)
Integrated intensity $\left(\frac{W}{m^2\,sr}\right)$
$2.0 \leq \lambda \leq 5.0$

e. $\Omega = 0.9$

CHAPTER VII

EXPERIMENTAL SYSTEM

The feasibility of the infrared detection scheme was evaluated on subscale simulated laboratory plumes to determine sensitivity, signal to noise ratio, and general suitability of IR imaging system for liquid rocket engine propellant path leak detection. The experimental analysis was undertaken with the objective of testing simple models to differentiate the amount of radiation coming from a radiation source passing through an absorbing, emitting and scattering medium. The feasibility experiments were completed using the Thermovision® system to obtain images of both hot and cold plumes in front of a warm background plate.

The subscale laboratory experimental set-up shown in Figure 7.1 is composed of a hot plate, an atomizer, and the Thermovision® system. Thermovision® is a trade name for real-time infrared imaging system. In the present investigation, Thermovision® 870 has been used. Thermovision® 870 represents a state-of-the-art infrared system with a thermoelectrically cooled detector element. This system consists of an infrared scanner, display unit, power source converter, standard video cassette recorder (VCR), and a standard television.

7.1 Thermovision® System

The scanner is connected to the display unit via a single interconnecting cable. The cable terminates in a plug which is connected to the scanner socket at the rear of the display unit. Thermovision® 870 power requirement is $\pm$ 15 V dc for the display unit and the scanner. A power source converter is used to convert the wall output (110 V) to the required $\pm$ 15 V dc. The Display Unit is connected to a VCR and a standard television by a similar connections. These interconnections

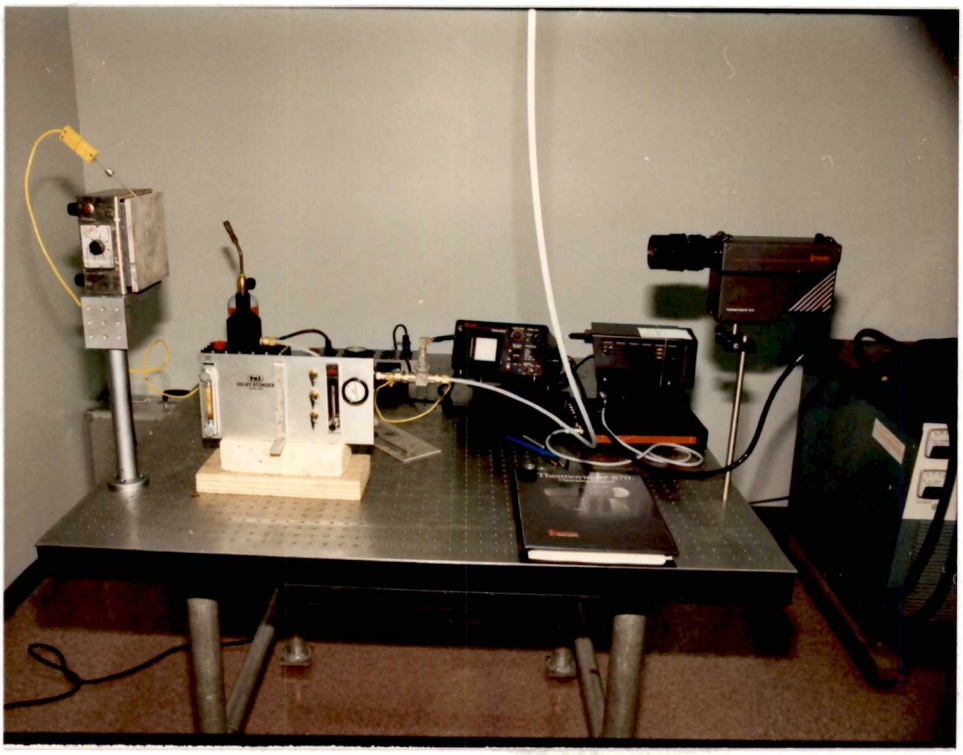


Figure 7.1 Experimental Arrangement

are shown in figure (7.2).

In the following section the individual components of the experimental set up will be briefly explained.

7.1.1 The Scanner Unit

The infrared scanner unit converts electromagnetic thermal energy radiation from an object into electronic video signals. These signals are amplified and transmitted via an interconnecting cable to a display monitor where the signals are further amplified and the resultant image is display on the display screen.

The scanner unit comprises the following:

(a) Electro-optical scanning mechanism

(b) Infrared detector

(c) Video interface

(d) Control electronics and microprocessor for data output

Electromagnetic energy radiating from the object being scanned is focused by an infrared lens into a mirror. The mirror is oscillated by a dc motor. The optical output from the oscillating mirror is focused by three fixed mirrors onto a horizontal mirror polygon which rotates at 16000 rpm. Both the oscillating mirror and the horizontal mirror polygon are controlled by the microprocessor. The microprocessor provides horizontal and vertical trigger pulses to the display unit trigger circuits.

The oscillating mirror and horizontal motors are synchronized in such a way that four fields produce one interlaced frame, each having 100 horizontal scanning lines. Of these, 70 are used as active imaging lines per field, or 280 per frame. With a scanning rate of 25 fields per second, 25/4 completely interlaced picture frames per second are thus produced.

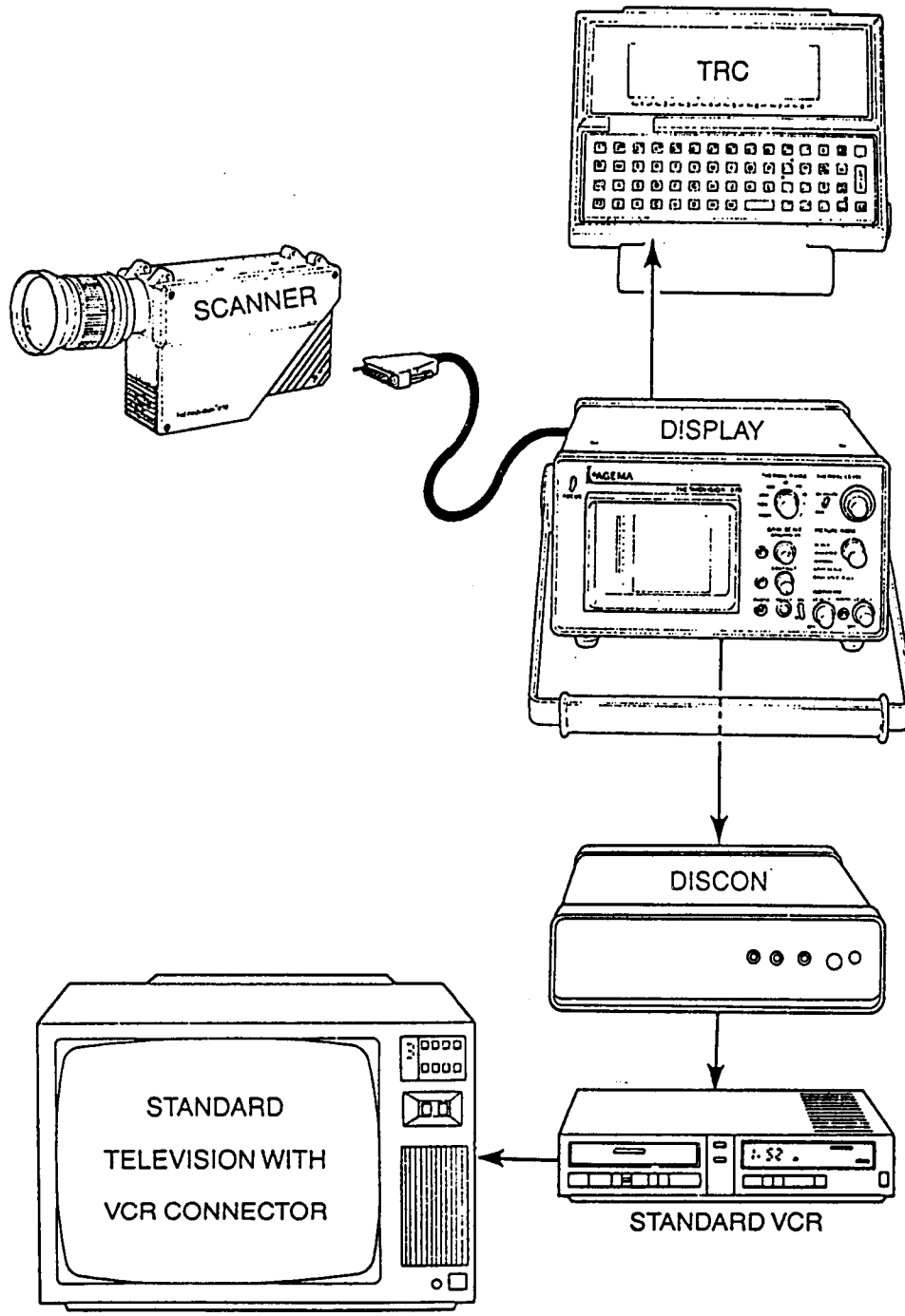


Figure 7.2 Connection of the Thermovision 870 system

The reflected beam from the horizontal mirror polygon is passed through a set of relay optics containing a selectable aperture unit and a filter unit and finally focused onto a point detector (see figure 7.3).

7.1.2 Detector

The detector is entitled SPRITE- Signal PRocessing In The Element. Essentially the detector is a strip of infrared sensitive material (mercury cadmium telluride) mounted on a sapphire substrate.

If a small region of the detector chip is exposed to infrared radiation, excess current carriers are generated in the region. The excess current carriers 'drift' towards the readout region matched at the same velocity as the image which is scanned along the strip. Therefore, the excess carriers are fed along the strip together with the infrared image, resulting in all the carriers arriving at the readout at the same time. The result is an improvement in signal/noise ratio obtained by an internal integration function from the detector itself. The SPRITE detector operates at a temperature of -70 ^{o}C. This is achieved by using a 3-stage thermoelectric cooler incorporated into the encapsulators. This single element SPRITE detector is sensitive to radiation between 2 and 5 μm.

7.1.3 The Interchangeable Lenses

Lenses are fitted to the scanner unit in the same manner as photographic lenses with bayonet fitting. All lenses are anti-reflective coated, therefore, all the incoming radiation energy are transmitted through the lenses without being reflected.

The scanner unit of Thermovision® 870 can be fitted with any one of four different standard lenses with field of view varying from 7° to 40°. The standard 20° lens is used for the present investigation.

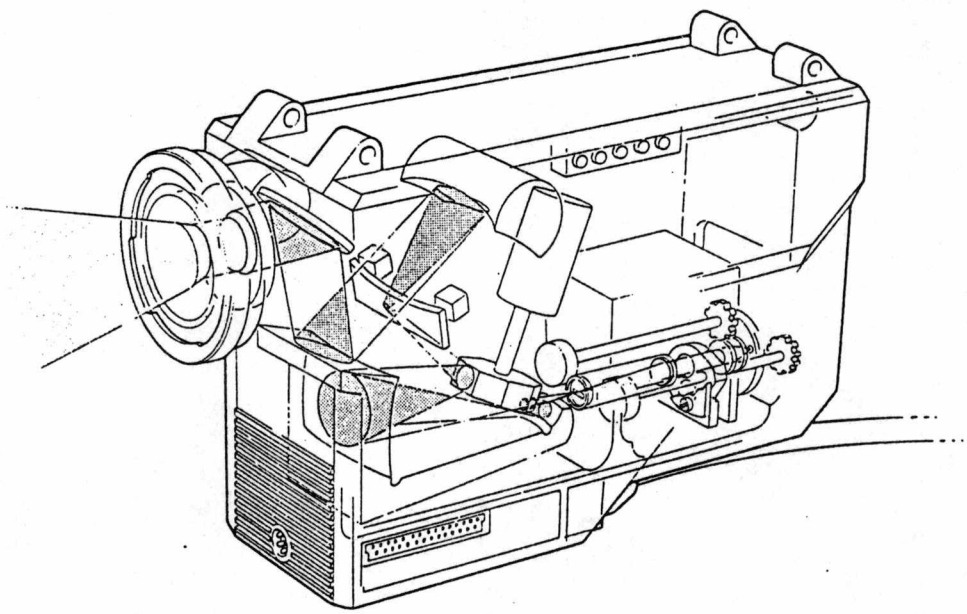


Figure 7.3 Cutaway view of Thermovision scanner

7.1.4 Object Field Data

Table 7.1 and figure 7.4 give the dimensions of the scanned field surrounding the object at a set distance d, and using the four different lenses. The table also detail the depth of focus within which a sharp picture of the object may be obtained. All measurements are in meters.

7.1.5 Aperture Selection

The aperture control, located at the back of the scanner assembly, is an aperture turret which has positions for three apertures, marked 0, 1, and 2. The apertures are selected so that the object temperature covering the range -20^{o}C to +500^{o}C can be measured. The smaller the aperture, the higher the temperatures that can be viewed.

7.1.6 The Display Unit

The display unit houses all the operational controls for the Thermovision® 870 system, see Figure 7.5. Some of the controls and their functions can be described as:

1. Gray Scale Brightness — This manual control increases or decreases the display brightness.
2. Gray Scale Contrast — This manual control increases or decreases the display contrast.
3. Thermal Range — This nine position switch selects the thermal range of the object being viewed. The switch is calibrated between 2 and 1000 isotherm units.
4. Thermal level — This control adjusts the zero thermal level (as seen on the

Table 7.1 Scanned field (W) and depth of focus (+) set at various distances (d)

Lens	d	0.3	0.5	0.8	1.2	2	3	5	10
7° × 7°	w				0.13	0.22	0.34	0.59	1.2
	+				0.04	0.12	0.30	1.2	4.6
	–				0.04	0.11	0.25	0.7	2.4
12° × 12°	w			0.13	0.23	0.42	0.65	1.1	2.1
	+			0.05	0.13	0.41	0.83	4.2	∞
	–			0.04	0.10	0.29	0.62	1.6	4.7
20° × 20°	w		0.13	0.22	0.37	0.68	1.0	1.7	3.5
	+		0.05	0.16	0.45	1.9	12.1	∞	∞
	–		0.04	0.11	0.25	0.6	1.3	2.8	7.1
40° × 40°	w	0.17	0.34	0.59	0.82	1.6	2.4	4.0	8.2
	+	0.05	0.29	1.9	∞	∞	∞	∞	∞
	–	0.03	0.12	0.3	0.6	1.3	2.2	4.1	9.0

NOTE: All measurements are in metres.

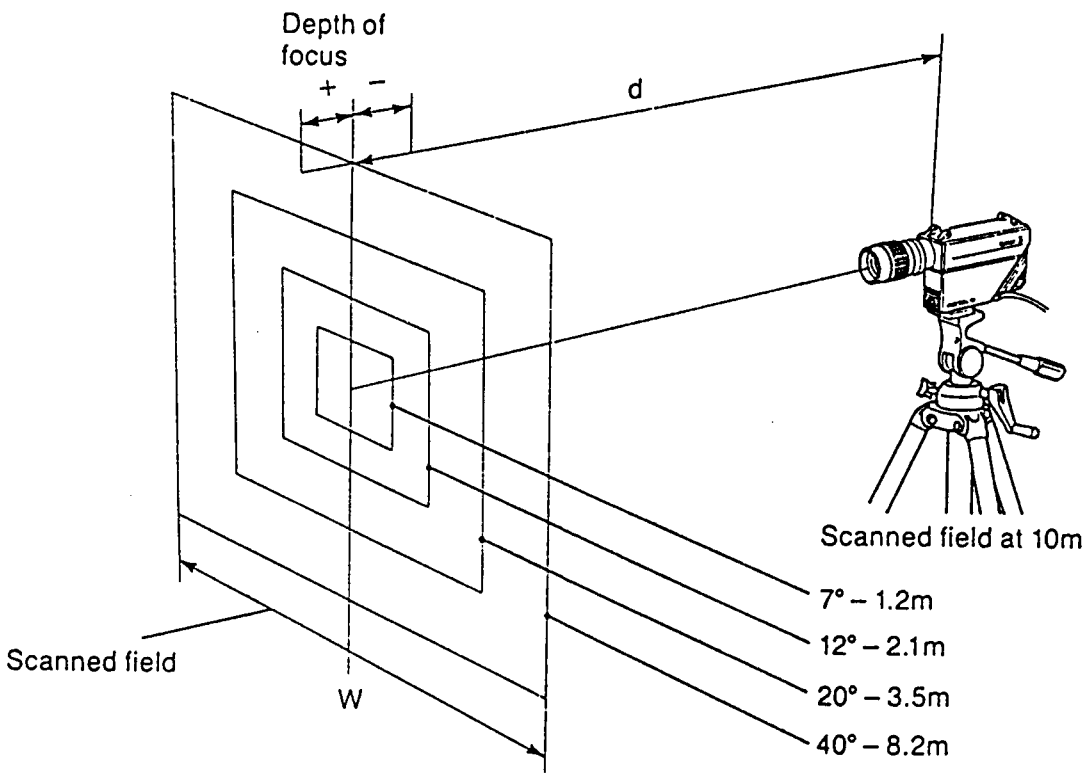


Figure 7.4 Dimensions of scanned surfaces with various lenses

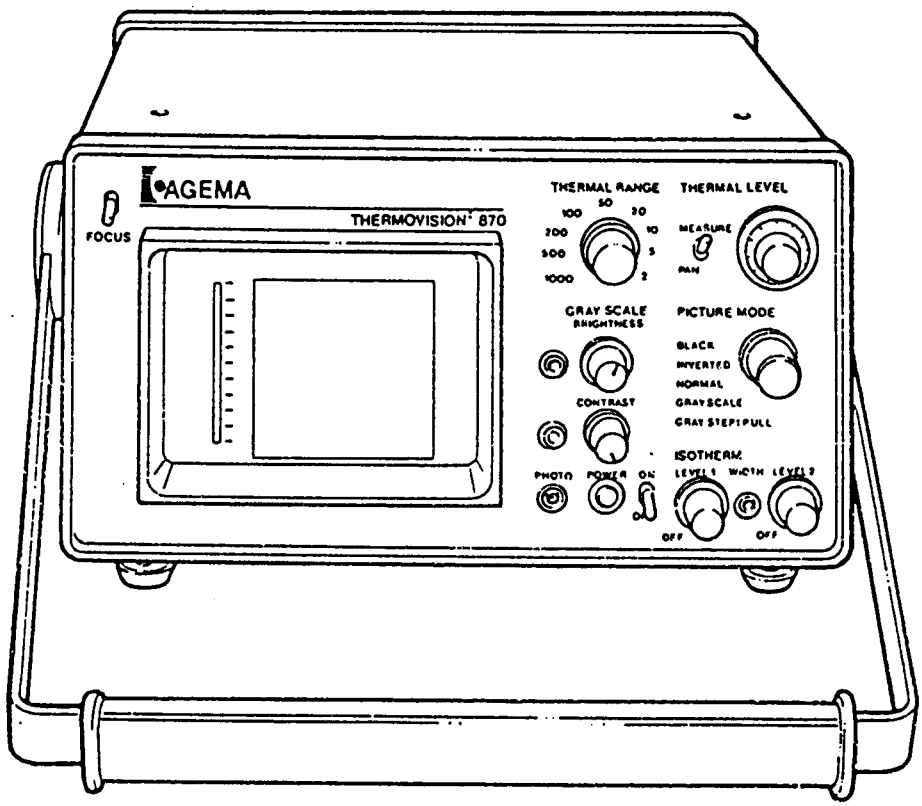


Figure 7.5 Display unit.

vertical scale) of the thermal image.

5. Picture Mode — This switch selects the type of image to be displayed.
6. Gray Scale — This position causes a continuous gray scale to be displayed on the screen.
7. Normal — This position selects a normal thermal image display, where the hotter object temperatures appear as white and the cooler as black.
8. Inverted — This position is used to invert the display representation, i.e. warm = black, and cool = white.
9. Black — This position causes only isotherm levels to be displayed while suppressing the gray tone image (used in conjunction with the Isothermal Level and Width control.
10. Isotherm Level (1) — This control is used to turn one of the two isotherm functions ON and to adjust for identification of discrete thermal levels on the object (shown as saturated white).
11. Isotherm Level (2) — See Isotherm Level (1)
12. Isotherm Width — This control sets the width of the 2 isotherm markers, displayed on the vertical scale.

7.1.7 Video Cassette Recording (VCR)

A standard VCR can be connected to Thermovision® 870, but the scanning and interlacing system have to be modified by utilizing a specially developed converter called DISCON (Digital Infrared System for Coloration).

Using this system the recorded image together with the recorded Thermal Level, Thermal Range, and Isotherm setting can be played back in black and white using a standard television set. The image is presented in real time but can be adapted to a frozen image by utilizing the FREEZE function on the DISCON unit.

This is advantageous when studying an image in more detail or for photographic recording.

7.1.8 Computer Systems

Thermographic images contain much information which is not always perceptible to the human eye. By using a computerized image reduction or by subtracting one image from another it is possible to enhance the differences. Using a computer, results are obtained quicker and usually with more accuracy. There are two methods available for computer analysis of images that can be used with Thermovision®.

7.1.8.1 Thermal Image Computer System TIC

This system operates in conjunction with an IBM PC. The UTSI image processing division has developed the interface and software which enables image analysis in colors to be carried out on-line and in real time, using Thermovision®. Thermal range and level setting are transferred automatically from the Thermovision® 870 display unit to the computer and from computer to the VCR and television screen. This system includes a camera which enable the frozen image to be photographed from VICOM, digital image processing system.

7.1.8.2 Temperature Readout Computer TRC

Thermovision® 870 can also be operated on line with a temperature readout computer, which is a portable computer and is loaded with a special software program developed for it. This ensures that it is possible to display immediately on the computer screen both the temperature or the emissivites which correspond to the two isothermal settings on the display unit.

7.1.9 Atomizer

A general purpose atomizer was used to generate a water vapor plume consisting of particles with mean droplet diameter of 2.0 μm. This atomizer has six jets with three on-off valves to control the jets and built-in dilution air flowmeter. These features are useful for ranging the output particle concentrations.

7.2 Experimental Results

The feasibility of the infrared detection scheme was evaluated on subscale simulated laboratory plumes to determine sensitivity and general suitability for the application. The experimental analysis was undertaken with the objective of testing simple models to differentiate the amount of radiation coming from a radiation source passing through an absorbing, emitting and scattering medium. The feasibility experiments were completed using the Thermovision® system to obtain images of both hot and cold plumes in front of a warm background plate.

Planning was conducted for quantitative experiments with water vapor plumes. These experimental results were used to validate the numerical radiation transport model. In the following section several different experimental arrangements are presented.

7.2.1 Cold Plume in Front of Warm Background Plate

These experiments were accomplished with the cold plume in front of a warm background plate at several different plate temperature settings. The cold plume was provided by the atomizer and a hot plate was used as a background radiation source.

The heavy duty hot plate provided a temperature range from ambient to 755

^{o}K. The unit consists of a heated plate and a four position temperature switch. The top plate (23 x 23 cm) is heated by a resistance heater embedded in a refractory material. The plate is made of cast iron to withstand heavy thermal loads. The temperature of the plate is controlled by the four position temperature switch. The switch is used to select varying resistive loads that will vary the watts input.

Figure 7.6 shows a distinct cold plume against the warm background plate as obtained by the IR camera and enhanced by the VICOM digital image processing system. The thermal images of the background radiation with and without the plume were stored on a VCR for later analyses. This image was enhanced using computerized image analyser by subtracting the thermal images of the background radiation with the plume from the thermal images of the background radiation without the plume in order to enhance the difference.

The presence of cold plume reduced the incoming infrared radiation by absorbing the incoming thermal energy. This reduction of thermal energy by the plume is identified by the green shaded area in Figure 7.6 and can be easily distinguished from the warm background radiation source.

Figure 7.7 shows the thermal image of warm background radiation source without the plume at temperature of 460 ^{o}K. The integrated intensity variation across the plate is also plotted in this figure. Figure 7.8 is the thermal image of warm background plate with the plume of cold water vapor in front of it. These images were stored on VCR for analyses. The integrated intensity across the image of the plate with the plume was accomplished using the computerized images by subtracting the image of the plate with the plume from the image of the plate without the plume, in order to enhance the differences.

The cold water vapor plume creates a shaded area in the vertical, z, direction.

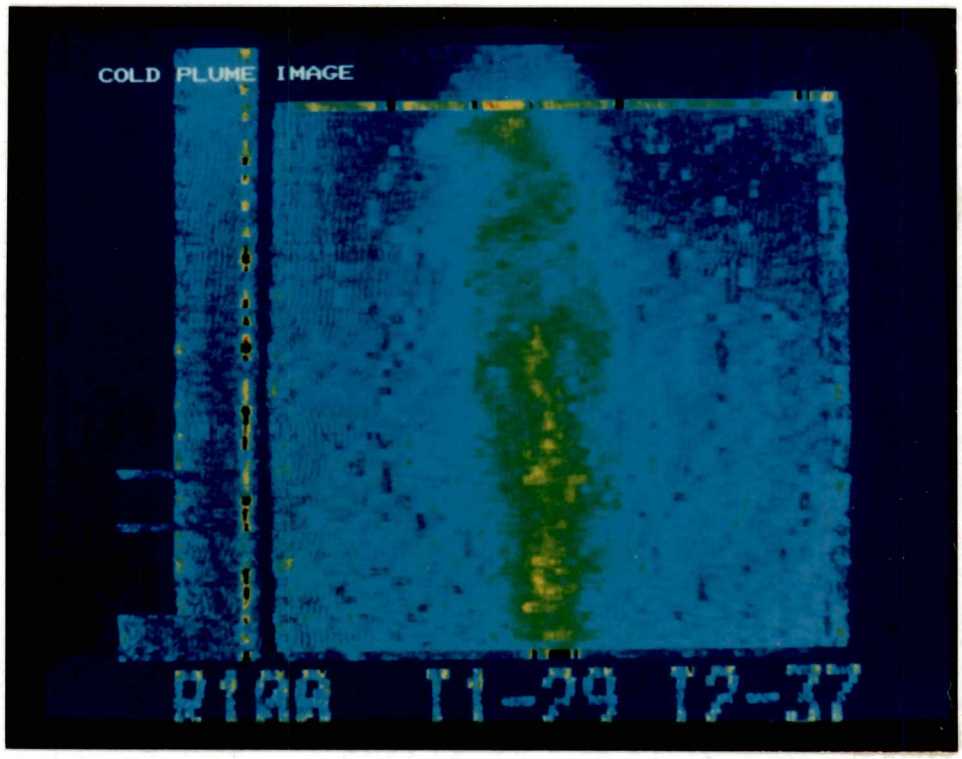


Figure 7.6 Thermal image of the cold plume in front of warm background radiation source

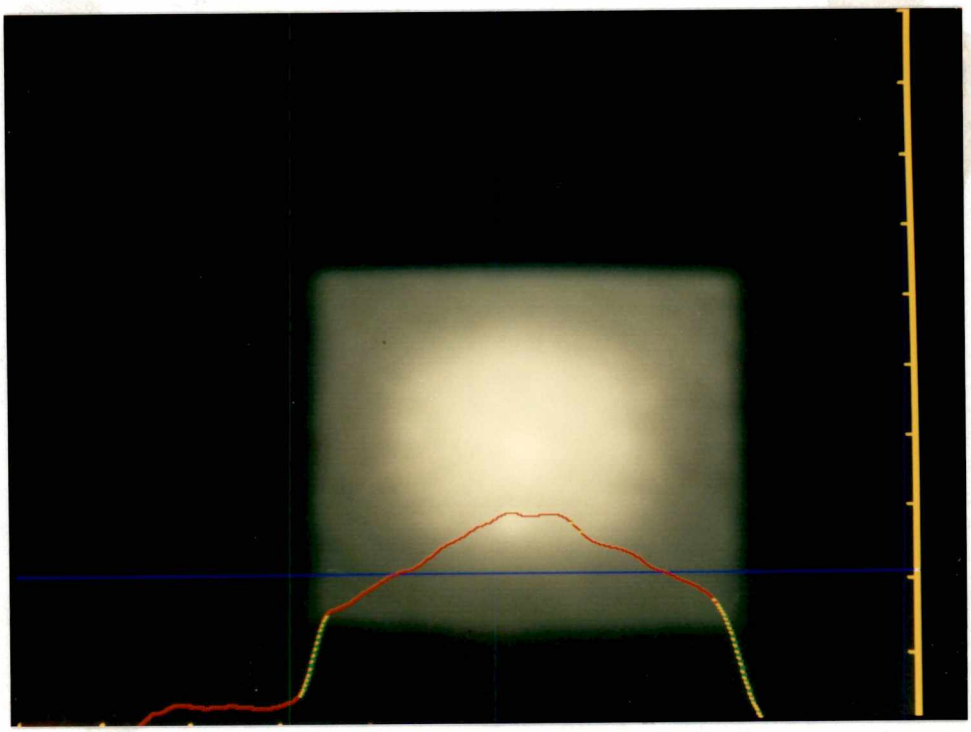


Figure 7.7 Thermal image of the warm background radiation source without the plume at $T_p = 460°K$

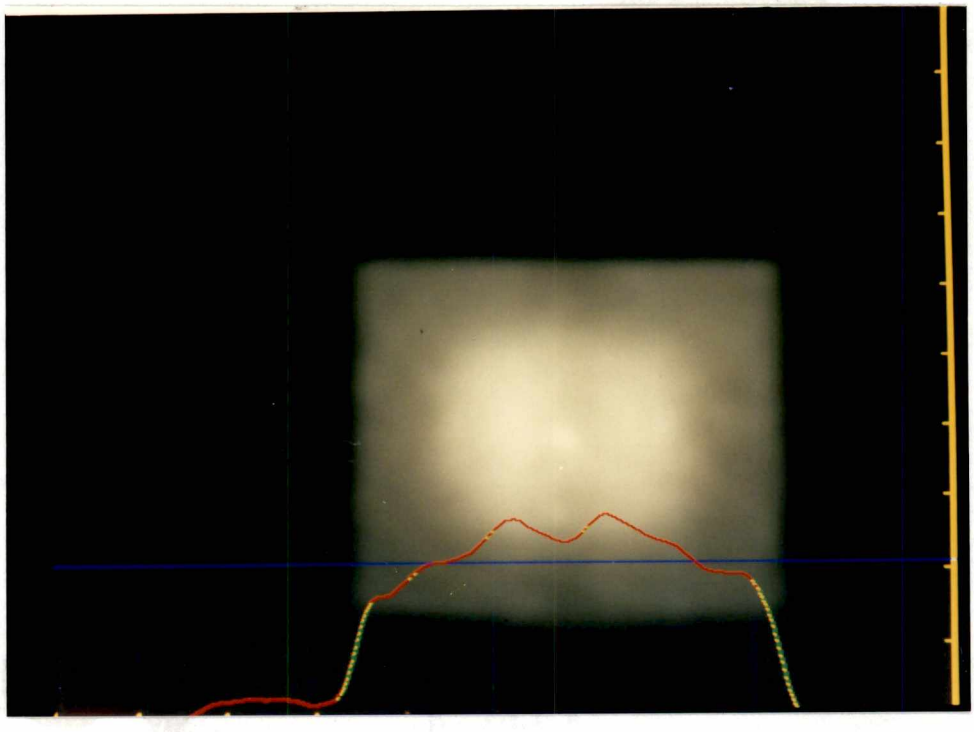


Figure 7.8 Thermal image of the warm background radiation source with the cold plume

The width of the shaded area represents the size of the plume. Figures 7.9 and 7.10 are similar to Figures 7.7 and 7.8 respectively. The only difference between these figures is the plate temperature for this case was 485 ^{o}K. More detailed explanation of these figures can be seen in section 7.3.

These important results have confirmed the sensitivity of the IR system to low intensity signals.

7.2.2 Hot Plume in Front of Warm Background Plate

The hot plume for this experiment was created by burning pure hydrogen gas in air. The thermal image of the hydrogen flame in front of the warm background plate is shown in Figure 7.11. The emission energy from the flame is strongly noticeable in this figure. The emission level from the hydrogen flame was much more intense than the emission from warm background radiation source. The IR camera easily distinguished the different between the warm background and the hydrogen flame.

This result confirms the sensitivity of the IR system to high intensity signals.

7.3 Comparison of Numerical and Experimental Results

Figure 7.12 is sketch of Figure 7.7 provided to explain the figures in a easier manner. The following discussion is valid for all the experimental figures in this section. The line (a) represents the level of the integrated intensity with scale of 0.0 to 1.0 (1.0 represents the maximum intensity). The line (b) shows a fixed z location for which the integrated intensity variations were plotted. The line (c) is the integrated intensity variation curve across the plate at z. The square (d) represent the warm background plate with a circular area in the center of plate which indicates the high temperature area; the intensity is higher in this region

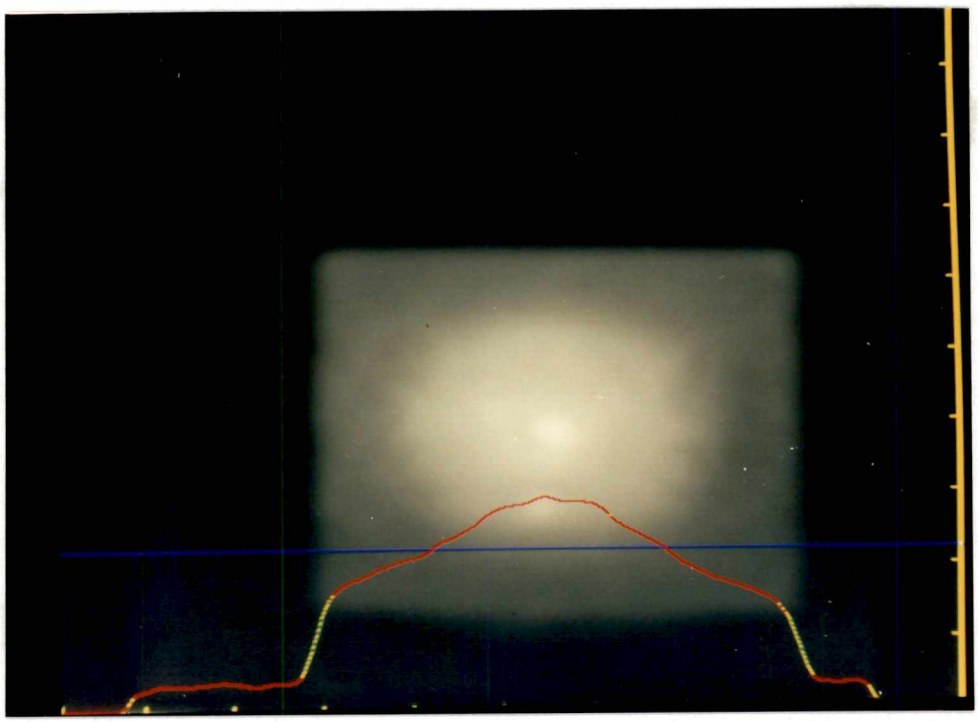


Figure 7.9 Thermal image of the warm background radiation source without the plume at $T_p = 485°K$

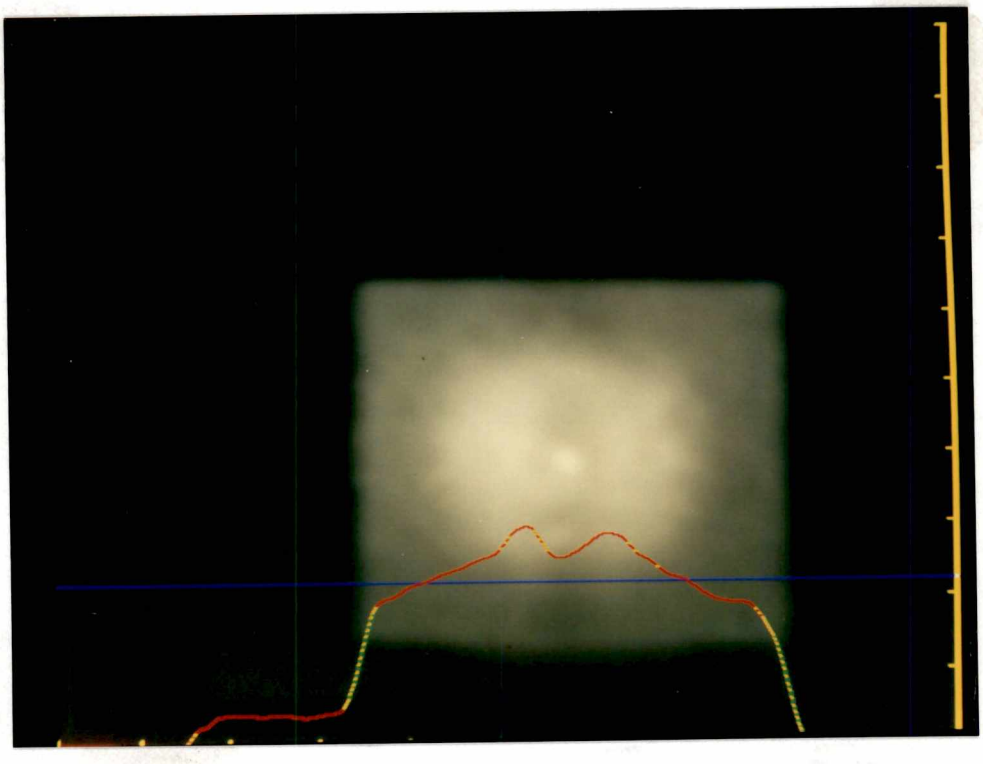


Figure 7.10 Thermal image of the warm background radiation source with the plume

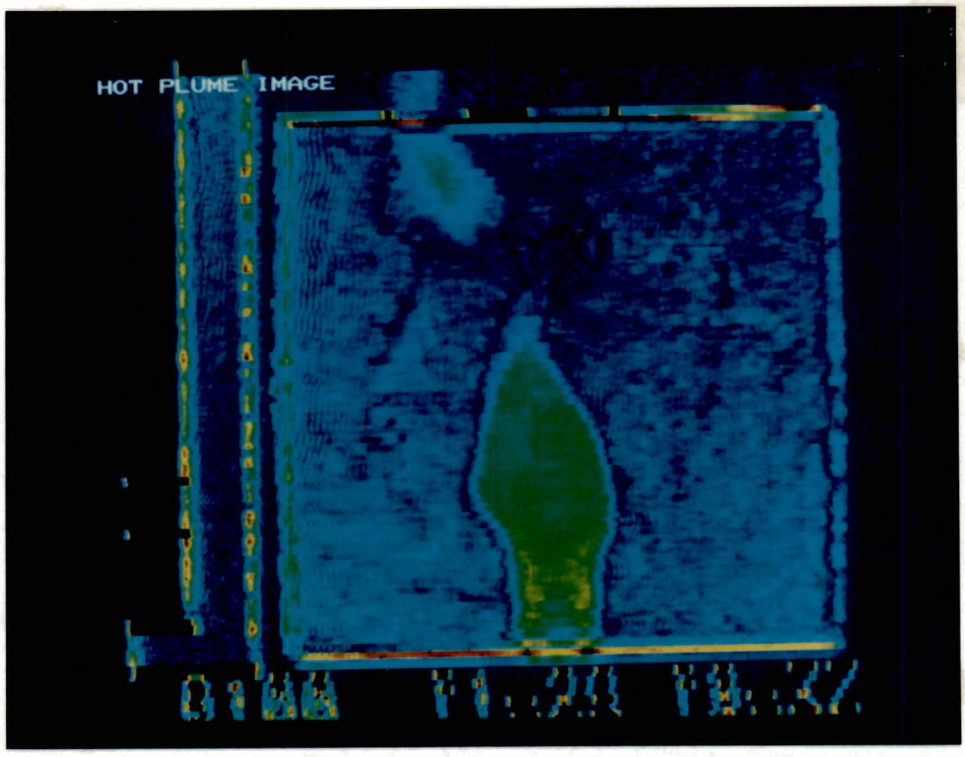


Figure 7.11 Thermal image of the hot plume in front of the warm background radiation source

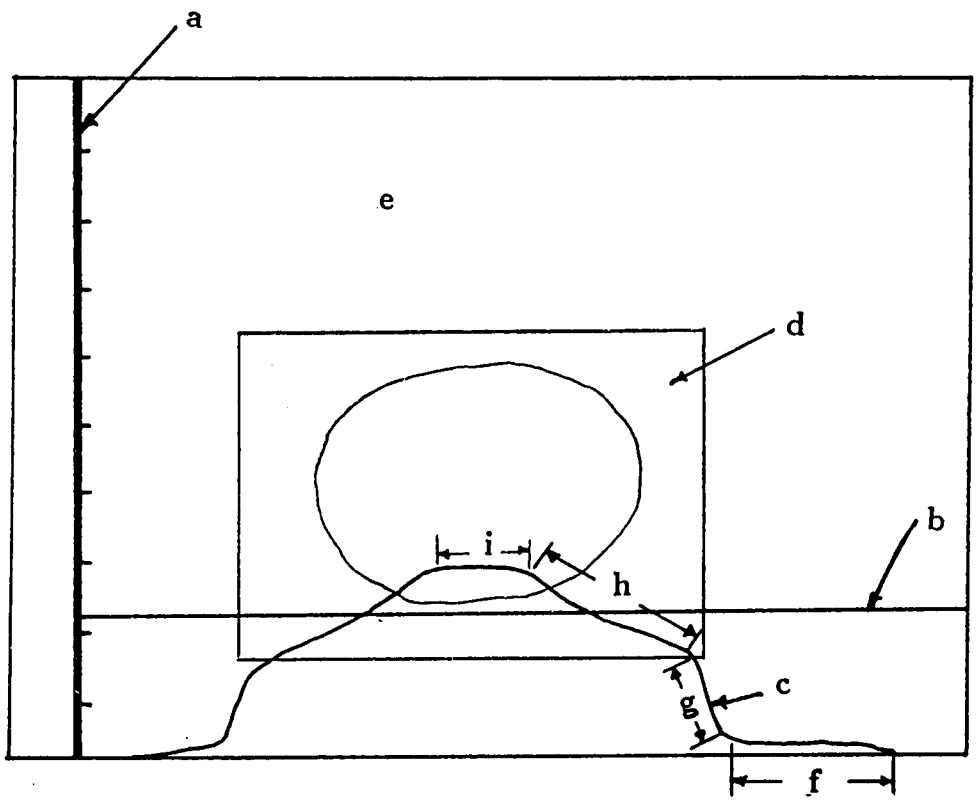


Figure 7.12 Sketch of a typical experimental result

than the rest of the plate. The rest of the figure (e) represents the environment.

The intensity variation (line c) can be divided into smaller segments in order to distinguish the representation of each line segments. The segment (f) represents the uniform intensity of the ambient; (g) represents the stepwise jump of intensity from the ambient to the warm plate due to sudden change of the temperature from environment at 300 ^oK to the plate temperature of 460 ^oK; (h) shows gradual increase in the integrated intensity level due to the nonuniformity of the plate temperature; finally (i) indicates that at the center of the plate the intensity is uniform.

The numerical results were obtained with the assumption of the plate being a uniform source of radiation from side to side. Figures 7.13 and 7.14 are the comparison of the numerical and experimental results obtained at plate temperature of 485 ^oK for plume diameter of 5.0 cm.

The integrated intensities as a function of the the actual distance across the plate geometry are plotted in these figures. Figure 7.13 is for the case of no scattering and Figure 7.14 is for the case which scattering is present with albedo of 0.4. The plate integrated intensity is decreased in the center due to the presence of the plume. This decay of the integrated intensity is due to the absorption of the incoming intensity by the plume. The maximum absorption effect appears at the center of the plume which is directly related to the plume size. The percentage of the integrated intensity reduction ($2 \leq \lambda(\mu) \leq 5$), from numerical results, is about 12% for Figure 7.13 and 14% in Figure 7.14.

The plate in the laboratory experiment was not a uniform source of radiation. Although the radiation source is not uniform, the results can still be used to prove the sensitivity of the IR detector for general purpose of this investigation. The plate (see Figures 7.7-7.10) has two distinct uniform temperatures, a circular

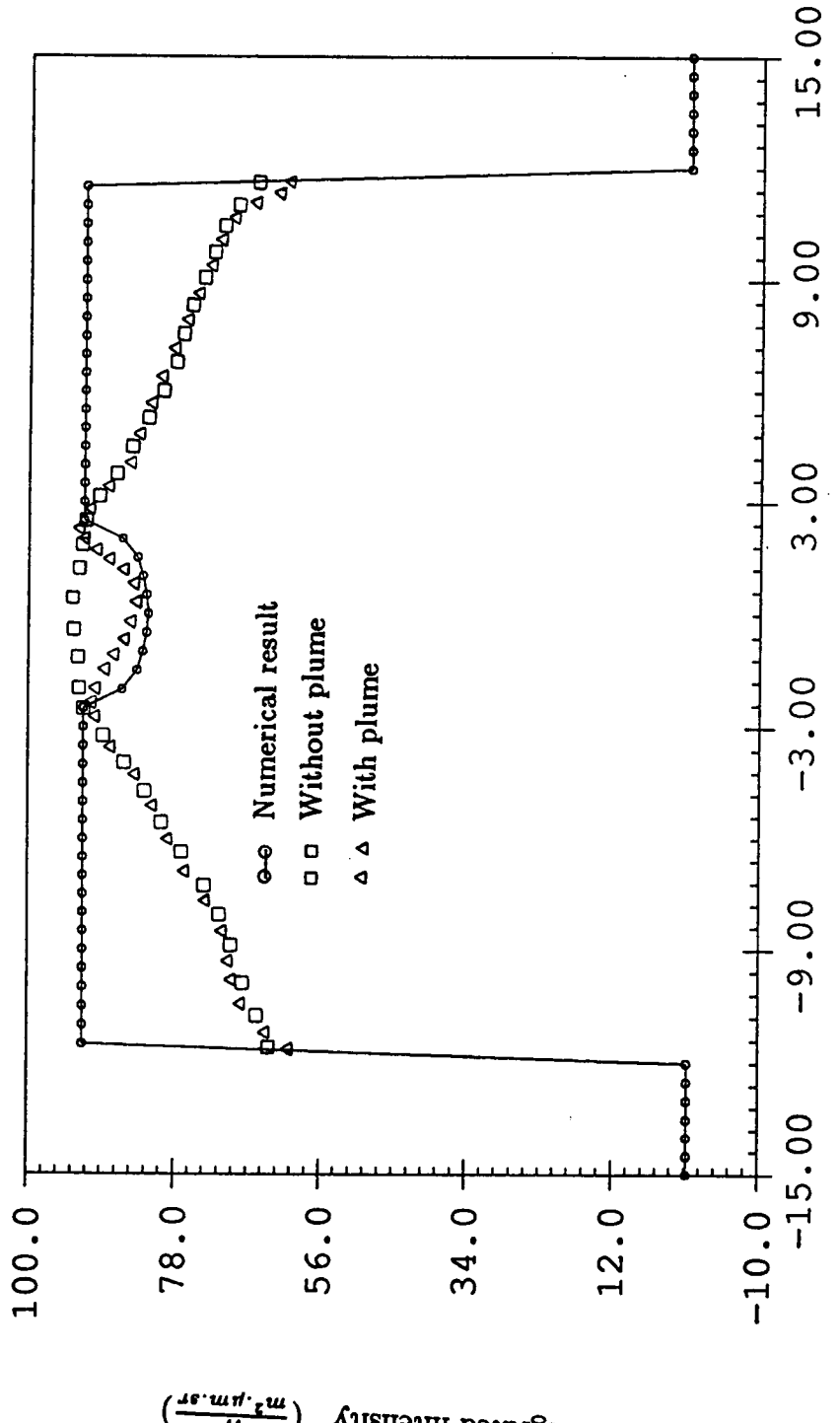


Figure 7.13 Comparison of the experimental and numerical integrated intensity across the plate ($T_p = 485°K$, $T_{max} = 300°K$, $T_{min} = 300°K$, $DP = 5(cm) and d\Omega = 0.0$)

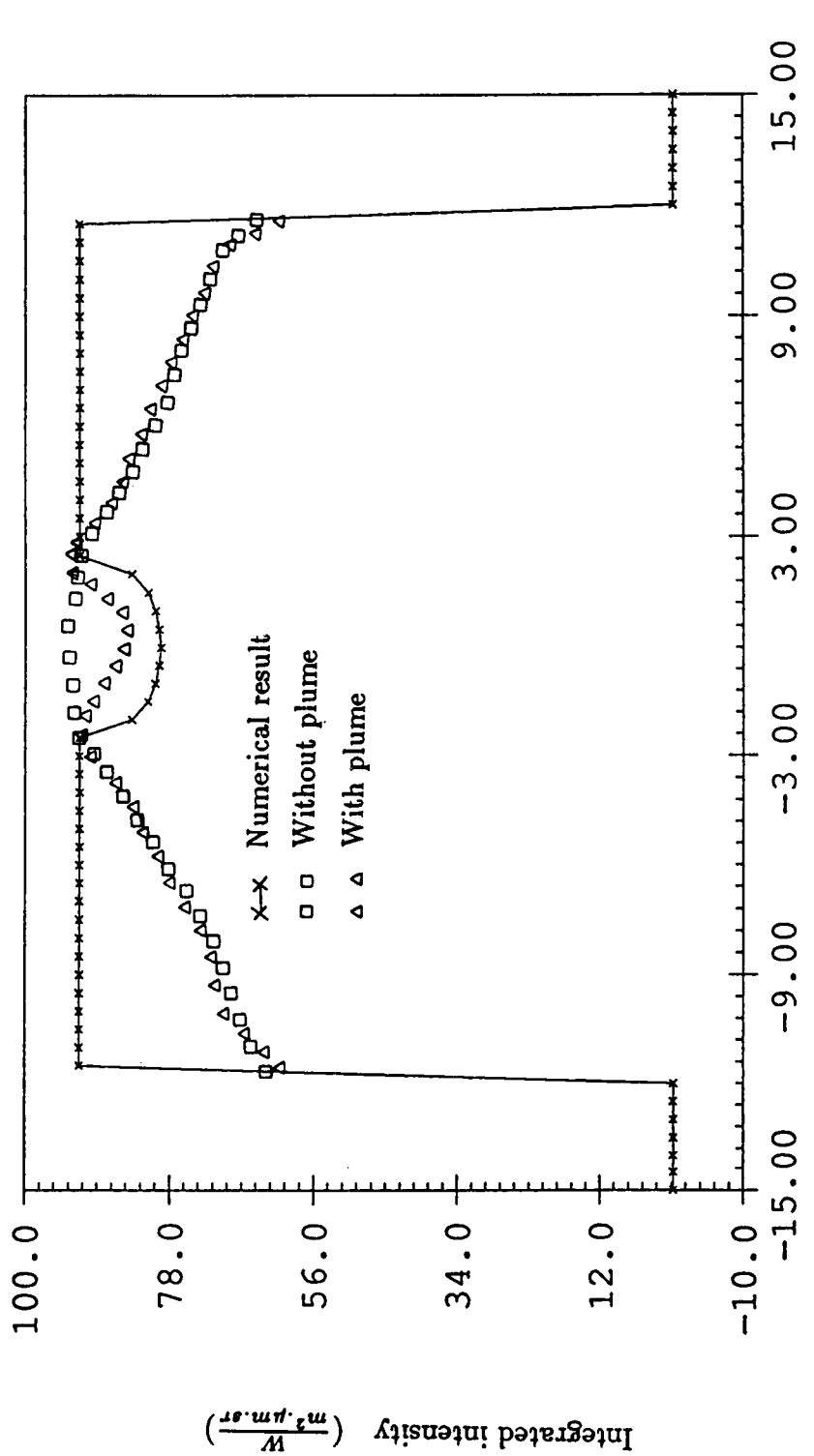


Figure 7.14 Comparison of the experimental and numerical integrated intensity across the plate ($T_p = 485°K$, $T_{max} = 300°K$, $T_{min} = 300°K$, $DP = 5(cm) and d\Omega = 0.4$)

area in the center of the plate with a fairly uniform temperature and another uniform temperature for the rest of the plate.

The experimental results indicated that the integrated intensity variation has a profile similar to the numerical results where the integrated reduction appears at the center of the plate where the plume is present. The percentage of the integrated intensity reduction ($2 \leq \lambda(\mu) \leq 5$), is about 11 % (from experimental result) compared to the 12 % and 14% of the numerical results. The small differences in the percentage of the intensity reduction can be explained in the following manner. First, the plume diameter in experimental cases are not as uniform as the numerical model. Second, the concentration of the water vapor for experiment was a mixture of air and water vapor, but for numerical calculations were based on the assumption of pure water vapor. Third, the experimental background plate was not isothermal but the numerical calculations were based on uniform plate temperature. Finally, the numerical calculations were accomplished for the cases of little scattering and with scattering. The scattering effect in the experimental cases could not be measured directly, but based on these comparisons it shows that there is no scattering present in the laboratory simulations.

The overall comparison of the experimental and numerical show that the experimental results generally validated the numerical radiation transport model.

7.4 Impingement Cooling

The complicated high pressure cycle of a rocket engine provides many opportunities for propellant path leaks while the engine is running. In such situations where a cryogenic fuel leak develops, the leak may impinge on local surfaces cooling parts of the engine which then result in sudden surface temperature changes in the areas around the leak. Therfore, a leak detection method can be proposed that is based

on monitoring surface thermal radiation and its time-variations.

In order to verify the effects of impingement cooling on surface radiation for leak detection, a simple experiment was performed. Figures 7.15 and 7.16 show the results of these experiments. These experiments were done by impinging cryogenic nitrogen on the hot plate. As it is shown in Figure 7.15, the plate temperature was 485 ^{o}K before the cryogenic impinged on the plate. Figure 7.16 shows the integrated intensity variation across the plate after cryogenic impingement on the surface of the hot plate. This figure shows two important results caused by the impingement cooling. First, the temperature was reduced from 485 to 445 ^{o}K and second the integrated intensity dropped significantly in the area of impingement cooling. The impingement cooling effect can easily be noticed by the darker shaded area on the right hand side of the plate in Figure 7.16.

The result from this experiment confirms that a suitably selected infrared detector is capable of detecting the cryogenic leaks that cause impingement cooling which effects a sudden change of the surface temperature of areas around the leak.

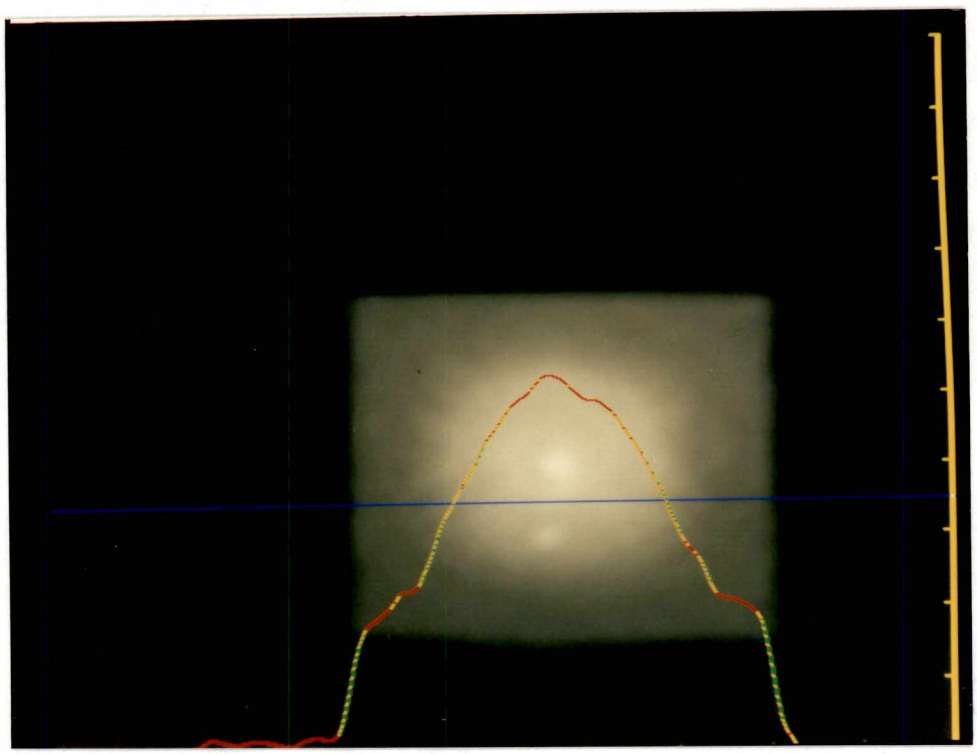


Figure 7.15 Thermal image of the warm background radiation source at $T_P = 485^o K$

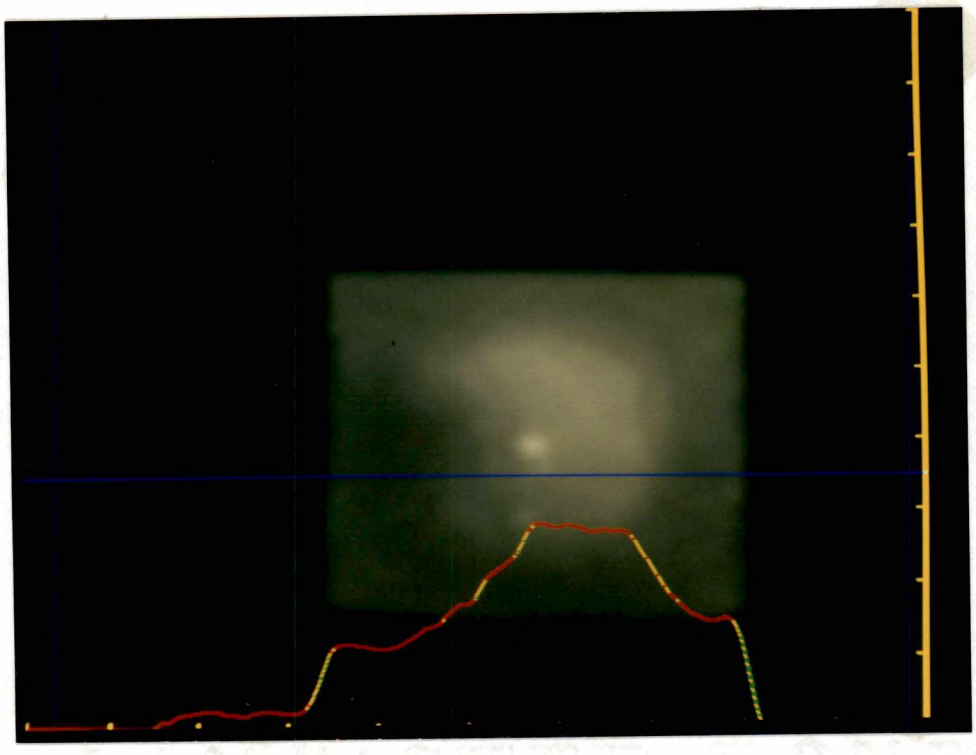


Figure 7.16 Thermal image of the impingement cooled plate at $T_P = 445^o K$

CHAPTER VIII

CONCLUSIONS AND RECOMMENDATIONS

The feasibility of using infrared optical sensors for liquid rocket engine leak detection systems was investigated by developing a radiative transfer model which contains the effect of emission, absorption, and scattering of an intervening medium on transmitted radiation in spectral bands. Various cases of spectral and integrated radiation were evaluated using this model to simulate many practical scenarios in propellant path leak conditions.

The theoretical results indicate that there are two distinct regions of the spectra that can be utilized to monitor two major types of gas leaks containing water vapor and/or particles of water. The region from 2.5 to 2.9 μ can be used to monitor cool leaks which are along the line-of-sight of the optical system and which block radiation emitted by hot surfaces of the rocket motor in the background. In addition, this wavelength range can be used to monitor hot leaks containing water vapor which are strong emitters of infrared radiation. These results suggest the choice of a band filter of 2.5-2.9μ for the IR camera used in leak detection. The results of the study indicate that in this wavelength range, most of the incoming infrared energy has been absorbed or emitted by the gas plume. The significant change of the background radiation intensity in this spectral region is a very sensitive warning signal for leaks of this type.

For situations where a cryogenic fuel leak impinges on local surfaces, the leak cools parts of the engine, which then results in sudden surface temperature drops in the areas around the leak. Therefore, a second leak detection method proposed in research study is based on monitoring surface thermal radiation and its time-variations. It was found by theoretical modeling of the phenomenon that

the spectral region $2 \leq \lambda \leq 2.3\mu$ and $3.4 \leq \lambda \leq 4.4\mu$ can be used to detect the sudden surface temperature change of the part experiencing the impinging leak. The important result of the theory and experiment conducted in this study was that at these wavelength ranges, cold plumes will not absorb the infrared signal from the chilled parts. This means that the total incoming infrared signal intensity will pass unchanged through the leak plume. Hence, background radiation from hot surfaces can be readily monitored in wavelength bands that are unaffected by absorption, emission, and scattering by the gaseous water vapor and vapor-particulate plumes. The theoretical results also indicated that the value of the minimum of integrated intensity over the entire relevant band width ($2 \leq \lambda \leq 5\mu$) decreases with increased plume diameter. This says that leak size is directly proportional to the extent of the reduction in the integrated intensity signal, and this can be used as a calibration technique for the leak size.

The experimental results obtained in this investigation confirm that a suitably selected infrared detector and band width filters are capable of being set up to detect hot and cold leaks as well as the cryogenic leaks that cause impingement cooling of nearby hot parts of the liquid rocket engine and structures.

The results of this research provide a basis for developing and employing intelligent leak detection systems in real-life complex environments. An important step in developing such a system is the integration of IR sensor technology, digital image processing, and expert systems into a real time leak-detection and health-monitoring analysis system. It is recommended, however, that additional laboratory simulations be conducted to further verify, extend and develop both the theoretical method for infrared signal transmission with absorption, emission, and scattering effects and also, the hardware (IR detector, vidicon, etc.) and software for the practical leak-detection system.

BIBLIOGRAPHY

BIBLIOGRAPHY

1. Panner, S.S., *Quantitative Molecular Spectroscopy and Gas Emissivities*, Addison-Wesley Publishing, Mass., 1959.

2. Ludwing, C.B., et al, *Handbook of Infrared Radiation from Combustion Gases.* NASA SP-3080, 1973.

3. Viskanta, R., "Heat Transfer by Conduction and Radiation in Absorbing and Scattering Material," Journal of Heat Transfer, February, 1965, pp. 143-150.

4. Love, T.J. and R.J. Grosh, "Radiative Heat Transfer in Absorbing, Emitting, and Scattering Media," Journal of Heat Transfer, May 1965, pp. 161-166.

5. Chan, J.H. and S.W. Churchill, "Anisotropic, Multiply Scattered Radiation from an Arbitrary, Cylindrical Source in an Infinite Slab," Journal of Heat Transfer, May 1965, pp. 167-172.

6. Heaslet, M.A. and R.F. Warming, "Radiation Transfer and Wall Temperature Slip in an Absorbing Planar Medium," Int. J. Heat Mass Transfer, Vol. 8, 1965, pp. 979-994.

7. Usiskin, C.M. and E.M. Sparrow, "Thermal Radiation Between Parallel Plates Separated by an Absorbing - Emitting Nonisothermal Gas," Int. J. Heat Transfer, Vol. 1, 1960, pp. 28-36.

8. Abu-Romia, M.M. and C.L. Tine, "Appropriate Mean Absorption Coefficient for Infrared Radiation of Gases," Journal of Heat Transfer, 1967, pp. 321-327.

9. Viskanta, R., "Radiation Transfer and Interaction of Convection With Radiation Heat Transfer," in *Advances in Heat Transfer*, Irvine, T.F. Jr., and Hartnett, J.P., eds., Vol. 3, Academic Press, New York, 1966.

10. Kourganoff, V., *Basic Methods in Transfer Problems*, Dover Publications, New York, N.Y., 1963.

11. Goody, R.M., *Atmospheric Radiation*, Oxford at the Clarendon Press, 1964.

12. Sampson, D.H., "Choice of an Appropriate Mean Absorption Coefficient for Use in the General Grey Gas Equations," *J. Quant. Spectrosc. Radiative Transfer*, Vol. 5, 1965, p. 211.

13. Grant, I.P., "On the Representation of Frequency Dependence in Non-Grey Radiative Transfer," *J. Quant. Spectrosc. Radiative Transfer*, Vol. 5, 1965, p. 227.

14. deSoto, S., and D.K. Edwards, "Radiative Emission and Absorption in Nonisothermal Nongrey Gases in Tubes," in the *Proceedings of Heat Transfer and Fluid Mechanics Institute*, Stanford University Press, Stanford, Calif., 1965.

15. Howell, J.R., and M. Perlmutter, "Monte Carlo Solution of Radiant Heat Transfer in a Nongrey Nonisothermal Gas With Temperature Dependent Properties," *AIChE Journal*, Vol. 10, 1964, p. 562.

16. deSoto, S., "Coupled Radiation, Conduction, and Convection in Entrance Region Flow," AIAA Paper No. 66-105, AIAA 3rd Aerospace Sciences Meeting, New York, N.Y., Jan. 1966.

17. Malkmus, W., and A. Thomson, "Infrared Emissivity of Diatomic Gases for the Anharmonic Vibrating-Rotator Model," *J. Quant. Spectrosc. Radiative Transfer*, Vol. 2, 1962, p. 17.

18. Breeze, J.E., C.C. Ferriso, C.B. Ludwing, and W. Malkmus, "Temperature Dependence of the Total Integrated Intensity of Vibration-Rotational Band Systems," *Journal of Chemical Physics*, Vol., 42, 1965, p. 402.

19. Jamieson, J.A., R.M. McFee, G.N. Plass, R.H. Grube, and R.G. Richards, *Infrared Physics and Engineering*, McGraw-Hill, New York, 1963.

20. Jakob, M., *Heat Transfer*, Vol. II. John Wiley, New York (1957).

21. Hottel, H.C. and E.C. Cohen, A.I. Ch. E. Journal 4, 3(1958).

22. Sparrow, E.M., C.M. Usiskin and H.A. Hubbard, *J. Heat Transfer*, Trans. ASME, Series C, 83, 199 (1961).

23. Tien, C.L., and M.M. Abu-Romia, Radiative Energy Transfer to the Outer Base Region of a Semi-Infinite Cylindrical Gas Body, AIAA Pre-print No. 64-60, (January 1964).

24. deSoto, S., The Radiation from an Axisymmetric, Real Gas System with a Non-Isothermal Temperature Distribution, presented at the Seventh National Heat Transfer Conference, AIChE-ASME, (August 1964).

25. Einstein, T.H., Radiant Heat Transfer to Absorbing Gases Enclosed in a Circular Pipe with Conduction, Gas Flow, and Internal Heat Generation, NASA TR R-156 (1963).

26. Heaslet, M.A. and R.F. Warming, "Theoretical Predictions of Radiative Transfer in Homogeneous Cylindrical Medium," *J. Quant. Spectrosc. Radiant Transfer*, 1966, Vol. 6, pp. 751-774.

27. Kesten, A.S., "Radiant Heat Flux Distribution in a Cylindrically-Symmetric Nonisothermal Gas with Temperature - Dependent Absorption Coefficient," *J. Quant Spectrosc. Radiative Transfer*, 1968, Vol. 8, pp. 419-434.

28. Vesngi, A. and J. Jsujita, "Diffuse Reflection of a Searchlight Beam by Slab, Cylindrical, and Spherical Media," 1969, Vol. 21, No. 4, Publications of the Astronomical Society of Japan.

29. Siegel R. and J. R. Howell, *Thermal Radiation Heat Transfer,* McGraw-Hill Book Company, 1981.

30. Love, T. J., *Radiative Heat Transfer,* Charles E. Merrill Publishing Company, 1968.

VITA

Sayed Ahmad Ali Shohadaee

I was born in Babol, the most ancient city of the northern state of Mazandaran in Iran, on January 5, 1957. I received my high school diploma from Momtaz High School in June 1976. After two years of mandatory military service in the Air Force of Iran, I came to the U.S.A. for higher education. I entered The University of Mississippi in Oxford, in fall 1979, and received the degree of Bachelor of Science in Mechanical Engineering in August 1981. I began graduate studies in fall 1981, accepted a teaching assistantship at the same university, and taught courses in heat transfer, engineering analyses and engineering laboratory. I received my Master of Science degree in Mechanical Engineering in May 1984.

I began my Ph.D. program at The University of Tennesse Space Institute (UTSI) in fall 1984 and accepted a Graduate Research Assistant at UTSI. During my course of study, I contributed most of my effort to two NASA projects, and received my Doctor of Philosophy degree in Mechanical/Aerospace Engineering in December 1990.

I am married and have three children, Maryam, Zahra, and Zaynab. I am a member of ASME, AIAA, and Sigma Pi Epsilon. I love most international sports, especially soccer, wrestling, and volleyball. I enjoy reading, playing soccer and volleyball, outdoor activities, and gardening.